Mon. Not. R. Astron. Soc. **324**, 389–419 (2001)

The peculiar motions of early-type galaxies in two distant regions – VI. The maximum-likelihood Gaussian algorithm

R. P. Saglia,[1★] Matthew Colless,[2] David Burstein,[3] Roger L. Davies,[4] Robert K. McMahan, Jr[5] and Gary Wegner[6]

[1]*Institut für Astronomie und Astrophysik, Scheinerstraße 1, D-81679 Munich, Germany*
[2]*Research School of Astronomy and Astrophysics, The Australian National University, Weston Creek, ACT 2611, Australia*
[3]*Department of Physics and Astronomy, Arizona State University, Tempe, AZ 85287-1504, USA*
[4]*Department of Physics, University of Durham, South Road, Durham DH1 3LE*
[5]*Department of Physics and Astronomy, University of North Carolina, CB#3255 Phillips Hall, Chapel Hill, NC 27599-3255, USA*
[6]*Department of Physics and Astronomy, Dartmouth College, Wilder Lab., Hanover, NH 03755, USA*

Accepted 2000 December 29. Received 2000 December 29; in original form 2000 September 7

ABSTRACT

The EFAR project is designed to measure the properties and peculiar motions of early-type galaxies in two distant regions. Here we describe the maximum-likelihood algorithm we developed to investigate the correlations between the parameters of the EFAR data base. One-, two- and three-dimensional Gaussian models are constructed to determine the mean value and intrinsic spread of the parameters, and the slopes and intrinsic parallel and orthogonal spread of the Mg_2–Mgb', Mg_2–σ, Mgb'–σ relations, and the Fundamental Plane. In the latter case, the cluster peculiar velocities are also determined. We show that this method is superior to 'canonical' approaches of least-squares type, which give biased slopes and biased peculiar velocities. We test the algorithm with Monte Carlo simulations of mock EFAR catalogues, and derive the systematic and random errors on the estimated parameters. We find that random errors are always dominant. We estimate the influence of systematic errors resulting from the way clusters were selected, and the hard limits and uncertainties in the selection function parameters for the galaxies. We explore the influence of uniform distributions in the Fundamental Plane parameters and the errors. We conclude that the mean peculiar motions of the EFAR clusters can be determined reliably. In particular, the placement of the two EFAR sample regions relative to the Lauer & Postman dipole allows us to constrain strongly the amplitude of the bulk motion in this direction. We justify a posteriori the use of a Gaussian modelling for the galaxy distribution in the Fundamental Plane space, by showing that the mean likelihood of the EFAR sample is obtained in 10 to 30 per cent of our simulations. We derive the analytical solution for the maximum-likelihood Gaussian problem in N dimensions in the presence of small errors.

Key words: galaxies: clusters: general – galaxies: distances and redshifts – galaxies: elliptical and lenticular, cD – galaxies: fundamental parameters – large-scale structure of Universe.

1 INTRODUCTION

The EFAR collaboration (Wegner et al. 1996, hereafter Paper I) has collected photometric (Saglia et al. 1997a,b, hereafter Papers III and IV) and spectroscopic (Wegner et al. 1999, hereafter Paper II) data for galaxies in clusters, with the primary goal of using the tight correlations between the global properties of early-types (the Fundamental Plane, hereafter FP, and the D_n–σ relation; see Djorgovski & Davis 1987 and Dressler et al. 1987) to measure the peculiar motions and the mass distribution on large scales. Colless et al. (2001, hereafter Paper VII) discuss the results of these investigations, and the interpretation of the peculiar motions in the context of cosmological models. This paper presents the methodology adopted to derive these results, and the Monte Carlo simulations performed to test them and to estimate the uncertainties and residual systematic biases. Colless et al. (1999, hereafter Paper V) discuss the implications of the EFAR Mg–σ relation.

★E-mail: saglia@usm.uni-muenchen.de

An abundant literature is dedicated to the problem of how best to determine regression lines from incomplete data sets subject to errors and explicit selection criteria. Regression algorithms involving two variables are discussed by Isobe et al. (1990) and Feigelson & Babu (1992), who provide least-squares fits and their uncertainties. Akritas & Bershady (1996) address the problem of linear regressions with errors and intrinsic scatter, by considering the variance of the variables involved. La Barbera, Busarello & Capaccioli (2000) extend this work to the analysis of the FP equation. The canonical methods used to find the coefficients of the FP (or of correlations between two variables) are of the least-squares type: one minimizes the orthogonal (absolute or squared) residuals from the plane (Jørgensen, Franx & Kjærgaard 1996; Jørgensen 1997; Pahre, Djorgovski & Carvalho 1997; Scodeggio, Giovanelli & Haynes 1997) or the (squared) residuals from one of the variables (Hudson et al. 1997). Principal component analysis has also been used (Carvalho & Djorgovski 1992). Ample discussion of problems related to selection is given by Willick (1994) and Teerikorpi (1997), in the context of the determination of peculiar velocity fields. However, none of these approaches is able to deal effectively with the multiple problems that the EFAR and similar data sets pose: (i) the factor of 2 in redshift spanned, (ii) the strong selection effects, (iii) the non-negligible and widely varying measurement errors, (iv) the presence of defined selection criteria, and (v) the intrinsic scatter of the relation. In this paper we demonstrate that 'classical' methods fail when confronted with the EFAR data set, and we quantify the biases they produce. We construct an algorithm based on maximum-likelihood (ML) Gaussian modelling, and test it with Monte Carlo simulations. We demonstrate that it solves the problems posed by the data set, producing nearly unbiased estimates of the parameters involved.

The paper is organized as follows. Section 2 discusses critically the results of linear regression analysis and presents the ML algorithm for the one-, two- and three-dimensional cases. Section 3 describes the method to generate mock catalogues of the EFAR data base, the tests of the 'canonical' least-squares methods and of the ML Gaussian algorithm, and the estimates of the errors on the derived parameters. Simulations backing the results presented in Papers II, V and VII are discussed for the Mg_2–Mgb', Mgb'–σ and Mg_2–σ relations, the FP and the cluster peculiar velocities. Conclusions are drawn in Section 4. The appendices give the analytical solution of the N-dimensional Gaussian ML problem in the presence of small errors and some results used in the paper.

2 THE MAXIMUM-LIKELIHOOD GAUSSIAN ALGORITHM

After reviewing the results of the standard least-squares analysis in Section 2.1, we describe the properties of the EFAR data base in Section 2.2 to argue that a ML approach is needed to study the sample. We set the equations of the problem for the general case in Section 2.3, and address the simplified cases when one (Section 2.4), two (Section 2.5) or three (Section 2.6) variables are considered.

2.1 Linear models

Before discussing the specific problems related to the EFAR data base and the solutions we have developed to address them, it is worth considering the more general question of how to model the correlations existing between the structural parameters of galaxies. As usual in astrophysics, logarithmic quantities are considered in order to avoid scaling problems. In the simplest approach, one focuses on pairs of data points $\{x_i, y_i\}$, looking for a linear relation $y = ax + b$ between them. table 1 of Isobe et al. (1990) (see also equations 6–9 below) summarizes the estimates of the slopes a and zero-points b, and their variances, derived using five methods ($Y - X$ and $X - Y$ regressions, bisector, reduced major axis and orthogonal regression), when measurement errors are negligible. Briefly, we recall that the $Y - X$ regression derives the slope a_{YX} and zero-point b_{YX} of the line $y = a_{YX}x + b_{YX}$ by minimizing the quantity

$$\chi^2_{YX} = \Sigma_i (y_i - a_{YX}x_i - b_{YX})^2, \tag{1}$$

and the $X - Y$ regression by minimizing the analogous χ^2_{XY}. The bisector solution gives the slope and zero-point of the line passing in between the $Y - X$ and $X - Y$ lines. The reduced major axis slope is the geometric mean of the $Y - X$ and $X - Y$ slopes. The orthogonal regression derives a_O and b_O by minimizing the orthogonal residuals from the line

$$\chi^2_{YX} = \Sigma_i \frac{(y_i - a_O x_i - b_O)^2}{1 + a_O^2}. \tag{2}$$

If the differences in slopes and zero-points between the methods are smaller than the expected variance, a well-defined answer is found. Unfortunately, this is rarely the case in astronomy. Isobe et al. therefore recommend that astronomers use the $Y - X$ regression when it is clear that Y is the variable to be 'predicted', and the bisector method when the functional relation between the variables has to be investigated. They discourage the use of the orthogonal regression, since its slope has greater dispersion. The problem is complicated when errors (on one or both variables) are present. In particular, Feigelson & Babu (1992) conclude that 'models incorporating both measurement errors and intrinsic scatter are complex and not yet fully developed'. Akritas & Bershady (1996) improve on this aspect, presenting an updated version of table 1 of Isobe et al., where corrections for measurement errors are taken into account. Isobe et al., Feigelson & Babu and Akritas & Bershady stress that 'there is no such thing as true slope', and that the regression method should be chosen according to the problem to be solved.

These considerations become more transparent when the underlying bivariate probability distributions $P(x,y)$ are examined. Assuming normality, $P(x, y)$ can always be written as

$$P(x,y) = \frac{1}{2\pi\sigma_x\sigma_y\sqrt{1-\rho^2}} \exp\left\{ -\frac{1}{2(1-\rho^2)} \times \left[\frac{(x-\bar{x})^2}{\sigma_x^2} - \frac{2\rho(x-\bar{x})(y-\bar{y})}{\sigma_x\sigma_y} + \frac{(y-\bar{y})^2}{\sigma_y^2} \right] \right\}, \tag{3}$$

where $\bar{x}$ and $\bar{y}$ are the mean values of x and y, σ_x and σ_y the standard deviations (rms scatter), and ρ the correlation coefficient defined as $\sigma_{xy} = \rho\sigma_x\sigma_y$. Calling $\hat{x} = x - \bar{x}$ and $\hat{y} = y - \bar{y}$, equation (3) can be cast as

$$P(x,y) = \frac{|\mathbf{\Lambda}|^{1/2}}{2\pi} \exp\left\{ -\frac{1}{2}[\Lambda_{xx}\hat{x}^2 + 2\Lambda_{xy}\hat{x}\hat{y} + \Lambda_{yy}\hat{y}^2] \right\}, \tag{4}$$

where $\mathbf{\Lambda} = \boldsymbol{V}^{-1}$, $|\mathbf{\Lambda}| = \Lambda_{xx}\Lambda_{yy} - \Lambda_{xy}^2 = [(1-\rho^2)\sigma_x^2\sigma_y^2]^{-1}$, and $\boldsymbol{V}$

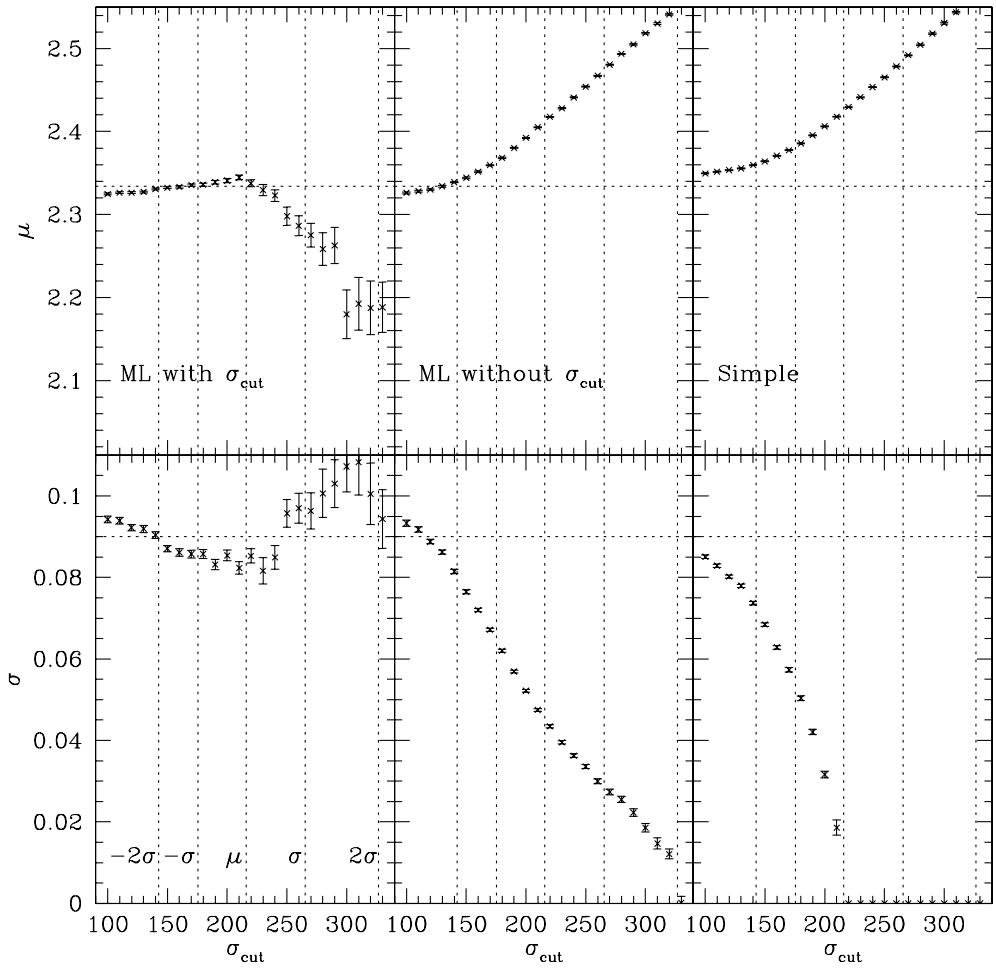

Figure 1. The results of the simulations of the σ distribution. The panels to the left show the mean (top panel) and rms (bottom panel), averaged over 99 simulations, as derived by the ML algorithm with normalization correction for $\sigma_{\rm cut}$. The error bars are $1/\sqrt{99}$ smaller than the random error expected for one simulation. The central panels show the mean (top) and rms (bottom) as derived by the ML algorithm without normalization correction for $\sigma_{\rm cut}$. The panels to the right show the simple mean (top) and rms (bottom, corrected for measurement errors). The horizontal dotted lines give the input values. The vertical dotted lines mark the positions of the input mean value, and $\pm\sigma$, $\pm2\sigma$ away from it.

is the covariance matrix:

$$\boldsymbol{V} = \begin{pmatrix} \sigma_x^2 & \rho\sigma_x\sigma_y \\ \rho\sigma_x\sigma_y & \sigma_y^2 \end{pmatrix},$$

$$\boldsymbol{\Lambda} = \frac{1}{1-\rho^2}\begin{pmatrix} 1/\sigma_x^2 & -\rho/(\sigma_x\sigma_y) \\ -\rho/(\sigma_x\sigma_y) & 1/\sigma_y^2 \end{pmatrix}. \tag{5}$$

Equations (3) and (4) are equivalent to the three following formulae:

$$P(x,y) = \frac{1}{\sqrt{2\pi}\sigma_x}\exp\left(-\frac{\hat{x}^2}{2\sigma_x^2}\right)\frac{1}{\sqrt{2\pi}\sigma_y\sqrt{1-\rho^2}} \times \exp\left[-\frac{1}{2}\frac{\left(\hat{y}-\dfrac{\rho\sigma_y}{\sigma_x}\hat{x}\right)^2}{(1-\rho^2)\sigma_y^2}\right], \tag{6}$$

$$P(x,y) = \frac{1}{\sqrt{2\pi}\sigma_y}\exp\left(-\frac{\hat{y}^2}{2\sigma_y^2}\right)\frac{1}{\sqrt{2\pi}\sigma_x\sqrt{1-\rho^2}} \times \exp\left[-\frac{1}{2}\frac{\left(\hat{x}-\dfrac{\rho\sigma_x}{\sigma_y}\hat{y}\right)^2}{(1-\rho^2)\sigma_x^2}\right], \tag{7}$$

$$P(x,y) = \frac{1}{\sqrt{2\pi}\sigma_1}\exp\left[-\frac{(\hat{y}-a_o\hat{x})^2}{2(1+a_o^2)\sigma_1^2}\right]\frac{1}{\sqrt{2\pi}\sigma_2} \times \exp\left[-\frac{(a_o\hat{y}+\hat{x})^2}{2(1+a_o^2)\sigma_2^2}\right], \tag{8}$$

where

$$a_o = \frac{1}{2\rho\sigma_x\sigma_y}\left[\sigma_y^2-\sigma_x^2+\sqrt{(\sigma_y^2-\sigma_x^2)^2+4\rho^2\sigma_x^2\sigma_y^2}\right], \tag{9}$$

$$\sigma_1^2 = \frac{1}{2}\left[\sigma_x^2+\sigma_y^2+\sqrt{(\sigma_y^2-\sigma_x^2)^2+4\rho^2\sigma_x^2\sigma_y^2}\right], \tag{10}$$

$$\sigma_2^2 = \frac{1}{2}\left[\sigma_x^2+\sigma_y^2-\sqrt{(\sigma_y^2-\sigma_x^2)^2+4\rho^2\sigma_x^2\sigma_y^2}\right]. \tag{11}$$

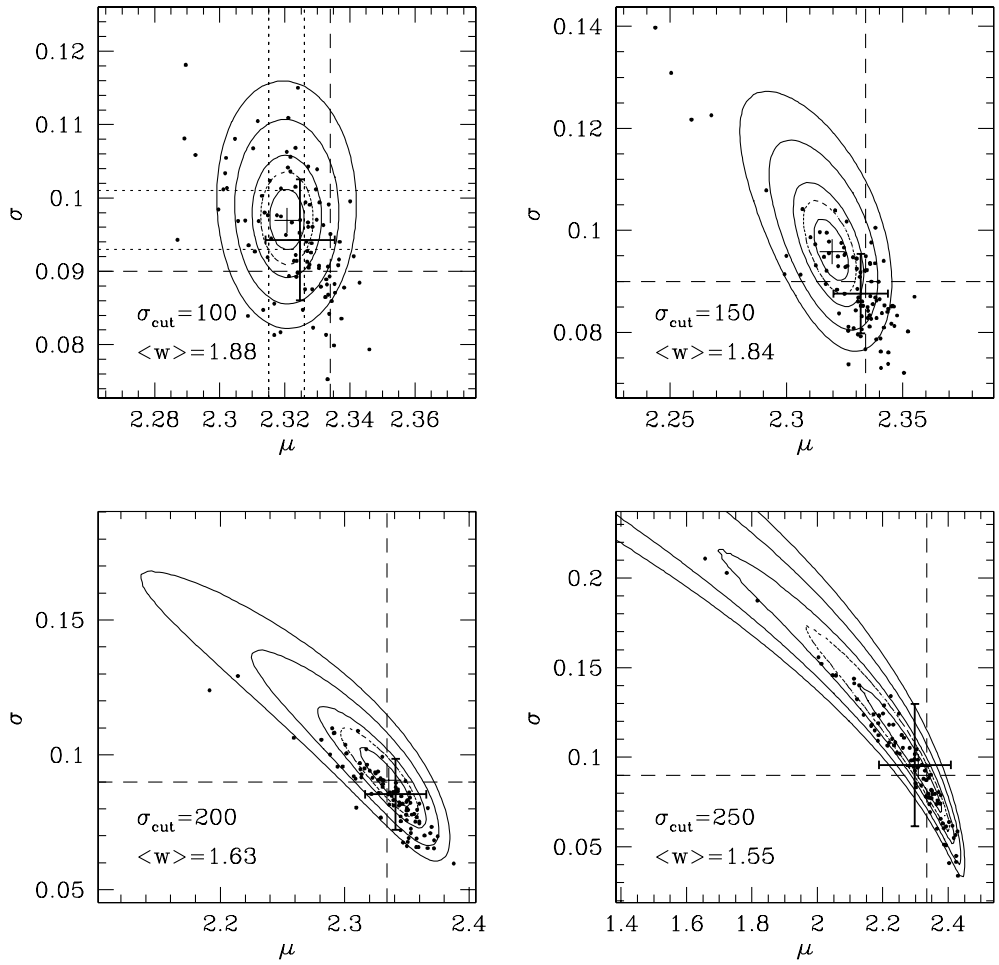

Figure 2. The contours of constant likelihood in the (μ, σ) plane for one of the simulations in Fig. 1 analysed by the ML algorithm with normalization correction $\sigma_{\rm cut}$ = 100, 150, 200 and 250 km s^{-1} respectively. The projections (shown as dotted lines for the $\sigma_{\rm cut}$ = 100 case) of the four full-line contours give the one-dimensional 1σ, 2σ, 3σ and 4σ confidence intervals. The dotted contours show the 1σconfidence regions in two dimensions. The small crosses mark the ML solution. The applied mean selection weights $\langle w\rangle$ scaling factors are given in each panel (see text). The dashed lines show the input values of the mean μ and rms σ. The dots show the positions of ML solutions of the simulations of Fig. 1. The thick error bars mark the position of μ and σ, averaged over the 99 simulations of Fig. 1, and show their rms.

Equation (6) shows that a Gaussian bivariate probability distribution can be generated extracting first the x variable around its mean with rms σ_x, and then the residual $\xi = \hat{y} - (\rho\sigma_y/\sigma_x\hat{x}$ around the $Y - X$ line with slope equal to the regression of Y on X and rms $\sqrt{1-\rho^2}\sigma_y$. Similarly, equation (7) shows that the same distribution can be generated first extracting the y variable and then the residual $\zeta = \hat{x} - (\rho\sigma_x/\sigma_y)\hat{y}$ around the $Y - X$ line with slope equal to the regression of X on Y. Finally, equation (8) generates the distribution extracting the residuals around the eigenvectors of the covariance matrix. The direction of the eigenvector with the largest eigenvalue is the slope of the orthogonal regression. The zero-points b of the relevant linear relations of slope a are obtained from the mean values as

$$b = \bar{y} - a\bar{x}. \tag{12}$$

Do we therefore conclude, as did Akritas & Bershady (1996), that 'there is no such thing as true slope'? In fact, the key of the problem is the covariance matrix, and therefore the natural slope is the direction of the principal axes (given by equation 9) with the largest eigenvalue (given by equation 10; equation 11 is the second eigenvalue of the covariance matrix). As a consequence, the orthogonal regression determines the 'true slope', not the bisector, which Isobe et al. (1990) prefer for its lower variance. However, what about distance determination problems, where equation (6) should be preferred according to Akritas & Bershady, if y is the distance-dependent quantity? Indeed, if one seeks for the distance shift δ of the data point $(\hat{y}_i + \delta, \hat{x}_i)$, the most probable value when equation (3) is given is

$$\delta = -\left(\hat{y}_i - \frac{\rho\sigma_y}{\sigma_x}\hat{x}_i\right), \tag{13}$$

which involves the $Y - X$ regression coefficient V_{xy}/V_{xx}.

Further complications arise when the data points $\{x_i, y_i\}$ are affected by errors comparable to the rms spreads σ_x and σ_y, or when only a subset of the possible data volume is available due to incompleteness. These affect the estimation of the covariance matrix V and the mean values of the variables. For example, we estimate in Appendix B that the orthogonal regression solution ignoring the errors underestimates the true slope if the error in the X direction is larger than the one in Y. These effects might be included in the regression approach by careful treatement (see references given in Feigelson & Babu 1992), but it is clear from

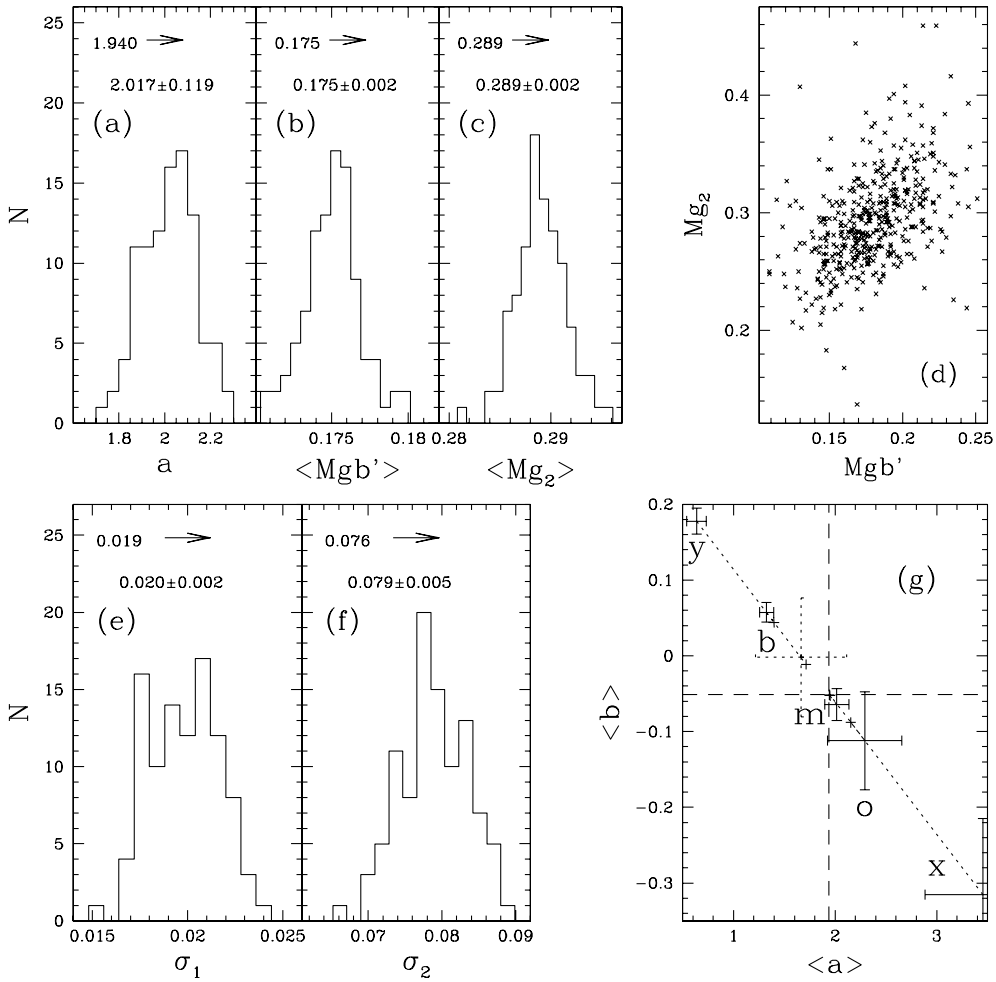

Figure 3. The results of the Mg_2–Mgb' simulations. The panels show the histograms of (a) the slopes, the mean values of (b) $\langle Mgb' \rangle$ and (c) $\langle Mg_2 \rangle$, the orthogonal and parallel spread (e) σ_1 and (f) σ_2 as derived from the ML algorithm. Input values, means and rms of the 99 simulations are also given. Panel (d) shows one of the 99 Mg_2–Mgb' realizations. Panel (g) shows the values of the slopes a and zero-points b, averaged over 99 simulations and derived using the Y–X (y), the X–Y (x), bisector (b) and orthogonal (o) regressions, plus the ML algorithm (m). The error bars show the random errors expected for one simulation. The dotted cross shows the values and the random errors of the slopes a and zero-points b, averaged over 99 simulations, derived using the $Y - X$ regression, taking into account errors as in Akritas & Berschady (1996). The horizontal and vertical dashed lines show the input values. The other dotted lines of plot (g) terminating to the small crosses show the values obtained when the errors are reduced by a factor of 5. The crosses for the ML and orthogonal regression cases overlap.

the discussion above that an ML approach is superior, allowing the natural and simultaneous solution of all these difficulties.

2.2 The EFAR data base

The EFAR data base comprises photometric and spectroscopic information for a set of cluster galaxies spanning a factor of 2 in redshift, with non-negligible measurement errors and selection effects.

The size of the errors can be quantified comparing the rms spread of the variables with the mean of the errors. In this sense photometric errors (≈0.02 mag; see Papers III and IV) are small in the EFAR data base. Unfortunately, this is not the case for the spectroscopic data (see Paper II). For the case of the velocity dispersions σ, we find that the mean value (25 km s^{-1}) of the measurement errors on σ is 36 per cent of the rms spread of the values (71 km s^{-1}). For the Mgb index, the mean value (0.39 Å) of the measurement errors is 48 per cent of the rms spread of the values (0.83 Å). In addition, we cannot measure central velocity dispersions smaller than 100 km s^{-1} for lack of spectral resolution.

Selection effects are also severe. The galaxy sample is more than 50 per cent complete only for galaxies with $D_W > 20$ kpc (see Paper I), with 46 per cent of the galaxies having selection probabilities larger than 50 per cent. The EFAR galaxy selection S is described in Paper I, and is a function of the $D_{i,\,W}$ diameter measured in arcsec for galaxy i:

$$S_{i,j}(\log D_{i,W}) = 0.5\left[1 + \mathrm{erf}\left(\frac{\log D_{i,W} - \log D^0_{W,j}}{\delta_{W,j}}\right)\right], \qquad (14)$$

where j is the cluster index, $\log D^0_{W,j}$ is the mid-point, and $\delta_{W,j}$ the width of the cut-off in the selection function. The diameter $D_{i,W}$ correlates with the $D_{i,n}$ diameter of the sample, as $\log D_{i,n} = 0.8 \times \log D_{i,W} + 0.26$ with 0.09 dex scatter in $D_{i,n}$ (see Paper III). Therefore we compute the selection probabilities $S_{i,j}$ from the $D_{i,Wn}$ diameters derived from the very accurate $D_{i,n}$ instead of using the values of $D_{i,W}$ given in Paper I. In the following we shall indicate with S_i the selection probability for the galaxy i, dropping the cluster index, and with $w_i = 1/S_i$ the selection weight.

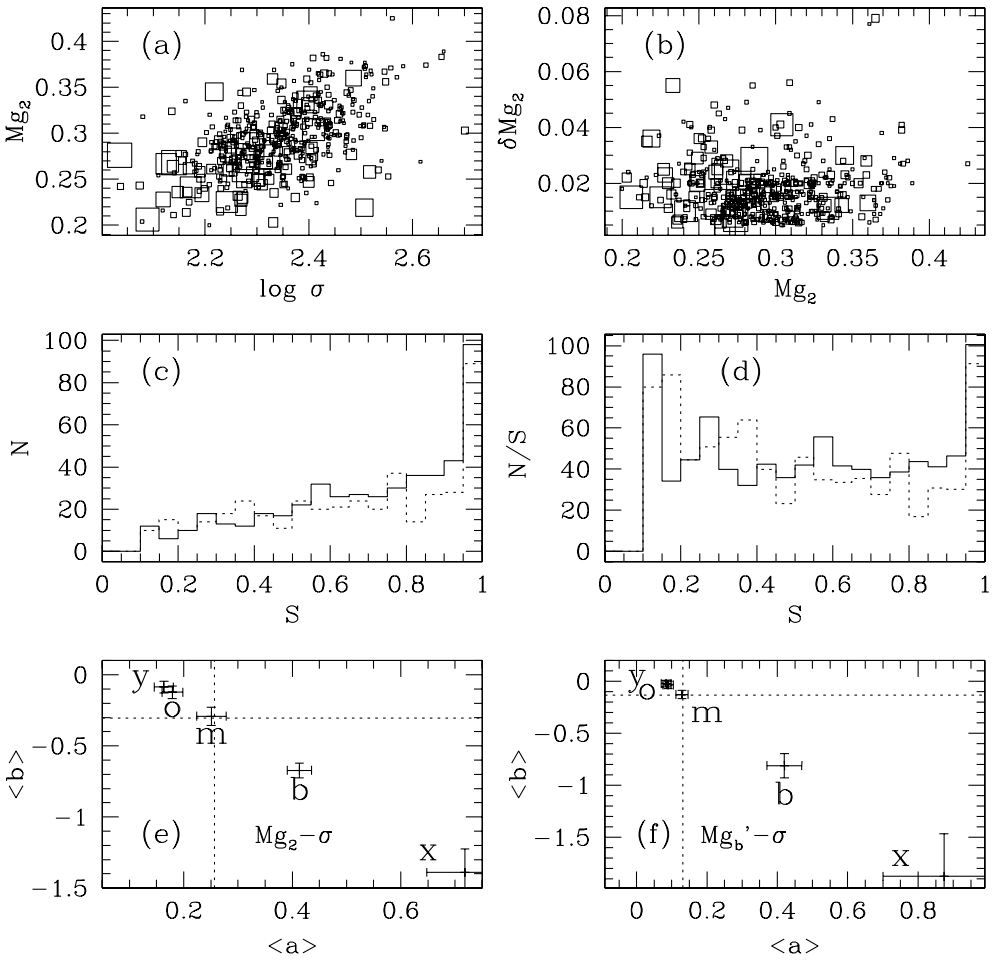

Figure 4. The results of the Mg_2–σ and Mgb'–σ simulations. Panel (a) shows one of the 99 Mg_2–σ realizations. The size of the points is proportional to their selection weight $1/S$. Panel (b) shows the distribution of the Mg_2 errors. Panel (c) plots the distribution of selection probabilities S for the simulation shown in (a) and (b) (full line) and for the EFAR data base (dotted line) analysed in Paper V. Panel (d) plots the effective number of data points N/S as a function of S for the simulation shown in (a) and (b) (full line) and for the EFAR data base (dotted line) analysed in Paper V. Panels (e) and (f) show the values of the slopes a and zero-points (b), averaged over 99 simulations and derived using the Y–X (y), the X–Y (x), bisector (b) and orthogonal (o) regressions, plus the ML algorithm (m), for the Mg_2–σ and Mgb'–σ relations respectively. The error bars show the random errors expected for one simulation. The horizontal and vertical dotted lines show the input values.

Due to the large spread in redshift, the EFAR clusters have been sampled down to different limiting D^0_W(kpc). However, 95 per cent of the early-type galaxies in the sample have $D_{Wn} > 12.6$ kpc, so that nearly unbiased estimates of the cluster peculiar velocities can be obtained just by dropping from the sample objects with $\log D_{Wn} \leq d_{\rm cut} = \log D_{W{\rm cut}}$.

To our knowledge, no algorithm based on linear regressions has been developed to model all these features at the same time. In the following we describe a parametric algorithm based on Gaussian modelling able with to deal with (i) a spread of selection weights, (ii) sizeable measurement errors with a large spread, and (iii) possible explicit selection limits.

2.3 The general case

In the general case, we have N (logarithmic) data $\boldsymbol{x}_i = (x_{i,1}, \cdots, x_{i,N})$ for each galaxy i. We indicate with $\boldsymbol{E}_i$ the related $N \times N$ error matrix. If the errors are uncorrelated, $\boldsymbol{E}_i$ is a diagonal matrix with $E_{i,j,k} = \delta_{j,k}\sigma^2_{i,j}$, where $\delta_{j,k} = 1$ if $j = k$ and 0 otherwise. Each galaxy has been selected according to the value of a selection diameter, which possibly could be expressed as a linear combination of a subsample of $x_{i,N}$, giving a selection weight $w_i = 1/S_i$. One variable $x_{i,1}$ may be distance-dependent. We want to estimate the vector of the mean values of the data $\bar{\boldsymbol{x}} = (\overline{x_1}, \cdots, \overline{x_N})$, the covariance matrix $\boldsymbol{V}$ and, possibly, the vector $\boldsymbol{\delta} = (\delta_1, \cdots, \delta_M)$ of the M cluster peculiar velocity shifts. In this case we need an additional constraint to fix $\overline{x_1}$, such as $\sum_j \delta_j = 0$. Other options are discussed in Paper VII. The direction of the eigenvector with the smallest eigenvalue of the matrix $\boldsymbol{V}$ defines the minimum variance hyperplane describing the data distribution, or the slope of the linear correlation in the two-dimensional case. We solve the problem by assuming that both the distributions of the galaxy parameters and of their errors are normal, with covariance matrix $\boldsymbol{V}$ and the error matrices E_i respectively. The first assumption can be verified a posteriori, estimating the likelihood of the best-fitting Gaussian model (see Figs 5 and 13 and Section 3.5.3). The second is based on the error analysis performed in Papers II and III for the EFAR data base. Once the error convolution is performed, the probability density of the

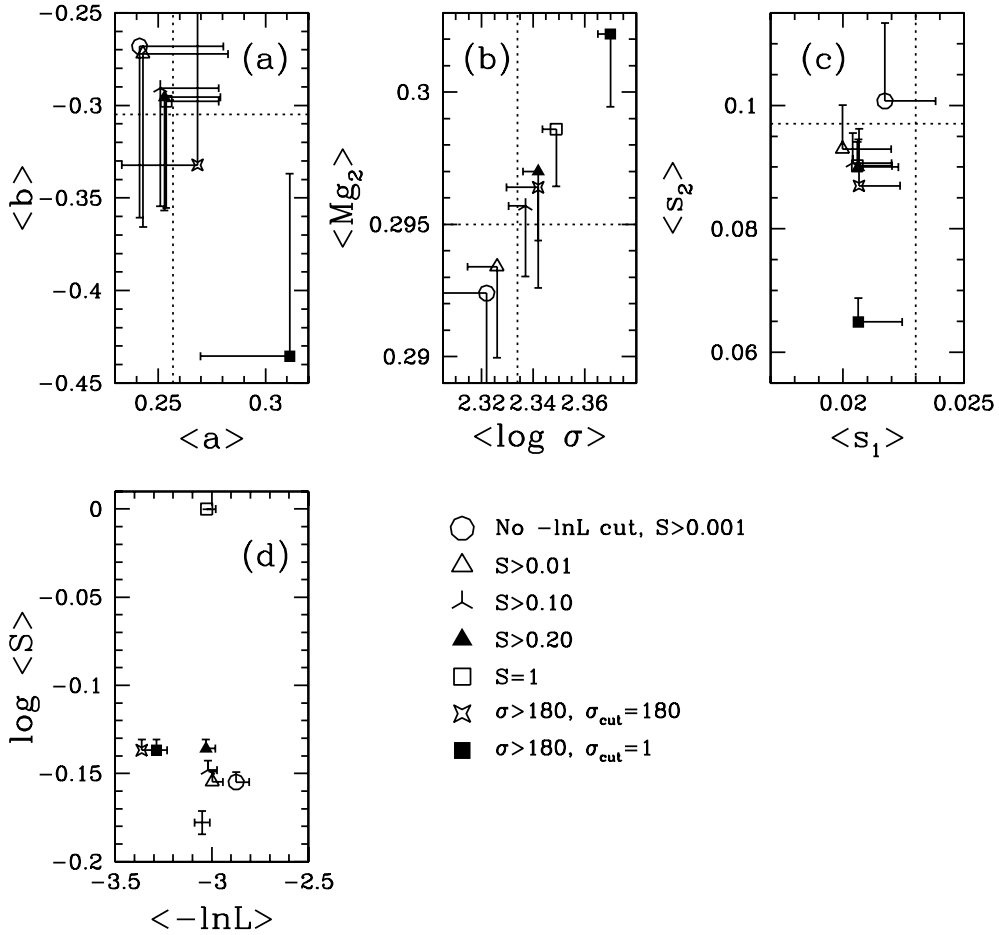

Figure 5. The effects of the selection weighting and of the cut in σ. The plots show the mean values (over 99 simulations) of (a) the slope and zero-point, (b) the mean values, (c) the orthogonal and parallel scatter as determined by the ML algorithm, and (d) the mean logarithmic likelihood and mean selection probability. The error bars show the random errors expected for one simulation. The different types of points refer to the cases discussed in the text. The cross in panel (d) shows the mean values derived for the EFAR sample examined in Paper V, with error bars equal to their rms, divided by the square root of number of the galaxies considered.

vector $\boldsymbol{x}_i$ is

$$P(\boldsymbol{x}_i) = \frac{1}{(2\pi)^{N/2}|\boldsymbol{V}+\boldsymbol{E}_i|^{1/2} f_i} \exp\left[-\frac{1}{2}\hat{\boldsymbol{x}}_i^T(\boldsymbol{V}+\boldsymbol{E}_i)^{-1}\hat{\boldsymbol{x}}_i\right] \times \hat{\theta}(\boldsymbol{A}\hat{\boldsymbol{x}}_i - \boldsymbol{x}_{\rm cut}) \quad (15)$$

where $\hat{\boldsymbol{x}}_i = (x_{i,1} - \bar{x}_1 + \delta_j, x_{i,2} - \bar{x}_2, \cdots, x_{i,N} - \bar{x}_N)$. The function $\hat{\theta}(\boldsymbol{y}) = \prod_k \theta(y_k)$, where $\theta(y) = 1$ if $y \geq 0$ and 0 otherwise, takes into account that parts of the parameter space might not be accessible because of selection effects or explicit cuts. For simplicity, we assume that these cuts are applied to linear combinations of the variables, described by the appropriate matrix $\boldsymbol{A}$. The normalization factor f_i is such that $\int P\,\mathrm{d}^N x = 1$. Following Eadie et al. (1971), we write the likelihood of the observed sample as

$$\mathcal{L} = \prod_i P(\boldsymbol{x}_i)^{w_i}, \quad (16)$$

counting $w_i = 1/S_i$ times galaxies with selection probability S_i We determine $\bar{\boldsymbol{x}}$, V and, possibly, $\boldsymbol{\delta}$ by minimizing $-\ln\mathcal{L}$. In the following sections we describe how this general scheme is implemented in the different cases of interest. In all cases the minimization is performed numerically, using the simplex algorithm (Press et al. 1986). Appendix C discusses the analytical solution of equation (16) for small errors, no explicit cuts and no peculiar velocities.

2.4 The one-dimensional case

The first simple application of the scheme described above is the determination of the mean value μ and the (intrinsic) rms σ of a set of data x_i with errors σ_i, selection weights w_i and subject to the censoring $x > x_{\rm cut}$. Mean values and intrinsic spread of the EFAR photometric ($\log R_{\rm e}$, $[\langle SB_{\rm e}\rangle]$, $\log D_n$, $(B-R)$] or spectroscopic ($\log\sigma$, Mgb, Mg$_2$) parameters, or of the measured cluster peculiar velocities can be estimated in this way.

The simplified version of equation (16) now reads:

$$\mathcal{L} = \prod_i \left\{ \frac{1}{f_{1i}\sqrt{2\pi(\sigma_i^2+\sigma^2)}} \exp\left[-\frac{(x_i-\mu)^2}{2(\sigma_i^2+\sigma^2)}\right] \theta(x_i - x_{\rm cut}) \right\}^{w_i}. \quad (17)$$

Errors are taken into account by convolving the intrinsic distribution with the appropriate Gaussian error distribution. Selection effects are taken into account in equation (17) by counting $1/S_i$ times galaxies with selection probability S_i. The presence of explicit cuts $x_{\rm cut}$ is taken into account (for mild cases;

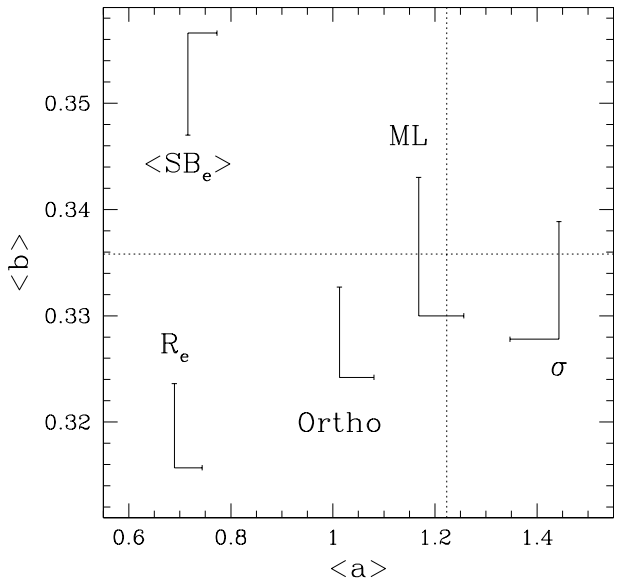

Figure 6. The parameters of the FP relation. The plot shows the mean coefficients $\langle a\rangle$ and $\langle b\rangle$ (over 99 simulations) derived from the linear regressions on $\log R_e$, $\log\sigma$, $\langle SB_e\rangle$, the orthogonal minimization and the ML algorithm. The error bars show the rms. The dotted lines show the input values.

see below) by the normalization correction:

$$f_{1i} = \frac{1}{\sqrt{2\pi(\sigma_i^2+\sigma^2)}}\int_{x_{\rm cut}}^{\infty}\exp\left[-\frac{(x-\mu)^2}{2(\sigma_i^2+\sigma^2)}\right]{\rm d}x$$
$$= 0.5\left\{1-{\rm erf}\left[\frac{x_{\rm cut}-\mu}{\sqrt{2(\sigma_i^2+\sigma^2)}}\right]\right\}. \quad (18)$$

We expect our approach to work in the presence of *mild* cuts with $(x_{\rm cut}-\mu)/\sigma \ll 0$, so that the cut is well away from the mean value of the distribution (see Section 3.2). Appendix A gives the analytical solution of the problem for the limiting case of small errors.

2.5 The two-dimensional case

We turn now to the two-dimensional case, which allows us to investigate correlations between pairs of variables, such as Mg_2–Mgb' examined in Paper II and Mgb'–σ and Mg_2–σ discussed in Paper V. Other relations that we shall not explicitly consider here are the $FP-\log\sigma$ relation (where $FP=\log R_e - b\langle SB_e\rangle$ with $b\approx 0.3$), the $(B-R)-\log\sigma$ relation, the $(B-R)-$Mgb and $(B-R)-Mg_2$ relations, the 'Kormendy' relation $\log R_e$–$\langle SB_e\rangle$, or the $\log D_n$–$\log\sigma$ relation. Note that the EFAR data base measures the photometric parameters in the R band.

Equation (15) reads in this case:

$$P[\boldsymbol{x}_i=(x_{i,1},x_{i,2})] = \frac{|\boldsymbol{\Lambda}_i|^{1/2}}{2\pi f_{2i}}\exp\left[-\frac{1}{2}\hat{\boldsymbol{x}}_i^T(\boldsymbol{V}+\boldsymbol{E}_i)^{-1}\hat{\boldsymbol{x}}_i\right]$$
$$\times\,\theta(x_{i,1}-x_{1cut})\theta(x_{i,2}-x_{2cut}), \quad (19)$$

where the normalization factor f_{2i} is

$$f_{2i} = \frac{|\boldsymbol{\Lambda}_i|^{1/2}}{2\pi}\int_{x_{1cut}}^{\infty}\int_{x_{2cut}}^{\infty}\exp\left(-\frac{1}{2}\hat{\boldsymbol{x}}_i^T\boldsymbol{\Lambda}_i\hat{\boldsymbol{x}}_i\right){\rm d}x\,{\rm d}y = L(h,k,\rho). \quad (20)$$

Here $\boldsymbol{\Lambda}_i=(\boldsymbol{V}+\boldsymbol{E}_i)^{-1}$ and $L(h,k,\rho)$ is the bivariate probability integral (Abramovitz & Stegun 1971) with $h=(x_{1cut}-\bar{x}_1)\times\sqrt{\Lambda_{i,22}(1-\rho^2)}$, $k=(x_{2cut}-\bar{x}_2)\sqrt{\Lambda_{i,11}(1-\rho^2)}$ and $\rho=-\Lambda_{i,12}/\sqrt{\Lambda_{i,11}\Lambda_{i,22}}$. We set $x_{1cut}=-\infty$, $x_{2cut}=-\infty$ (and therefore $f_{2i}=1$) when considering the Mg_2–Mgb' relation, $x_{1cut}=-\infty$, $x_{2cut}=\log\sigma_{\rm cut}$ when studying the Mgb'–σ and Mg_2–σ relations, and $x_{1cut}=FP_{\rm cut}$, $x_{2cut}=\log\sigma_{\rm cut}$ when examining the $FP-\sigma$ relation. In this case we derive $FP_{\rm cut}$ using its relation with D_{Wn}: $FP=0.78\log D_{Wn}-6.14$ (see Paper III). Finally, note that in every case we compute $\boldsymbol{\Lambda}_i$ using the simplifying assumption that the error matrix is diagonal with diagonal terms given by the estimated total errors. For the spectroscopic data these involve two terms, the uncorrelated statistical errors and the correlated errors coming from run-to-run corrections (see Paper II).

Appendix B gives the analytical solution for the limiting case of small errors, no peculiar velocities and no cuts.

2.6 The three-dimensional case

The three-dimensional case allows us to study the EFAR Fundamental Plane. As is well known, early-type galaxies do not fill the three-dimensional space defined by the coordinates $\boldsymbol{x}=(x_1=\log R_e, x_2=\log\sigma, x_3=\langle SB_e\rangle)$, but rather occupy a narrow region around the FP defined by the equation

$$\log R_e - a\log\sigma - b\langle SB_e\rangle = c. \quad (21)$$

Following Section 2.3, we determine the mean values $\overline{\log R_e}$, $\overline{\log\sigma}$ and $\overline{\langle SB_e\rangle}$, the covariance matrix V and the cluster peculiar velocity shifts δ_j (subject to the constraint $\sum_j\delta_j=0$; see Section 2.3) by maximizing the likelihood $\mathcal{L}$:

$$\ln\mathcal{L} = \sum_{\sigma>\sigma_{\rm cut},FP>FP_{\rm cut}}\frac{1}{S_j(\log D^i_{Wn})}\ln P(\boldsymbol{x}_i)$$
$$= -\sum_{\sigma>\sigma_{\rm cut},FP>FP_{\rm cut}}\frac{1}{S_j(\log D^i_{Wn})}[0.5\hat{\boldsymbol{x}}_i^T(\boldsymbol{V}+\boldsymbol{E}_i)^{-1}\hat{\boldsymbol{x}}_i+\ln f_{3i}$$
$$+1.5\ln(2\pi)+0.5\ln|\boldsymbol{V}+\boldsymbol{E}_i|],$$

where

$$f_{3i} = \int P_i\,\theta(\log\sigma-\log\sigma_{\rm cut})\theta(FP-FP_{\rm cut})\,{\rm d}^3x \quad (22)$$

is the fraction of galaxies with $\sigma>\sigma_{\rm cut}$, and $FP>FP_{\rm cut}$. The integral (equation 22) is performed in Appendix E. The offset δ_j between true mean galaxy size $\overline{\log R_e}$, and the mean galaxy size observed for cluster j, $\overline{\log R_e}-\delta_j$, is related to the peculiar velocity of the cluster. In particular, the ratio of the true angular diameter distance of a cluster, D_j, to the angular diameter distance corresponding to its redshift, $D(z_j)$, is

$$\frac{D_j}{D(z_j)} = \frac{{\rm dex}(\overline{\log R_e})}{{\rm dex}(\overline{\log R_e}-\delta_j)} = 10^{\delta_j}. \quad (23)$$

The relation between angular diameter distance and redshift (Weinberg 1972) is given by

$$D(z) = \frac{cz}{H_0(1+z)^2}\frac{1+z+\sqrt{1+2q_0z}}{1+q_0z+\sqrt{1+2q_0z}}. \quad (24)$$

We assume $H_0=50\,{\rm km\,s^{-1}\,Mpc^{-1}}$, $q_0=0.5$, and compute all redshifts and peculiar velocities in the CMB frame of reference. The peculiar velocity of the cluster, V_j, is then

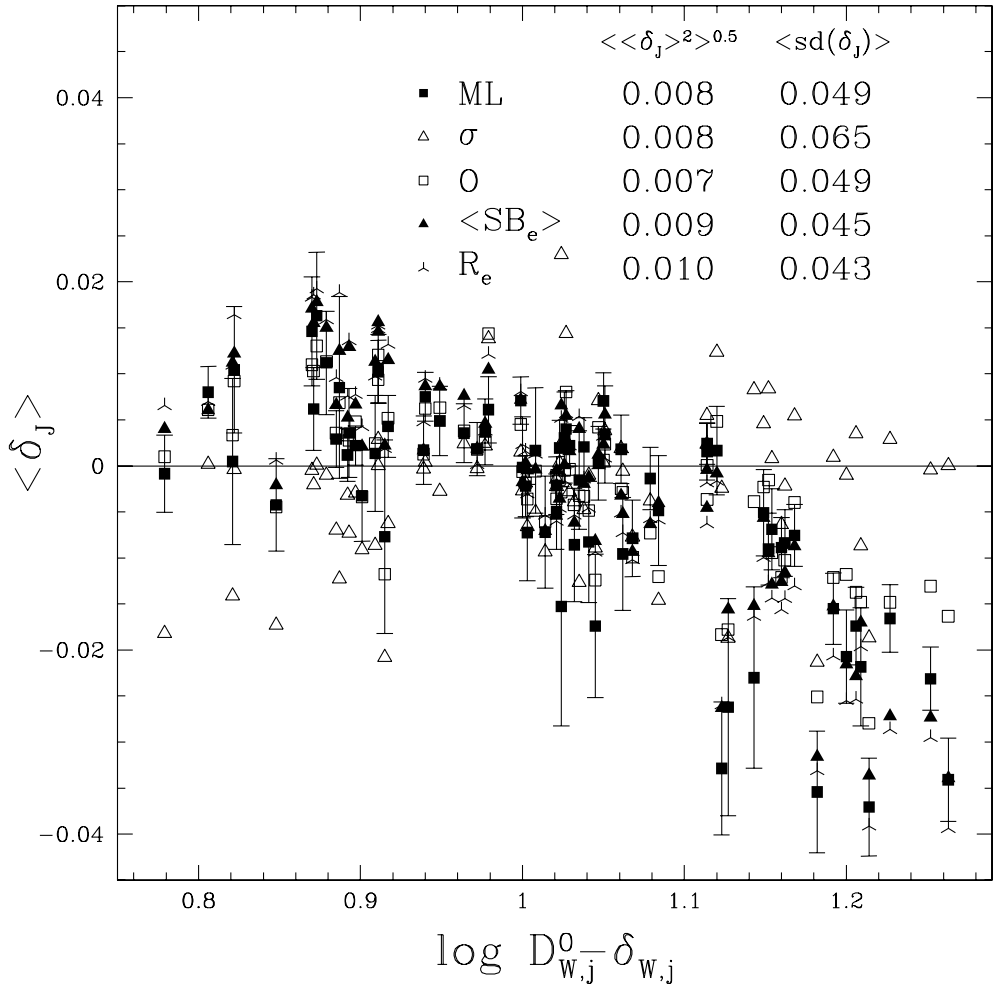

Figure 7. The peculiar velocity shifts of the EFAR clusters. The plot shows the mean (over 99 simulations) peculiar velocity shifts $\langle\delta_j\rangle$ as a function of $\log D^0_{W,j} - \delta_{W,j}$ (see equation 14, with $D^0_{W,j}$ in kpc). The methods used are the linear regressions on $\log R_e$ (triangular crosses), $\log\sigma$ (open triangles), $\langle SB_e\rangle$ (filled triangles), the orthogonal minimization (open squares) and the ML algorithm (filled squares). The error bars show the errors on the mean, the rms are ≈10 times larger. The numbers give the rms over the EFAR clusters of the mean differences $\langle\delta_j\rangle$ over the 99 simulations and the mean over the 99 simulations of the standard deviation (over the EFAR clusters) of the δ_j values with $\log D^0_{W,j} - \delta_{W,j} < 1.18$. The input peculiar velocity shifts are all zero.

obtained as

$$V_j = \frac{cz_j - cz(D_j)}{1 + z(D_j)}, \tag{25}$$

where $z(D_j)$ is the redshift corresponding to the true distance D_j through the inverse of equation (24).

The error matrix $\boldsymbol{E}_i$ is given by

$$\boldsymbol{E}_i = \begin{pmatrix} \delta r_i^2 & 0 & \dfrac{(1+\alpha^2)\delta r_i^2 - \delta FP_i^2}{\alpha(1+\alpha^2)} \\ 0 & \sigma_s^2 & 0 \\ \dfrac{(1+\alpha^2)\delta r_i^2 - \delta FP_i^2}{\alpha(1+\alpha^2)} & 0 & \dfrac{(\alpha^2-1)\delta FP_i^2 + (1+\alpha^2)\delta r_i^2}{\alpha^2(1+\alpha^2)} + \delta ZP_i^2 \end{pmatrix}, \tag{26}$$

where δr_i is the error on $\log R_{e,i}$, δFP_i is the error on the combined quantity $FP_i = \log R_{e,i} - \alpha\langle SB_{e,i}\rangle$, with $\alpha \approx 0.3$, and δZP_i is the photometric zero-point error (see Papers III and IV). Note that in principle b might be different from α. The quantity $\delta u_i = \sqrt{(\alpha^2-1)\delta FP_i^2 + (1+\alpha^2)\delta r_i^2/\alpha^2(1+\alpha^2)}$ is the error on the effective surface brightness coming from the fitting. See Appendix D for a derivation of these formulae. The error σ_s on $\log\sigma$ combines the uncorrelated and correlated errors (see Paper II).

It is worth noting that the eigenvectors $\boldsymbol{v}_1$, $\boldsymbol{v}_2$, $\boldsymbol{v}_3$ of the $\boldsymbol{V}$ matrix can be written to a close approximation as a function of the parameters a and b defining the Fundamental Plane of equation (21):

$$\begin{aligned} \boldsymbol{v}_1 &= \hat{\boldsymbol{x}}_1 - a\hat{\boldsymbol{x}}_2 - b\hat{\boldsymbol{x}}_3, \\ \boldsymbol{v}_2 &= \hat{\boldsymbol{x}}_1 + \hat{\boldsymbol{x}}_3/b, \\ \boldsymbol{v}_3 &= -\hat{\boldsymbol{x}}_1/b - (1+b^2)\hat{\boldsymbol{x}}_2/(ab) + \hat{\boldsymbol{x}}_3, \end{aligned} \tag{27}$$

where $\boldsymbol{v}_1$ measures the displacement from the FP, and $\boldsymbol{v}_2$ and $\boldsymbol{v}_3$ are two orthogonal vectors in the FP. The absence of a $\hat{\boldsymbol{x}}_2$ component in $\boldsymbol{v}_2$ is remarkable. In Paper VII (equation 12) we fit for the coefficient of $\log\sigma$ in the second principal component and find that it is small. In Section 3.5.2 (equation 30) we show that it is compatible with zero within the statistical uncertainties.

In the following we indicate the rms spread around the vectors $\boldsymbol{v}_1$, $\boldsymbol{v}_2$ and $\boldsymbol{v}_3$ with $\overline{\sigma_1}$, $\overline{\sigma_2}$ and $\overline{\sigma_3}$, respectively.

3 MONTE CARLO SIMULATIONS

The algorithms described in the previous section have been

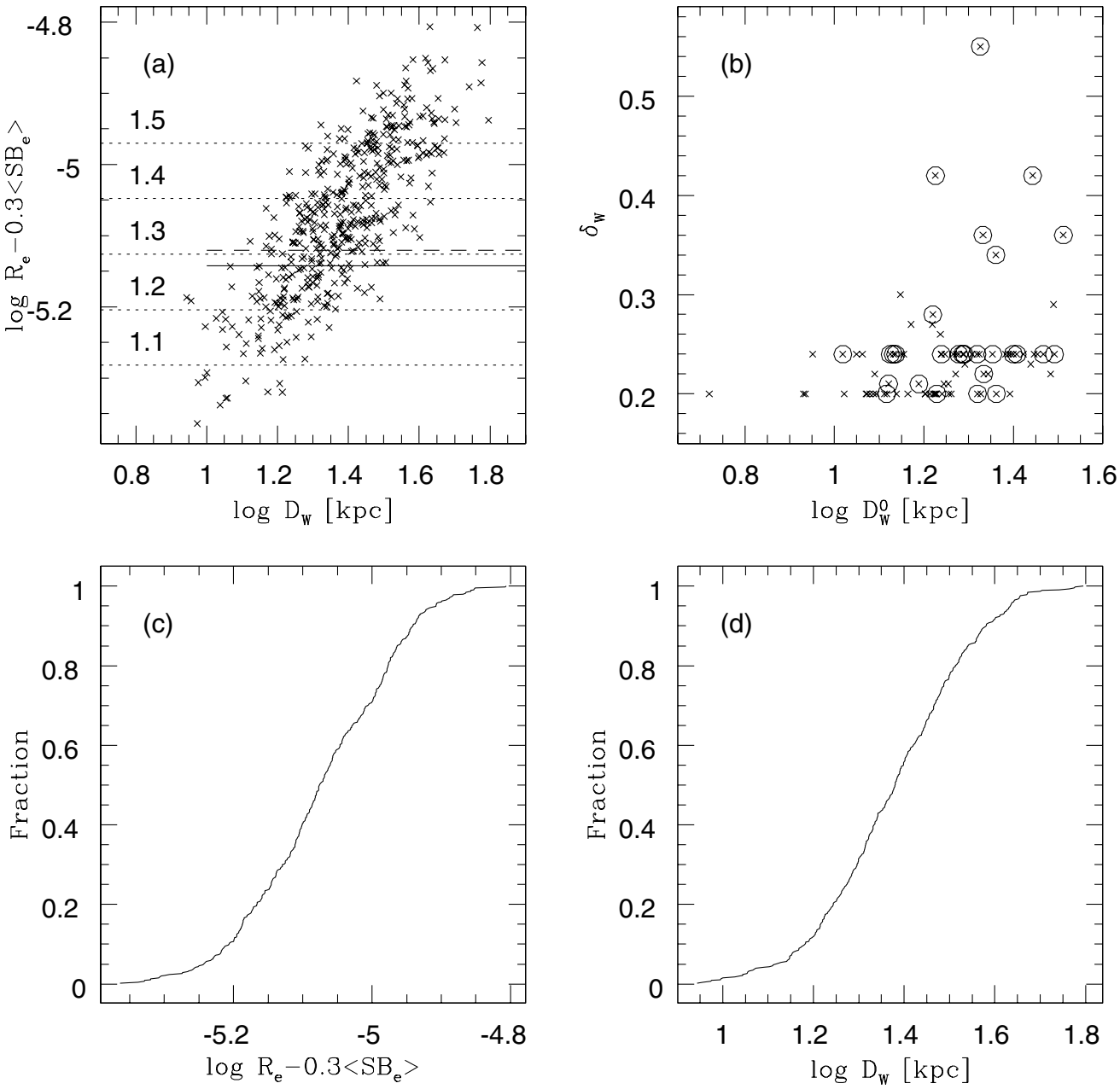

Figure 8. One of the simulations of Section 3.5.1. Panel (a) shows the correlation between $\log R_e - 0.3\langle SB_e\rangle$ and $\log D_W$. The full line shows the input mean value $\overline{\log R_e} - 0.3\overline{\langle SB_e\rangle}$, the dashed dashed line the value derived by the ML algorithm. The dotted lines correspond to the given values of $\log D_{W\rm cut}$. Panel (b) shows the values of the selection parameters $\log D^0_{W,j}$ and $\delta_{W,j}$. The 29 best clusters are shown circled. Panel (c) shows the cumulative distribution of $\log R_e - 0.3\langle SB_e\rangle$ values. Panel (d) shows the cumulative distribution of $\log D_W$.

extensively tested on mock catalogues of the EFAR data base. After describing how these catalogues are generated (Section 3.1), we proceed to test cases of increasing complexity. We start with the one-dimensional σ distribution (Section 3.2), as an example of the influence of hard cuts on the mean and rms of the sample. Then we consider the Mg_2–Mgb' relation (Section 3.3), where distance-independent quantities not subject to explicit cuts are involved. We turn in Section 3.4 to the Mg–σ relations, where no data points with central velocity dispersions smaller than the resolution limit can be present. Finally, we examine the three-dimensional case of the Fundamental Plane (Section 3.5), where one distance-dependent quantity ($\log R_e$) is correlated against two distance-independent quantities ($\log\sigma$ and $\langle SB_e\rangle$), with distance-dependent selection limits and the presence of cluster peculiar velocities.

3.1 Mock catalogues of the EFAR data base

We generate mock catalogues of the EFAR data base using the Gaussian distribution functions that are reconstructed from the data (see Papers II, V and VII, and Case 0 of Table 1). We specify the values of $\overline{\log R_e}$, $\overline{\log\sigma}$, $\overline{\langle SB_e\rangle}$, $\overline{Mg_2}$ and $\overline{Mgb'}$, the coefficients of the FP and the slopes of the Mg_2–σ and Mgb'–σ relations, and the dispersions of the distributions in the orthogonal directions. We generate one entry in the mock catalogue for each early-type galaxy present in the data base. As a first step, we extract the

Table 1. The mean values (over 99 simulations) of the parameters of the Fundamental Plane derived for various cases.

Case	N_{cl}	N_{gal}	a	b	c	$\overline{\log R_e}$	$\overline{\log \sigma}$	$\overline{\langle SB_e \rangle}$	σ_1	σ_2	σ_3	Notes
0	29	255	1.223	0.336	−8.666	0.770	2.304	19.71	0.064	1.995	0.610	standard fit Paper VII
1	29	240	1.150	0.329	−8.360	0.808	2.311	19.77	0.058	1.946	0.643	standard fit 1000 simulations
1	29	240	1.168	0.330	−8.418	0.799	2.310	19.76	0.058	1.950	0.644	standard fit 99 simulations
2	26	224	1.175	0.330	−8.427	0.797	2.308	19.76	0.058	1.954	0.648	uses clusters with $N_{gal} \geq 6$
3	5	80	1.222	0.331	−8.563	0.774	2.303	19.72	0.066	1.963	0.661	uses clusters with $N_{gal} \geq 10$
4	13	144	1.200	0.331	−8.517	0.791	2.305	19.76	0.061	1.948	0.653	uses clusters with $N_{gal} \geq 8$
5	18	176	1.194	0.331	−8.506	0.789	2.304	19.75	0.060	1.948	0.655	uses clusters with $N_{gal} \geq 7$
6	35	269	1.164	0.330	−8.401	0.803	2.311	19.76	0.057	1.955	0.643	uses clusters with $N_{gal} \geq 5$
7	47	317	1.148	0.329	−8.345	0.809	2.314	19.77	0.056	1.959	0.637	uses clusters with $N_{gal} \geq 4$
8	62	364	1.138	0.329	−8.325	0.810	2.314	19.77	0.055	1.960	0.638	uses clusters with $N_{gal} \geq 3$
9	29	247	1.096	0.328	−8.203	0.818	2.325	19.75	0.057	1.976	0.580	no D_W cut is applied
10	29	247	1.097	0.328	−8.205	0.818	2.325	19.75	0.057	1.975	0.580	$D_{Wcut} = 6.3$ kpc
11	29	233	1.227	0.333	−8.611	0.762	2.283	19.76	0.059	1.926	0.711	$D_{Wcut} = 14.1$ kpc
12	29	219	1.266	0.334	−8.729	0.705	2.237	19.78	0.060	1.903	0.783	$D_{Wcut} = 15.9$ kpc
13	29	240	1.141	0.329	−8.325	0.852	2.339	19.80	0.058	1.932	0.614	uses no selection weighting
14	29	231	1.131	0.327	−8.275	0.828	2.325	19.78	0.057	1.941	0.618	uses galaxies with $S_i > 0.2$
15	29	243	1.195	0.332	−8.512	0.771	2.294	19.74	0.058	1.943	0.673	uses galaxies with $S_i > 0.001$
16	29	223	1.165	0.330	−8.414	0.799	2.309	19.76	0.058	1.944	0.649	uses galaxies with $\delta\sigma < 0.1$
17	29	171	1.054	0.330	−8.160	0.786	2.317	19.72	0.026	1.484	0.506	excludes galaxies with $\ln \mathscr{L} < 0$
18	29	240	1.158	0.328	−8.356	0.803	2.315	19.76	0.057	1.978	0.646	uses uniform errors for all galaxies
19	29	240	1.168	0.331	−8.443	0.807	2.312	19.77	0.058	2.207	0.478	also fit third axis of FP
20	29	228	1.106	0.326	−8.187	0.818	2.320	19.77	0.055	1.955	0.608	all $\log D_W^0$ shifted by +0.1
21	29	243	1.179	0.330	−8.454	0.810	2.316	19.77	0.059	1.943	0.652	all $\log D_W^0$ shifted by −0.1
22	29	243	1.177	0.330	−8.437	0.803	2.313	19.76	0.059	1.947	0.646	all δ_W shifted by +0.1
23	29	229	1.129	0.328	−8.291	0.817	2.319	19.77	0.055	1.943	0.625	all δ_W shifted by −0.1
24	29	239	1.185	0.331	−8.488	0.797	2.309	19.77	0.059	1.923	0.648	random peculiar velocity field
25	29	237	1.183	0.335	−8.563	0.791	2.307	19.78	0.058	1.926	0.653	LP dipole plus random component
26	29	238	1.194	0.332	−8.531	0.788	2.307	19.78	0.057	1.950	0.654	SMAC dipole plus random component
27	29	240	1.170	0.330	−8.425	0.798	2.310	19.77	0.057	1.961	0.643	pure LP dipole
28	29	240	1.161	0.333	−8.464	0.796	2.309	19.77	0.058	1.940	0.642	pure SMAC dipole
45	29	240	1.142	0.328	−8.311	0.804	2.312	19.76	0.058	1.986	0.665	FP uniform distribution
46	29	240	1.156	0.336	−8.512	0.805	2.312	19.77	0.059	1.698	0.633	Error uniform distribution
47	29	239	1.146	0.336	−8.482	0.812	2.314	19.78	0.058	1.740	0.643	FP and Error uniform distribution

triplet ($\log R_e$, $\log \sigma$, $\langle SB_e \rangle$), using equation (27) to specify the directions of the principal components of the distribution in the ($\log R_e$, $\log \sigma$, $\langle SB_e \rangle$) space. We determine the corresponding value of the D_n diameter using the relation (a second-order approximation to the equation 4 of van Albada, Bertin & Stiavelli 1993):

$$\log D_n = \log 2R_e - 0.289\Delta - 0.019\Delta^2, \quad (28)$$

where $\Delta = \langle SB_e \rangle - 20$ matches the surface brightness used to determine the EFAR D_n diameters (see Paper III). Only galaxies with a dominant exponential component in the luminosity profile deviate strongly from equation (28). We simulate the effects of cluster peculiar velocities by adding cluster-dependent shifts to the extracted values of $\log R_e$ and $\log D_n$. We convert $\log D_n$ into $\log D_W$ using the relation $\log D_W = (\log D_n - 0.27)/0.8$ (see Paper III) and add the 0.09-dex rms random scatter of the relation. We compute the corresponding selection probability, according to the selection parameters of the cluster being extracted and its (redshift) distance, and test if the extracted data points should be in the sample. If this is the case, the values of Mg_2 and Mgb' are extracted following the (two-dimensional) Gaussian distribution computed at $\log \sigma$. Measurement errors are assigned following the EFAR catalogue, so extracted object N has the total errors of object N of the data base, taking into account the correlated terms of the total errors (see Paper II) properly. Therefore the error on σ, Mg_2 and Mgb' for the extracted object N is computed by considering the spectroscopic runs where object N of the data base was observed, generating proper run correction errors and determining the final error taking into account the run weights.

Finally, three additional sets of simulations (Cases 45, 46 and 47 of Table 1) are generated using uniform instead of Gaussian distributions, and zero input peculiar velocity fields. Following the procedure described above, we consider the values of $\overline{\log R_e}$, $\overline{\log \sigma}$, $\overline{\langle SB_e \rangle}$, σ_1, σ_2 and σ_3 and of the coefficients of the FP as Case 0 of Table 1, and equation (27) to specify the directions of the principal components of the distribution in the ($\log R_e$, $\log \sigma$, $\langle SB_e \rangle$) space. For Case 45 we add Gaussian errors generated as above, but we assume a uniform distribution of the FP parameters, extending $\pm\sqrt{3}\sigma_1$, $\pm\sqrt{3}\sigma_2$, $\pm\sqrt{3}\sigma_3$ in the $\boldsymbol{v}_1$, $\boldsymbol{v}_2$, $\boldsymbol{v}_3$ directions respectively from the mean values. This choice preserves the covariance matrix of the Gaussian case. For Case 46 we use Gaussian distributions of the FP parameters, but measurements errors drawn using a uniform distribution extending $\pm\sqrt{3}$ the estimated rms. For Case 47 we use uniform distributions for both the FP parameters and the errors, with the $\sqrt{3}$ scaling as above.

3.2 One-dimensional distributions

As a first example we discuss the use of the one-dimensional algorithm of Section 2.4. We generated 99 samples of the EFAR data base (see Paper V) and considered the σ distribution. Fig. 1 shows the results as a function of the cut applied to the data. For cuts well below the true mean of the distribution, the ML algorithm with or without normalization correction estimates the mean and rms of the distribution with small bias. The simple mean, which does not take into account the selection weights of the data, slightly overestimates the true value, because objects with small σ tend to have small selection probabilities. The simple rms, corrected for measurement errors as suggested by Arkitas &

Table 2. The rms values (over 99 simulations) of the parameters of the Fundamental Plane derived for various cases.

Case	dN_{cl}	dN_{gal}	da	db	dc	$d\overline{\log R_e}$	$d\overline{\log \sigma}$	$d\overline{\langle SB_e \rangle}$	$d\sigma_1$	$d\sigma_2$	$d\sigma_3$	Notes
1	0	4	0.089	0.013	0.354	0.025	0.016	0.060	0.006	0.158	0.067	standard fit 1000 simulations
1	0	4	0.089	0.013	0.347	0.027	0.018	0.048	0.006	0.168	0.066	standard fit 99 simulations
2	1	10	0.093	0.014	0.360	0.027	0.018	0.048	0.006	0.172	0.068	uses clusters with $N_{gal} \geq 6$
3	1	8	0.141	0.021	0.533	0.047	0.028	0.087	0.011	0.246	0.108	uses clusters with $N_{gal} \geq 10$
4	1	10	0.117	0.016	0.445	0.038	0.025	0.063	0.008	0.198	0.089	uses clusters with $N_{gal} \geq 8$
5	1	9	0.106	0.015	0.411	0.033	0.022	0.057	0.007	0.179	0.079	uses clusters with $N_{gal} \geq 7$
6	2	9	0.085	0.013	0.338	0.026	0.017	0.044	0.006	0.156	0.062	uses clusters with $N_{gal} \geq 5$
7	1	7	0.079	0.012	0.328	0.022	0.014	0.043	0.005	0.143	0.054	uses clusters with $N_{gal} \geq 4$
8	2	6	0.074	0.012	0.309	0.022	0.014	0.041	0.005	0.136	0.054	uses clusters with $N_{gal} \geq 3$
9	0	3	0.067	0.011	0.274	0.019	0.009	0.048	0.005	0.162	0.039	no D_W cut is applied
10	0	3	0.067	0.011	0.275	0.018	0.009	0.046	0.005	0.162	0.039	$D_{Wcut} = 6.3$ kpc
11	0	5	0.097	0.014	0.380	0.041	0.028	0.048	0.007	0.167	0.075	$D_{Wcut} = 14.1$ kpc
12	0	6	0.097	0.014	0.366	0.068	0.055	0.059	0.007	0.157	0.109	$D_{Wcut} = 15.9$ kpc
13	0	4	0.068	0.011	0.281	0.016	0.010	0.037	0.005	0.122	0.048	uses no selection weighting
14	0	5	0.077	0.013	0.323	0.021	0.012	0.046	0.006	0.149	0.057	uses galaxies with $S_i > 0.2$
15	0	3	0.101	0.014	0.385	0.047	0.032	0.064	0.006	0.179	0.104	uses galaxies with $S_i > 0.001$
16	0	3	0.093	0.013	0.362	0.029	0.019	0.048	0.006	0.171	0.070	uses galaxies with $\delta\sigma < 0.1$
17	0	10	0.150	0.026	0.667	0.030	0.017	0.064	0.010	0.268	0.080	excludes galaxies with $\ln \mathscr{L} < 0$
18	0	4	0.106	0.014	0.385	0.031	0.024	0.047	0.009	0.175	0.114	uses uniform errors for all galaxies
19	0	4	0.087	0.013	0.333	0.025	0.017	0.049	0.006	0.161	0.040	also fit third axis of FP
20	0	5	0.082	0.014	0.359	0.022	0.014	0.054	0.006	0.172	0.059	all $\log D_W^0$ shifted by +0.1
21	0	3	0.086	0.012	0.325	0.027	0.018	0.042	0.006	0.145	0.069	all $\log D_W^0$ shifted by −0.1
22	0	3	0.087	0.012	0.329	0.027	0.018	0.041	0.006	0.146	0.067	all δ_W shifted by +0.1
23	0	5	0.086	0.015	0.379	0.026	0.016	0.056	0.006	0.174	0.064	all δ_W shifted by −0.1
24	0	4	0.087	0.014	0.357	0.032	0.020	0.059	0.006	0.127	0.068	random peculiar velocity field
25	0	4	0.096	0.014	0.410	0.030	0.019	0.058	0.006	0.156	0.072	LP dipole plus random component
26	0	4	0.078	0.013	0.354	0.029	0.016	0.063	0.005	0.139	0.065	SMAC dipole plus random component
27	0	3	0.087	0.016	0.398	0.028	0.019	0.057	0.006	0.170	0.070	pure LP dipole
28	0	3	0.096	0.012	0.378	0.029	0.019	0.056	0.005	0.147	0.079	pure SMAC dipole
45	0	4	0.096	0.011	0.356	0.027	0.020	0.045	0.005	0.126	0.072	FP uniform distribution
46	0	3	0.093	0.016	0.402	0.022	0.015	0.045	0.006	0.138	0.058	Error uniform distribution
47	0	4	0.100	0.017	0.438	0.031	0.021	0.053	0.005	0.116	0.073	FP and Error uniform distribution

Bershadi (1996), underestimates slightly the true values, not taking into account the selection weights. As the cut is increased to values similar to the true mean of the distribution, the ML algorithm with normalization correction estimates the mean and rms with small bias, with the statistical errors (for the single sample $\sqrt{99}$ larger than the error bars shown) becoming increasingly large. With cuts one sigma or more larger than the mean, the ML algorithm starts to fail, biasing the mean low and the sigma high. However, the bias is always smaller than the random errors. Both the ML algorithm without normalization correction and the simple estimates bias the mean to larger values and the rms to smaller values.

As it is well known (Press et al. 1986), the likelihood analysis offers in principle a simple recipe for computing confidence intervals for the fitted parameters. The $n\sigma$ one-dimensional confidence interval is fixed by the contours of the likelihood function, where

$$\ln \mathcal{L}_{max} - \ln \mathcal{L} = 0.5n^2. \quad (29)$$

Fig. 2 shows four contours of constant likelihood in the (μ,σ) plane for one of the simulations in Fig. 1 analysed by the ML algorithm with normalization correction $\sigma_{cut} = 100$, 150, 200 and 250 km s^{-1} respectively. The thick error bars mark the position of μ and σ, averaged over the 99 simulations in Fig. 1, and show their rms. A straight application of equation (29) would produce $n = 1$ one-dimensional confidence intervals for μ and σ a factor $\approx$2 smaller than the rms measured by the simulations. Inspection of equation (16) reveals that since the mean weighting of each galaxy is $\langle w \rangle = \Sigma_i w_i/N$, the $n\sigma$ one-dimensional confidence interval is reached at a $0.5\langle w \rangle n^2$ distance from the ML value. This factor is taken into account in Fig. 1, where the scaled $n = 1$ one-dimensional confidence intervals match approximately the rms measured by the simulations. The two-dimensional 1σ confidence region, set by $\Delta \ln \mathcal{L} = 1.15\langle w \rangle$, is slightly larger. However, Fig. 13 shows that the mean weight fluctuates in the range 1.5–2, making the estimate of confidence intervals from the likelihood function uncertain for a given data set. In addition, this analysis does not allow us to study the small residual biases in the ML estimates. Therefore, in the following we will estimate confidence intervals and residual biases using Monte Carlo simulations only.

3.3 The Mg_2–Mgb' relation

The simplest test of the two-dimensional algorithm is performed by considering the Mg_2–Mgb' relation. We generated 99 samples without taking into account the EFAR selection function. The input parameters are the ones derived in Paper II. Two cases are examined, one with a realistic error distribution and one with a factor of 5 smaller errors. Fig. 3(d) shows one of the realizations with realistic errors. Fig. 3(g) shows the results averaged over the 99 simulations. In both the cases of small and realistic errors the ML algorithm retrieves the input parameters with small biases and with small errors. The $Y - X$, $X - Y$ and bisector regressions fail to derive the correct slopes and zero-points, because of the finite orthogonal scatter and the non-negligible errors. When the method of Akritas & Bershady (1996) is used to correct for the errors (dotted cross), the $Y - X$ result is less biased, but with large random errors. Note that the method cannot be used when selection weights are present. The orthogonal residual fit gives a slightly biased answer as expected from equation (B6), with a

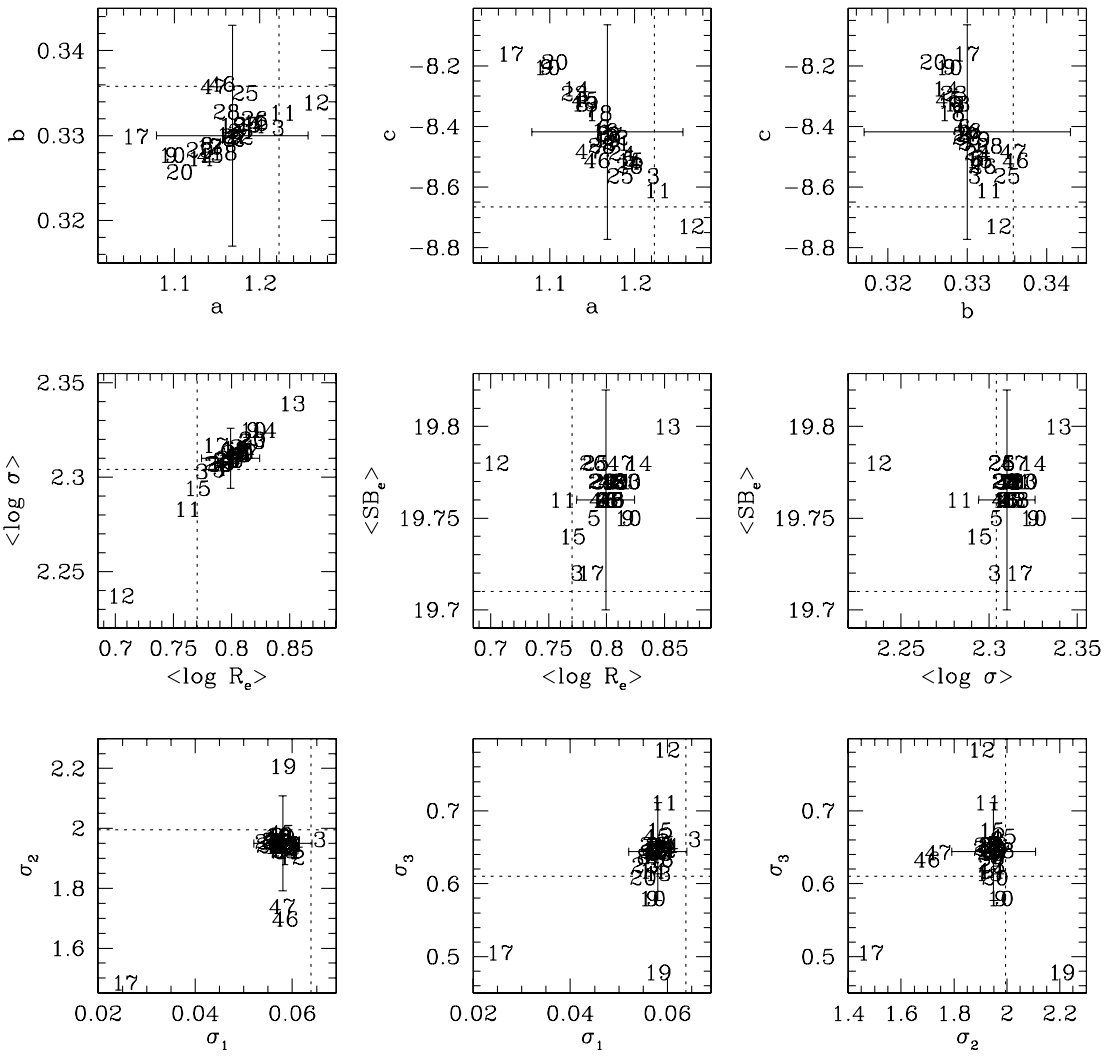

Figure 9. The fitted FP parameters for each case in Table 1, showing the distributions and correlations for various pairs of parameters. Each case is numbered as in the table. The dotted lines show the input parameters. The error bars show the rms over 1000 simulations derived for Case 1.

nearly perfect result when the errors are small. As expected from equation (12), the errors on a and b are perfectly anticorrelated.

Figs 3(a), (b), (c), (e) and (f) show the histograms of the results of the ML parameters (for the case of realistic errors). Not only are the slope and the mean values determined with high precision, but so also is the intrinsic scatter (orthogonal and parallel to the relation), despite the non-negligible measurement errors (the observed scatter orthogonal to the relation is more than twice that of the intrinsic one).

3.4 The Mg_2–σ and Mgb'–σ relations

The tests on the Mg_2–σ and Mgb'–σ relations were performed using the EFAR mock catalogues with realistic error distributions. The input parameters are the ones derived in Paper V. Fig. 4(a) shows one of these Mg_2–σ realizations. Data at small σ or Mg_2 have larger selection weights. Fig. 4(b) shows that the spread in the errors is large. The distribution of the selection probabilities (Fig. 4c) has a peak at the completeness value ($S = 1$), with a prominent tail down to the selection probability cut ($S = 0.1$). The effective number of data points per selection weight bin (Fig. 4d) is approximately constant. The simulations (full lines) reproduce closely the observed data set (dotted lines) analysed in Paper V.

Fig. 4(e) shows the slopes and zero-points derived from the various regressions and the ML algorithm, considering points with selection probabilities larger than 0.1 for the Mg_2–σ relation. As already seen in Section 3.3, the regressions give biased results due to the errors (as discussed in Section 2.1), while the ML algorithm is nearly free of biases and accurate.

Fig. 5 illustrates the effects of the selection weighting and of the cut in σ. When the analysis is performed including all the available data points to the largest selection weights and without any likelihood cut (open circle), the parallel and orthogonal scatters are derived best. However, the rms scatter on all the parameters is rather large, because the presence of some data points with very high weights can bias the analysis of some realizations. It is therefore prudent to limit the analysis to data points with weights not larger than 10 (e.g., $S_i > 0.1$) and clip points with low likelihood ($-\ln \mathcal{L} > 0$, triangular stars). This allows us to determine the slope and the zero-point of the relation with small biases and with small variance. The price is a slight underestimate of the orthogonal and parallel spread, σ_1 and σ_2. Fitting points with weights not larger than 5 (filled triangles) and

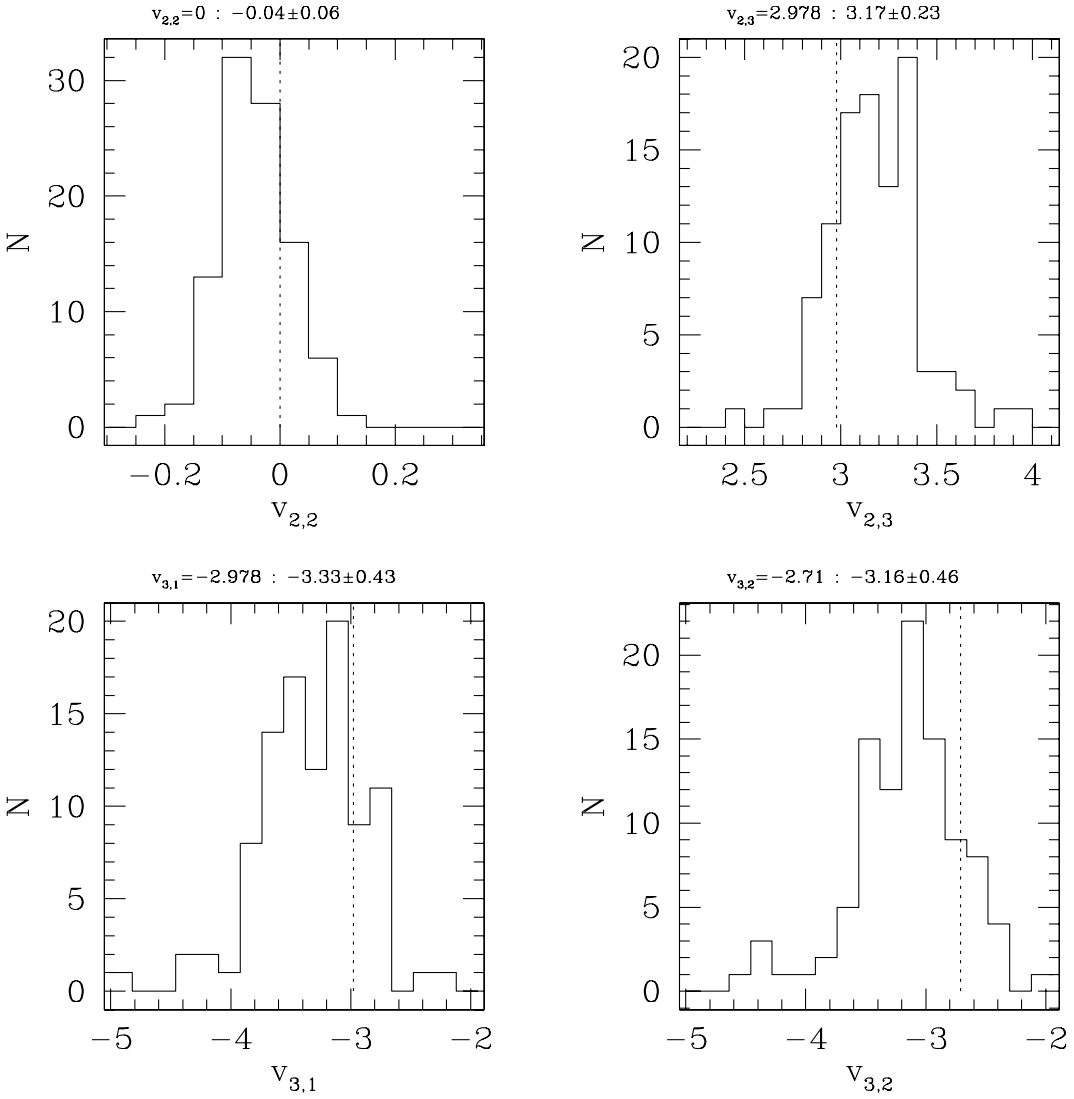

Figure 10. The distributions of the second and third components of vector $\boldsymbol{v}_2$, and the first and second components of vector $\boldsymbol{v}_3$ (see equation 30) resulting from fitting 99 simulations allowing the orientation of the major axis of the galaxy distribution within the FP to be a free parameter (Case 19). The input parameters of the simulations are given at the head of each panel (and indicated by the vertical dotted line), followed by the mean and rms of the fits to the simulations.

the same likelihood clipping, one observes that the mean quantities $\overline{\mathrm{Mg}_2}$ and $\overline{\log\sigma}$ are biased to systematically larger values, because the small galaxies have on average larger selection weights (see Fig. 5). The largest bias in the mean quantities is obtained weighting all data points equally, independently of the selection (open square). These tests justify the procedure adopted in Paper V to study the Mg_2–σ and $\mathrm{Mg}b'$–σ relations, where we consider galaxies with $S_i > 0.1$ and apply likelihood clipping.

To illustrate the effect of the cut in σ, we examine the extreme case where only galaxies with $\sigma > 180\,\mathrm{km\,s^{-1}}$ are considered in the analysis. When no correction is applied (filled square), the slope and the zero-point of the relation are slightly biased, the mean quantities $\overline{\log\sigma}$ and $\overline{\mathrm{Mg}_2}$ are biased to larger values, while the parallel spread is biased low (similar to what is seen in Fig. 1). The biases are fully corrected for when we apply the normalization corrections appropriate for $\sigma_{\mathrm{cut}} = 180\,\mathrm{km\,s^{-1}}$ (open star), with a slight increase of the variance. The cut applied to the EFAR data base ($\sigma > 100\,\mathrm{km\,s^{-1}}$) is in any case low compared to the mean value of the sample. Finally, plot (d) in Fig. 5 shows the mean values and rms (over the simulations) of the mean (over the data points) logarithmic likelihood and selection probability. The cross shows the values derived for the EFAR sample examined in Paper V, with error bars equal to their rms divided by the square root of number of the galaxies considered. The simulations match the mean likelihood of the EFAR sample within the estimated errors, justifying a posteriori the assumption of a Gaussian distribution. The mean selection probability of the simulations (see Fig. 5) is only slightly larger than that of the real sample.

Similar results are obtained when considering the $\mathrm{Mg}b'$–σ relation. Fig. 4(f) shows again that the linear regressions give biased results. The $Y - X$ and orthogonal fitting are very similar, because of the shallow slope. The ML with probability cut $S_i > 0.1$ and likelihood clipping gives nearly unbiased results. Histograms similar to Figs 3(a)–(f) for the Mg_2–σ and $\mathrm{Mg}b'$–σ relations have been already presented in Paper V.

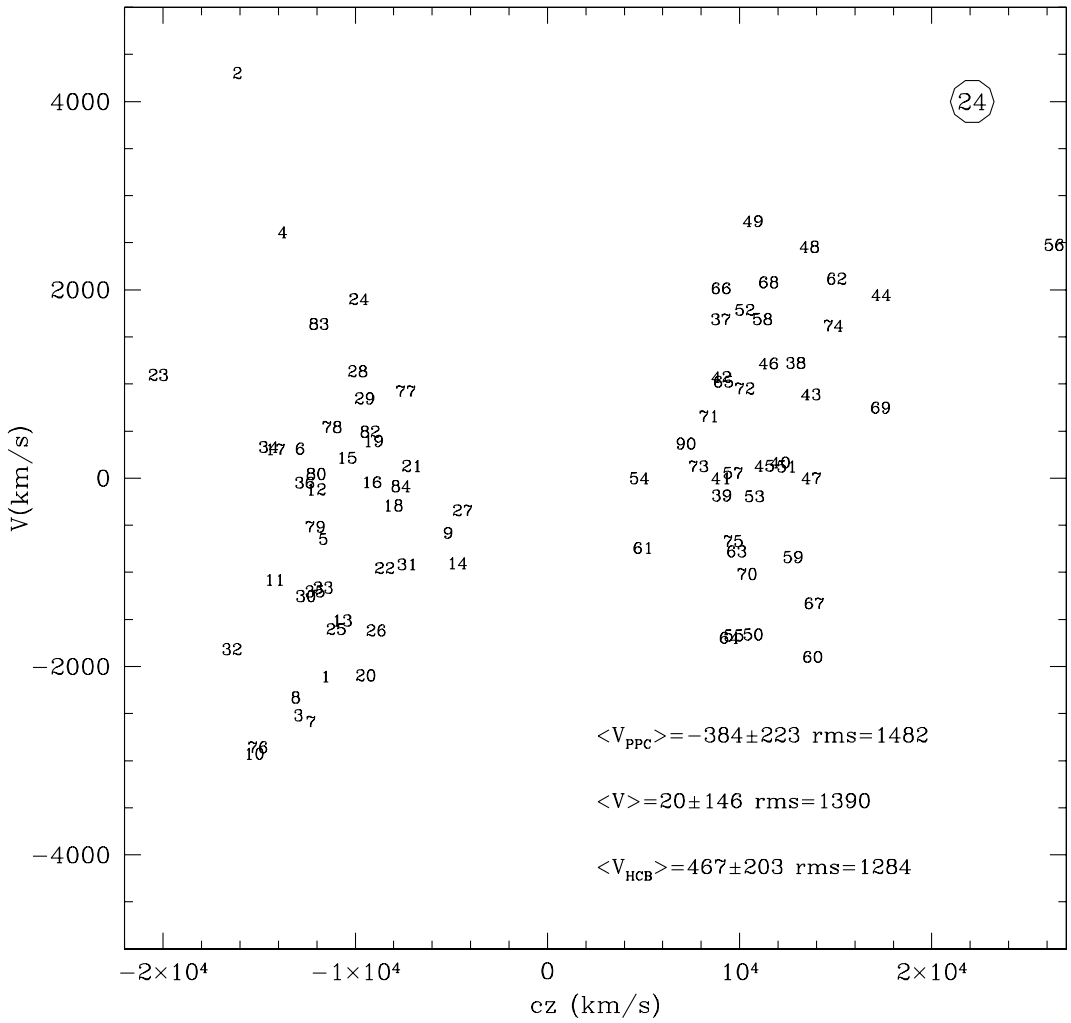

Figure 11. The input peculiar velocity field of the simulations of Case 24 of Table 1. Each cluster is identified by its Cluster Assignment Number (hereafter CAN; see Paper II). Clusters in the southern Galactic hemisphere are plotted at negative redshifts. The resulting mean velocities (with statistical errors) for the whole sample, the clusters at positive (the Hercules–Corona–Borealis sample, HCB) and negative Galactic longitudes (the Pisces–Perseus–Cetus sample, PPC) are given with their rms.

3.5 The Fundamental Plane

In this section we describe the tests of the ML algorithm used to derive the FP solution of Paper VII and the peculiar velocities of the EFAR sample. In Section 3.5.1 we assess the superiority of the ML algorithm with respect to the linear regression methods, when the a and b parameters of the FP are determined. In Section 3.5.2 we study the precision of the FP parameters derived using the ML algorithm, justifying the strategy adopted in Paper VII. Section 3.5.3 justifies a posteriori the assumption of a Gaussian distribution of galaxies in the ($\log R_e$, $\log\sigma$, $\langle SB_e\rangle$) space. Section 3.5.4 tests the bias correction scheme for the peculiar velocities adopted in Paper VII. Finally, Section 3.5.5 investigates how well coherent and random motions can be measured from the EFAR data sample.

3.5.1 Method comparison

As we have done above, we start comparing the performances of the 'classical approaches' (linear regressions and orthogonal fitting) and the ML algorithm, focusing on mock catalogues generated using parameters close to those derived for the EFAR data sample (see Paper VII and Case 0 of Table 1). We consider the 29 best clusters of the EFAR sample (see Paper VII), and we do not add peculiar velocities (i.e., the input peculiar velocity field is zero, $\delta_{\rm input}=0$). In each of the four methods considered we solve simultaneously for the coefficients a and b (see equation 21) and the vector δ_j. The shifts δ_j are determined by assuming that the mean of δ_j over the 29 clusters is zero, which fixes the value of the parameter c. Objects with $\sigma<100\,{\rm km\,s^{-1}}$, or with selection diameter D_W less than 12.6 kpc (i.e., $\log D_{W\rm cut}=1.1$), or with selection probabilities less than 0.1, are excluded from the fits. This procedure therefore mimics closely the 'fiducial' solution of Paper VII ('Case 1' of Table 4).

Fig. 6 shows the mean values and rms (over 99 simulations) of the FP coefficients a and b as determined using regressions on $\log R_e$, $\log\sigma$, $\langle SB_e\rangle$, orthogonal fitting and ML. As can be expected from the previous discussion, linear regressions and orthogonal fitting are inadequate to determine the coefficients of the FP. All five methods determine b quite accurately, with the $\langle SB_e\rangle$ and $\log R_e$ regressions giving the largest systematic

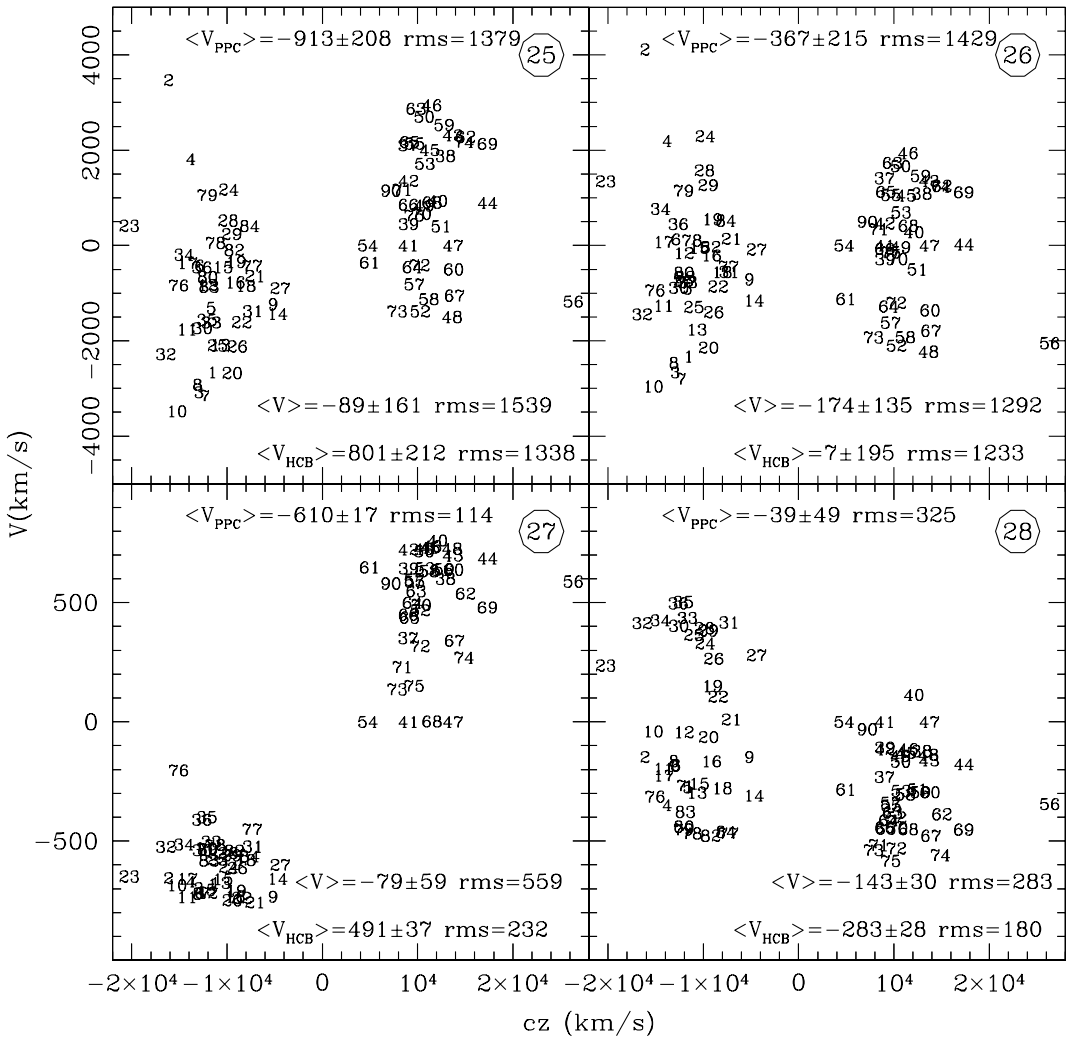

Figure 12. The input peculiar velocity fields of the simulations of Cases 25 to 28 of Table 1. Labels as in Fig. 11.

deviations ($\approx \pm 0.02$). Only the ML algorithm, however, is able to estimate a with a bias smaller than the expected statistical uncertainty. As expected from Appendix B, the $\log R_e$ and $\langle SB_e \rangle$ regressions and (less severely) the orthogonal fitting underestimate a, while the $\log \sigma$ regression overestimates it. As pointed out by Isobe et al. (1990), the $\log R_e$ regression gives the smallest rms. The ML algorithm determines a to 0.09 and b to 0.013 statistical accuracy.

Fig. 7 shows how well the five methods measure the input peculiar velocity shifts δ_j (all equal to zero) of the EFAR clusters. Similarly to the procedure described in Section 3.5.4 for the ML algorithm, the parameters a, b and c of the FP determined from the regressions on the subset of 29 best clusters for each separate simulation are used to compute the peculiar velocities of the remaining clusters.

Let us first focus on the clusters with $\log D^0_{W,j} - \delta_{W,j} < 1.18$. These are the clusters that statistically have at least one galaxy with $\log D_W \approx 1.1$ and selection probability larger than 0.1. In this case, the biasing influence of errors and selection effects is small for all the methods. The absolute values of the mean δ_j are typically smaller than 0.02 dex. The rms over the EFAR clusters of the mean δ_j over the 99 simulations is $\approx$0.008. The $\log R_e$ regression gives slightly poorer results. The statistical errors on the single cluster measurements are in any case larger, in the range 0.02–0.04 dex for the best-populated clusters, and up to 0.15 dex for the poorer populated clusters. The mean over the 99 simulations of the standard deviation (over the EFAR clusters) of the δ_j values differs for the various methods. The $\log R_e$ regression gives the smallest value (0.043 dex, or a typical 10.4 per cent accuracy on the determination of the distance of a single cluster), similar to the $\langle SB_e \rangle$ regression (0.045 dex, 10.9 per cent distance error). The ML algorithm and the orthogonal regression perform only slightly worse (0.049 dex, or 11.9 per cent distance error). The $\log \sigma$ regression gives the largest (0.065 dex, or 16 per cent distance error) random error.

The ML algorithm (and in order of increasingly importance the orthogonal, $\langle SB_e \rangle$ and $\log R_e$ regressions) derives δ_j biased to low values when $\log D^0_{W,j} - \delta_{W,j} \geq 1.18$. The clusters where this happens are so distant that their smallest galaxies in the EFAR sample have $\log D_W > 1.1$. Fig. 8 shows that these are clusters where we sample less than half of the galaxy distribution. From what was discussed in Section 3.2, we expect the ML algorithm to progressively fail in this regime. In Section 3.5.4 we correct for this residual bias due to the difference in the way the FP galaxy distribution is sampled in different clusters through simulations. In any case, the standard deviations (over the EFAR clusters) of the δ_j values do not change, remaining $\approx$4 times larger that the typical systematic errors.

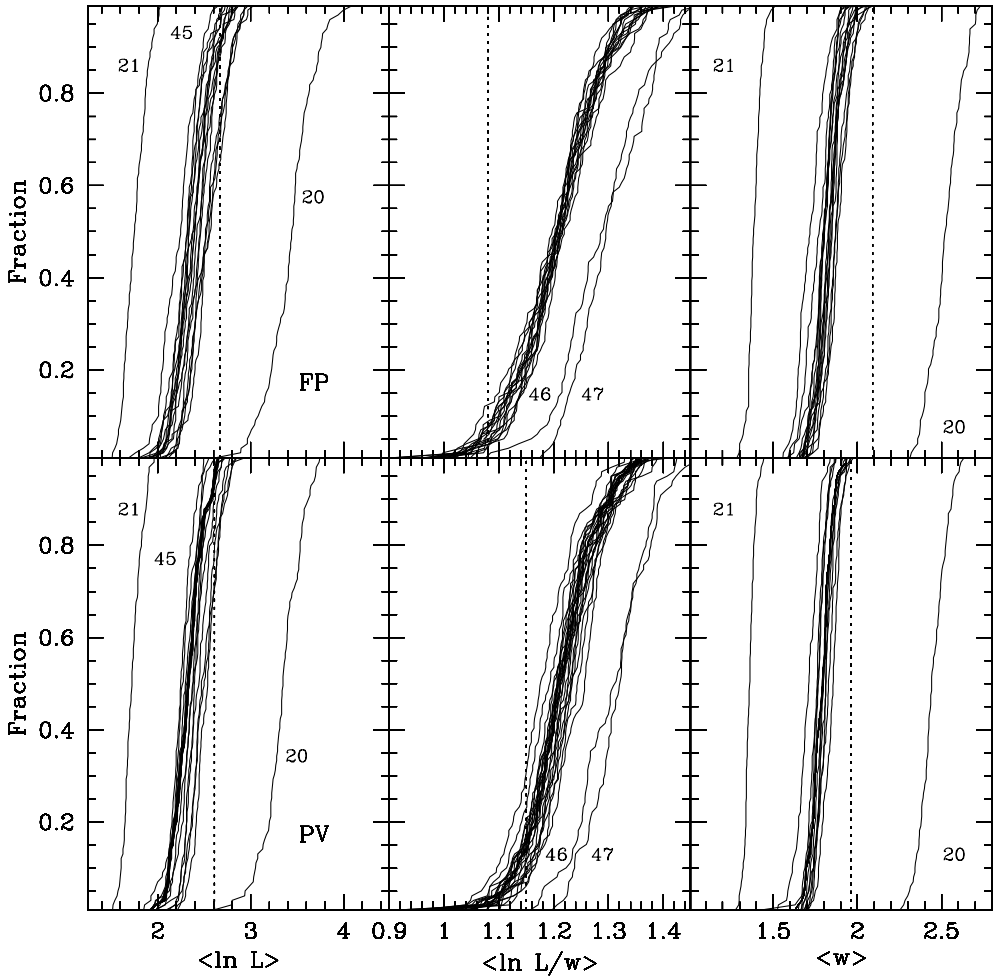

Figure 13. The cumulative distributions of the mean likelihoods (left), mean unweighted likelihoods (centre), mean selection weights (right). The top row refers to the galaxies of the clusters used in the determination of the FP parameters, and the bottom row to all galaxies of the clusters for which peculiar velocities are computed. The vertical dotted lines show the values of EFAR sample, as determined in Paper VII. The numbers identify the Cases discussed in the text.

Therefore we conclude that overall the ML method provides the best solution, keeping low the systematic and random errors on both the FP parameters and the δ_j values. In addition, it is more robust against outliers (since we can identify and remove the extreme low-likelihood objects; see Paper VII).

3.5.2 Variant cases and systematic errors

In this section we study the precision of the FP parameters derived using the ML algorithm, to justify the strategy adopted in Paper VII. Table 1 summarizes the tests performed, giving the mean values (over 99 simulations) of the number of clusters and galaxies (rounded to integer numbers) and the parameters of the FP derived for 28 cases. Table 2 lists the corresponding rms. Fig. 9 shows the results graphically.

Case 0 gives the parameters of the FP as derived in Paper VII for the standard fit. These are the input parameters used to generate the simulations considered here. Case 1 is the standard fit discussed above. Fig. 2 of Paper VII presents the histograms of 1000 simulations for this case. The mean values derived from the 99 simulations used here do not differ by more than 1.5 per cent from those derived from the 1000 simulations. As discussed in Paper VII, there are small residual biases in the fitted parameters: a is biased low by 6 per cent (i.e., since the mean value of a recovered from the simulations is smaller than the input value, we infer that the true value of a for the EFAR sample must be larger by $\approx$6 per cent than what was found in Case 0), b is biased low by 2 per cent; c is biased high by 4 per cent; $\overline{\log R_e}$, $\overline{\log \sigma}$ and $\overline{\langle SB_e \rangle}$ are all biased high, by 0.036 dex, 0.07 dex and 0.05 mag respectively; the scatter about the FP σ_1 is underestimated by 0.006 dex, or 1.4 per cent; the widths σ_2 and σ_3 of the galaxy distribution in the FP are biased by 0.049 (low) and 0.009 (high) dex respectively. These biases are all less than or comparable to the rms width of the distribution, so that although they are statistically significant (i.e., much greater than the standard error in the mean), they do not dominate the random error in the fitted parameters. Therefore in Paper VII we do not correct for these biases, since they are small and have negligible impact on the derived distances and peculiar velocities (see Section 3.5.4).

Case 2 is similar to Case 1: we do not add peculiar velocities, and we do not fit objects with $\sigma < 100\,\mathrm{km\,s^{-1}}$, or with selection diameter D_W less than 12.6 kpc (i.e., $\log D_{W\mathrm{cut}} = 1.1$), or with selection probabilities less than 0.1. However, in each simulation the list of fitted clusters is not fixed to the 29 clusters considered in Case 1; rather, it is restricted to the clusters that have six or more

Table 3. The mean residual selection bias $\langle \Delta\delta \rangle$ for Cases 1 (for 1000 and 99 simulations, with the rms error of the 99 simulations) and 20 to 28 of Table 1.

CAN	1 (1000)	1 (99)	dδ	20	21	22	23	24	25	26	27	28
1	−0.0182	0.0017	0.0048	−0.0119	−0.0028	−0.0014	−0.0081	0.0007	−0.0051	−0.0173	−0.0121	−0.0103
2	−0.0310	−0.0371	0.0053	−0.0484	−0.0299	−0.0320	−0.0435	−0.0348	−0.0350	−0.0376	−0.0436	−0.0352
3	−0.0204	−0.0166	0.0037	−0.0301	−0.0137	−0.0141	−0.0244	−0.0191	−0.0303	−0.0294	−0.0156	−0.0196
4	−0.0103	−0.0096	0.0061	−0.0092	−0.0110	−0.0110	−0.0088	−0.0091	−0.0136	−0.0155	−0.0174	−0.0153
5	−0.0142	−0.0153	0.0130	−0.0146	−0.0117	−0.0134	−0.0151	0.0179	0.0100	0.0362	0.0269	−0.0302
6	−0.0021	0.0036	0.0032	0.0081	0.0042	0.0042	0.0061	0.0021	−0.0074	−0.0051	−0.0037	−0.0051
7	−0.0218	−0.0174	0.0042	−0.0306	−0.0147	−0.0155	−0.0254	−0.0275	−0.0374	−0.0346	−0.0221	−0.0215
8	−0.0107	0.0034	0.0053	0.0035	0.0012	0.0012	0.0057	0.0012	−0.0002	−0.0051	−0.0109	−0.0031
9	+0.0069	0.0085	0.0099	0.0110	0.0112	0.0094	0.0120	−0.0207	−0.0026	−0.0018	−0.0028	0.0154
10	−0.0052	0.0018	0.0029	0.0053	0.0017	0.0007	0.0074	−0.0074	−0.0098	−0.0125	−0.0059	−0.0066
11	−0.0073	−0.0072	0.0052	−0.0021	−0.0074	−0.0068	−0.0062	−0.0092	−0.0050	−0.0070	−0.0065	−0.0028
12	−0.0024	0.0037	0.0036	0.0081	0.0028	0.0028	0.0077	−0.0014	−0.0044	−0.0122	0.0020	−0.0041
13	−0.0011	0.0061	0.0036	0.0187	0.0034	0.0057	0.0118	0.0069	−0.0044	−0.0054	0.0041	0.0001
14	+0.0033	−0.0015	0.0053	0.0047	−0.0021	−0.0015	0.0010	0.0041	0.0008	0.0056	0.0021	0.0037
15	+0.0007	0.0112	0.0056	0.0214	0.0117	0.0137	0.0126	−0.0015	0.0052	−0.0227	0.0020	−0.0083
16	+0.0019	0.0029	0.0031	0.0105	0.0027	0.0037	0.0053	−0.0001	−0.0094	−0.0085	−0.0017	0.0018
17	−0.0074	−0.0022	0.0033	0.0086	−0.0042	−0.0021	0.0023	−0.0096	−0.0172	−0.0140	−0.0126	−0.0069
18	−0.0001	−0.0032	0.0050	0.0027	−0.0029	−0.0028	−0.0005	0.0037	−0.0040	−0.0081	0.0013	−0.0001
19	+0.0009	0.0005	0.0090	0.0033	0.0030	0.0011	0.0040	−0.0142	0.0022	−0.0196	0.0118	−0.0033
20	−0.0005	0.0071	0.0026	0.0135	0.0053	0.0062	0.0120	0.0013	0.0001	−0.0084	0.0025	−0.0020
21	+0.0014	0.0043	0.0034	0.0109	0.0043	0.0050	0.0063	−0.0018	−0.0080	−0.0080	−0.0042	−0.0003
22	+0.0008	0.0036	0.0048	0.0089	0.0046	0.0047	0.0054	−0.0025	−0.0092	−0.0053	0.0016	−0.0112
23	−0.0077	0.0019	0.0030	−0.0056	0.0017	0.0000	0.0008	−0.0011	−0.0125	−0.0081	−0.0048	−0.0050
24	−0.0044	0.0015	0.0031	0.0004	0.0018	0.0011	0.0019	−0.0008	−0.0126	−0.0151	−0.0075	−0.0012
25	−0.0127	−0.0089	0.0033	−0.0195	−0.0067	−0.0077	−0.0169	−0.0136	−0.0208	−0.0139	−0.0152	−0.0218
26	−0.0073	−0.0072	0.0061	−0.0032	−0.0074	−0.0070	−0.0051	−0.0025	−0.0065	−0.0062	−0.0029	−0.0049
27	+0.0070	0.0133	0.0073	0.0179	0.0162	0.0142	0.0177	0.0179	0.0212	−0.0004	0.0269	0.0016
29	−0.0070	−0.0083	0.0066	−0.0081	−0.0073	−0.0069	−0.0092	−0.0129	−0.0015	−0.0149	−0.0042	−0.0017
30	−0.0135	−0.0174	0.0078	−0.0241	−0.0140	−0.0158	−0.0214	−0.0080	−0.0152	−0.0329	−0.0173	−0.0158
31	+0.0052	0.0096	0.0050	0.0116	0.0112	0.0104	0.0110	0.0130	0.0017	−0.0018	0.0040	0.0094
32	−0.0071	0.0018	0.0037	−0.0009	−0.0012	0.0002	−0.0008	−0.0140	−0.0045	−0.0127	−0.0087	−0.0065
33	−0.0114	−0.0049	0.0060	−0.0106	−0.0058	−0.0063	−0.0069	−0.0315	−0.0197	−0.0274	−0.0207	−0.0227
34	−0.0219	−0.0090	0.0039	−0.0272	−0.0040	−0.0071	−0.0215	−0.0206	−0.0269	−0.0238	−0.0196	−0.0214
35	−0.0059	0.0024	0.0022	−0.0029	0.0003	0.0005	−0.0006	−0.0008	−0.0137	−0.0136	−0.0030	−0.0073
36	−0.0146	−0.0084	0.0036	−0.0100	−0.0072	−0.0072	−0.0069	−0.0183	−0.0250	−0.0153	−0.0243	−0.0190
37	−0.0018	0.0049	0.0038	0.0111	0.0048	0.0050	0.0088	−0.0049	−0.0027	−0.0074	0.0061	−0.0023
38	−0.0054	0.0031	0.0050	0.0005	−0.0000	0.0008	0.0025	0.0014	−0.0122	−0.0039	0.0006	−0.0086
39	+0.0004	0.0102	0.0034	0.0196	0.0098	0.0113	0.0126	0.0077	−0.0034	−0.0083	0.0063	0.0016
40	−0.0054	−0.0002	0.0055	0.0011	−0.0009	−0.0011	0.0053	−0.0087	−0.0065	−0.0100	−0.0074	−0.0018
42	−0.0039	−0.0050	0.0041	0.0011	−0.0052	−0.0047	−0.0017	0.0038	−0.0045	−0.0082	−0.0030	0.0032
43	−0.0272	−0.0207	0.0051	−0.0473	−0.0115	−0.0147	−0.0377	−0.0283	−0.0292	−0.0345	−0.0252	−0.0379
44	−0.0438	−0.0341	0.0045	−0.0566	−0.0230	−0.0254	−0.0494	−0.0247	−0.0517	−0.0342	−0.0271	−0.0349
45	+0.0004	0.0106	0.0037	0.0163	0.0113	0.0119	0.0119	−0.0011	−0.0110	−0.0132	0.0017	−0.0077
46	−0.0089	−0.0014	0.0034	−0.0042	−0.0045	−0.0042	−0.0029	−0.0100	−0.0134	−0.0128	−0.0084	−0.0001
48	−0.0070	0.0003	0.0040	0.0001	−0.0025	−0.0023	0.0012	−0.0049	−0.0095	−0.0095	−0.0034	−0.0054
49	−0.0160	−0.0051	0.0047	−0.0110	−0.0012	−0.0025	−0.0075	−0.0061	−0.0120	−0.0073	0.0003	−0.0172
50	−0.0033	0.0071	0.0031	0.0077	0.0046	0.0048	0.0091	0.0017	−0.0079	−0.0069	0.0038	−0.0037
51	−0.0031	0.0076	0.0059	0.0102	0.0101	0.0086	0.0108	0.0081	−0.0028	−0.0062	−0.0030	−0.0072
52	−0.0067	0.0163	0.0069	0.0224	0.0180	0.0179	0.0187	−0.0040	0.0050	0.0011	0.0154	0.0008
53	−0.0357	−0.0231	0.0034	−0.0427	−0.0088	−0.0127	−0.0374	−0.0245	−0.0273	−0.0234	−0.0213	−0.0275
55	−0.0024	0.0014	0.0063	0.0055	0.0019	0.0018	0.0039	−0.0035	−0.0127	−0.0125	−0.0093	−0.0083
56	−0.0316	−0.0329	0.0072	−0.0449	−0.0327	−0.0338	−0.0410	−0.0312	−0.0502	−0.0414	−0.0346	−0.0475
57	−0.0032	0.0017	0.0068	0.0065	−0.0003	0.0006	0.0041	0.0011	−0.0039	−0.0050	0.0004	0.0011
58	−0.0165	−0.0075	0.0034	−0.0173	−0.0053	−0.0063	−0.0134	−0.0129	−0.0190	−0.0168	−0.0109	−0.0071
59	−0.0047	−0.0021	0.0031	−0.0011	−0.0025	−0.0039	0.0018	0.0013	−0.0107	−0.0089	−0.0072	−0.0012
60	−0.0251	−0.0155	0.0039	−0.0233	−0.0126	−0.0139	−0.0197	−0.0179	−0.0243	−0.0210	−0.0165	−0.0268
61	+0.0083	0.0062	0.0045	0.0099	0.0084	0.0074	0.0088	0.0013	−0.0016	0.0025	−0.0041	−0.0013
62	−0.0066	0.0040	0.0041	0.0057	0.0010	0.0027	0.0044	−0.0015	−0.0099	−0.0121	0.0019	−0.0053
63	+0.0010	−0.0077	0.0105	−0.0055	−0.0042	−0.0065	−0.0042	−0.0192	−0.0096	−0.0192	−0.0044	−0.0146
64	−0.0309	−0.0218	0.0064	−0.0266	−0.0150	−0.0182	−0.0221	−0.0304	−0.0425	−0.0439	−0.0306	−0.0383
65	−0.0015	0.0080	0.0028	0.0130	0.0085	0.0078	0.0126	0.0061	−0.0031	−0.0053	−0.0004	0.0006
66	+0.0001	0.0075	0.0027	0.0140	0.0065	0.0070	0.0118	0.0006	−0.0077	−0.0098	0.0040	0.0010
67	−0.0198	−0.0069	0.0044	−0.0185	−0.0067	−0.0075	−0.0150	−0.0238	−0.0233	−0.0207	−0.0212	−0.0230
68	−0.0060	−0.0009	0.0042	0.0063	0.0014	0.0014	0.0023	−0.0066	−0.0155	−0.0075	−0.0009	−0.0043
69	−0.0217	−0.0230	0.0099	−0.0358	−0.0114	−0.0142	−0.0262	−0.0181	−0.0215	−0.0439	−0.0231	−0.0250
70	−0.0026	0.0021	0.0032	0.0048	−0.0013	−0.0004	0.0050	0.0003	−0.0074	−0.0121	0.0056	0.0010
71	+0.0025	0.0146	0.0059	0.0216	0.0152	0.0158	0.0165	0.0017	−0.0037	0.0060	−0.0001	0.0044
72	−0.0096	−0.0086	0.0062	−0.0078	−0.0095	−0.0089	−0.0101	0.0043	−0.0160	−0.0084	−0.0071	0.0026
73	+0.0013	0.0105	0.0069	0.0144	0.0125	0.0121	0.0122	−0.0028	−0.0051	0.0122	0.0035	0.0001
74	−0.0329	−0.0354	0.0066	−0.0524	−0.0264	−0.0282	−0.0450	−0.0360	−0.0348	−0.0423	−0.0229	−0.0440
75	+0.0001	−0.0042	0.0050	0.0035	−0.0038	−0.0036	0.0002	0.0068	0.0026	−0.0105	−0.0040	−0.0009

Table 3 – *continued*

CAN	1 (1000)	1 (99)	dδ	20	21	22	23	24	25	26	27	28
76	−0.0306	−0.0262	0.0118	−0.0356	−0.0196	−0.0217	−0.0301	−0.0228	−0.0135	−0.0336	−0.0235	−0.0170
77	+0.0026	0.0138	0.0046	0.0160	0.0156	0.0150	0.0158	0.0038	0.0042	−0.0067	−0.0003	0.0078
78	−0.0075	−0.0079	0.0042	−0.0141	−0.0094	−0.0099	−0.0111	−0.0095	−0.0233	−0.0127	−0.0076	−0.0128
79	−0.0022	0.0017	0.0037	0.0071	0.0014	0.0022	0.0030	−0.0030	−0.0037	−0.0147	−0.0012	−0.0032
80	−0.0016	0.0022	0.0021	0.0078	0.0016	0.0022	0.0041	0.0008	−0.0046	−0.0049	−0.0026	0.0005
82	−0.0021	0.0022	0.0022	0.0087	−0.0005	0.0012	0.0058	−0.0010	−0.0051	−0.0047	0.0005	0.0017
83	−0.0024	0.0012	0.0029	0.0075	0.0012	0.0016	0.0039	−0.0013	−0.0049	−0.0151	0.0003	−0.0004
90	+0.0035	0.0071	0.0020	0.0117	0.0074	0.0068	0.0115	0.0037	−0.0002	−0.0062	0.0062	0.0038

galaxies. The number of fitted clusters fluctuates from 20 to 29 from simulation to simulation. The mean FP parameters do not show differences from Case 1.

Cases 3 to 8 examine fits performed on the subset of the clusters having 10 or more galaxies (Case 3) to clusters having three or more galaxies (Case 8). The mean FP parameters derived for Case 3 are the ones with the smallest biases. However, only 5–6 clusters for $\approx$ 70–80 galaxies are fitted. As a consequence, the statistical error on the parameters is nearly 2 times larger than for Case 1. On the contrary, Case 8 fits a larger number of galaxies and clusters than Case 1, and therefore gives slightly smaller ($\approx$20 per cent) statistical errors. However, the mean values of the FP parameters are biased more than for Case 1. In particular, the value of σ_1 is spuriously small, as offsetting the FP with spurious peculiar velocity suppresses the apparent scatter. We conclude that the list of clusters adopted in Paper VII is a reasonable compromise between the need of obtaining bias-free parameters and minimizing the statistical errors.

Cases 9 to 12 explore the effects of different $\log D_{W\rm cut}$. Low $\log D_{W\rm cut}$ give slightly smaller a coefficients; in addition, $\overline{\log R_{\rm e}}$ is too large, since essentially no normalization correction is applied. However, the statistical errors are smaller, because the sample size is maximized. In contrast, large $\log D_{W\rm cut}$ give larger a coefficients and too small $\overline{\log R_{\rm e}}$. In addition, the statistical errors are larger, because the sample size is reduced. We conclude that again Case 1 is the reasonable compromise both in terms of bias and statistical errors. This choice, however, forces us to apply additional corrections when deriving the peculiar velocities of the whole cluster sample (see Section 3.5.4).

Case 13 ignores selection probabilities altogether and applies a uniform weight to all galaxies, resulting in an effective overweighting of the larger galaxies. As a consequence, the mean values of $\overline{\log R_{\rm e}}$, $\overline{\log \sigma}$ and $\overline{\langle SB_{\rm e}\rangle}$ are biased to higher values. A similar effect, but of reduced amplitude, is observed for Case 14, where galaxies with selection probabilities lower than 0.2 are excluded. On the contrary, Case 15 includes essentially all galaxies in the fit, irrespective of their selection probabilities. The biases in the recovered parameters are reduced, but the statistical errors increase, because of the presence of a few (deviant) points with large weights. To conclude, weighting the data points with their inverse selection probability, and excluding galaxies with selection probabilities lower than 0.1, is a reasonable compromise that minimizes the biases and the statistical errors of the recovered parameters.

Case 16 shows that excluding the (few) galaxies with large errors on σ does not affect the results of the fits, both the mean and rms values of the parameters.

Case 17 excludes not only the galaxies rejected from the standard fit, but also galaxies with low likelihoods ($\ln \mathcal{L} < 0$); this results in a highly biased fit, with low a coefficient, an artificially lowered FP scatter, and a substantially narrower distribution in the FP. Case 18 replaces the individual error estimates for all measured quantities with uniform (average) errors. This has little effect on the derived parameters, but the statistical errors are larger.

Case 19 allows an extra degree of freedom by permitting the orientation of the major axis of the galaxy distribution within the FP to be fitted, rather than specified a priori. The vectors $\boldsymbol{v}_2$ and $\boldsymbol{v}_3$ of equation (27) now read

$$\boldsymbol{v}_2 = \hat{\boldsymbol{x}}_1 + v_{2,2}\hat{\boldsymbol{x}}_2 + v_{2,3}\hat{\boldsymbol{x}}_3, \tag{30}$$

$$\boldsymbol{v}_3 = v_{3,1}\hat{\boldsymbol{x}}_1 + v_{3,2}\hat{\boldsymbol{x}}_2 + \hat{\boldsymbol{x}}_3.$$

The only parameters affected are σ_2 and σ_3, which are biased high and low respectively. Fig. 10 shows the histogram of the recovered second and third components of vector $\boldsymbol{v}_2$, and the first and second components of vector $\boldsymbol{v}_3$. The input parameters (derived from the input a and b values and equation 27) are recovered with residual biases that are smaller than the statistical error. Therefore in Paper VII we use the simplifying approximation of equation (27).

Cases 20 to 23 explore the effects of errors on the parameters of the selection functions determined in Paper I. Case 20 considers mock catalogues where the selection probabilities used in the fitting procedure have been computed adding +0.1 dex to the true $\log D_W$. As a consequence, the selection weights are systematically higher than the true ones (see Fig. 13) and the mean number of selected galaxies (i.e., with selection probabilities larger than 0.1) is systematically smaller (see Table 1). In Case 21 we added −0.1 dex to the true $\log D_W$, getting selection weights systematically smaller than the true ones (see Fig. 13), and therefore a larger mean number of selected galaxies. Cases 22 and 23 use selection weights distorted by adding +0.1 dex (Case 22) and −0.1 dex (Case 23) to the selection probability widths δ_W. The largest systematic effects are observed for Case 20, where systematically smaller values of a, b and $\overline{\log \sigma}$, and systematically larger values of c and $\overline{\log R_{\rm e}}$ (because more small galaxies are excluded from the fit) are obtained. See Section 3.5.3 and Fig. 13 for a discussion of the effects on the distribution of likelihood probabilities.

Cases 24 to 28 refer to mock catalogues of the EFAR sample with peculiar velocity fields. Case 24 has a random peculiar velocity field (always the same for the performed 99 simulations) of 0.05 dex rms amplitude. We considered this particular field (see Fig. 11, where we plot the peculiar velocities of all clusters, the 29 in the FP sample plus the remaining ones) because its mean bulk motions of the clusters at positive (the Hercules–Corona–Borealis sample, HCB) and negative Galactic longitudes (the Pisces–Perseus–Cetus sample, PPC) are slightly non-zero and of opposite

Table 4. The mean residual selection bias $\langle \Delta\delta \rangle$ for Cases 29–38.

CAN	29 $+\mathrm{d}a$	30 $-\mathrm{d}a$	31 $+\mathrm{d}b$	32 $-\mathrm{d}b$	33 $+\mathrm{d}\overline{\log R_\mathrm{e}}$	34 $-\mathrm{d}\overline{\log R_\mathrm{e}}$	35 $+\mathrm{d}\overline{\langle SB_\mathrm{e}\rangle}$	36 $-\mathrm{d}\overline{\langle SB_\mathrm{e}\rangle}$	37 $+\mathrm{d}\overline{\log \sigma}$	38 $-\mathrm{d}\overline{\log \sigma}$
1	0.0059	−0.0027	0.0037	−0.0003	0.0267	−0.0233	−0.0176	0.0209	−0.0103	0.0125
2	−0.0320	−0.0422	−0.0341	−0.0401	−0.0121	−0.0621	−0.0564	−0.0177	−0.0510	−0.0225
3	−0.0108	−0.0225	−0.0149	−0.0183	0.0084	−0.0416	−0.0360	0.0028	−0.0327	−0.0001
4	−0.0052	−0.0139	−0.0077	−0.0113	0.0154	−0.0345	−0.0288	0.0097	−0.0221	0.0026
5	−0.0091	−0.0209	−0.0119	−0.0184	0.0108	−0.0413	−0.0354	0.0049	−0.0199	−0.0104
6	0.0062	0.0008	0.0047	0.0024	0.0285	−0.0214	−0.0159	0.0230	−0.0134	0.0206
7	−0.0118	−0.0232	−0.0151	−0.0197	0.0076	−0.0424	−0.0367	0.0020	−0.0328	−0.0014
8	0.0065	0.0002	0.0059	0.0010	0.0284	−0.0216	−0.0161	0.0229	−0.0108	0.0190
9	0.0095	0.0075	0.0077	0.0094	0.0343	−0.0173	−0.0114	0.0284	−0.0078	0.0228
10	0.0043	−0.0008	0.0031	0.0006	0.0268	−0.0232	−0.0176	0.0212	−0.0152	0.0197
11	−0.0044	−0.0102	−0.0054	−0.0092	0.0178	−0.0322	−0.0268	0.0123	−0.0223	0.0076
12	0.0063	0.0010	0.0045	0.0029	0.0287	−0.0213	−0.0157	0.0232	−0.0134	0.0212
13	0.0091	0.0030	0.0069	0.0053	0.0311	−0.0189	−0.0132	0.0255	−0.0079	0.0208
14	−0.0002	−0.0029	−0.0008	−0.0022	0.0235	−0.0265	−0.0208	0.0177	−0.0172	0.0146
15	0.0137	0.0086	0.0127	0.0097	0.0362	−0.0138	−0.0081	0.0305	−0.0016	0.0233
16	0.0048	0.0009	0.0032	0.0027	0.0279	−0.0221	−0.0164	0.0223	−0.0127	0.0188
17	0.0011	−0.0056	−0.0010	−0.0033	0.0228	−0.0272	−0.0214	0.0171	−0.0159	0.0110
18	−0.0012	−0.0053	−0.0028	−0.0036	0.0218	−0.0282	−0.0226	0.0162	−0.0192	0.0133
19	0.0019	−0.0009	0.0018	−0.0007	0.0274	−0.0264	−0.0203	0.0213	−0.0159	0.0191
20	0.0089	0.0053	0.0077	0.0066	0.0321	−0.0179	−0.0122	0.0264	−0.0098	0.0245
21	0.0057	0.0029	0.0049	0.0037	0.0293	−0.0207	−0.0151	0.0237	−0.0119	0.0204
22	0.0049	0.0022	0.0047	0.0025	0.0286	−0.0214	−0.0157	0.0229	−0.0128	0.0191
23	0.0047	−0.0008	0.0030	0.0009	0.0269	−0.0231	−0.0175	0.0214	−0.0151	0.0187
24	0.0042	−0.0012	0.0025	0.0006	0.0265	−0.0235	−0.0179	0.0210	−0.0155	0.0181
25	−0.0054	−0.0124	−0.0072	−0.0106	0.0161	−0.0339	−0.0283	0.0105	−0.0241	0.0064
26	−0.0035	−0.0109	−0.0061	−0.0083	0.0178	−0.0322	−0.0266	0.0122	−0.0221	0.0078
27	0.0149	0.0119	0.0130	0.0137	0.0383	−0.0117	−0.0060	0.0326	0.0005	0.0259
29	−0.0045	−0.0121	−0.0050	−0.0114	0.0168	−0.0333	−0.0275	0.0110	−0.0215	0.0063
30	−0.0133	−0.0215	−0.0155	−0.0193	0.0084	−0.0432	−0.0373	0.0025	−0.0338	0.0001
31	0.0109	0.0082	0.0097	0.0094	0.0348	−0.0157	−0.0103	0.0294	−0.0075	0.0275
32	0.0048	−0.0013	0.0030	0.0006	0.0268	−0.0232	−0.0176	0.0212	−0.0153	0.0190
33	−0.0021	−0.0076	−0.0032	−0.0066	0.0201	−0.0299	−0.0243	0.0146	−0.0200	0.0088
34	−0.0045	−0.0136	−0.0066	−0.0114	0.0160	−0.0340	−0.0283	0.0102	−0.0231	0.0036
35	0.0053	−0.0006	0.0034	0.0015	0.0274	−0.0226	−0.0170	0.0219	−0.0143	0.0189
36	−0.0045	−0.0123	−0.0067	−0.0101	0.0166	−0.0334	−0.0278	0.0110	−0.0247	0.0073
37	0.0070	0.0027	0.0060	0.0038	0.0299	−0.0201	−0.0145	0.0243	−0.0116	0.0213
38	0.0064	−0.0003	0.0046	0.0015	0.0281	−0.0219	−0.0162	0.0224	−0.0121	0.0184
39	0.0125	0.0078	0.0117	0.0088	0.0352	−0.0148	−0.0091	0.0296	−0.0043	0.0252
40	0.0022	−0.0026	−0.0003	−0.0001	0.0248	−0.0252	−0.0194	0.0191	−0.0163	0.0149
42	−0.0018	−0.0082	−0.0036	−0.0063	0.0200	−0.0300	−0.0245	0.0146	−0.0202	0.0101
43	−0.0151	−0.0264	−0.0178	−0.0237	0.0043	−0.0457	−0.0399	−0.0015	−0.0332	−0.0085
44	−0.0274	−0.0409	−0.0307	−0.0376	−0.0091	−0.0591	−0.0533	−0.0148	−0.0482	−0.0190
45	0.0131	0.0080	0.0118	0.0093	0.0356	−0.0144	−0.0089	0.0301	−0.0057	0.0262
46	0.0018	−0.0046	−0.0004	−0.0023	0.0236	−0.0263	−0.0206	0.0179	−0.0150	0.0130
48	0.0035	−0.0030	0.0017	−0.0011	0.0253	−0.0247	−0.0190	0.0195	−0.0134	0.0150
49	−0.0009	−0.0094	−0.0027	−0.0074	0.0199	−0.0301	−0.0244	0.0142	−0.0205	0.0119
50	0.0096	0.0045	0.0079	0.0062	0.0321	−0.0179	−0.0123	0.0264	−0.0085	0.0226
51	0.0109	0.0044	0.0085	0.0067	0.0329	−0.0176	−0.0120	0.0272	−0.0076	0.0222
52	0.0192	0.0135	0.0171	0.0155	0.0413	−0.0087	−0.0032	0.0359	0.0028	0.0293
53	−0.0173	−0.0290	−0.0209	−0.0254	0.0019	−0.0481	−0.0425	−0.0037	−0.0368	−0.0092
55	0.0026	0.0001	0.0032	−0.0005	0.0264	−0.0236	−0.0183	0.0210	−0.0155	0.0195
56	−0.0280	−0.0378	−0.0310	−0.0348	−0.0079	−0.0579	−0.0521	−0.0136	−0.0452	−0.0202
57	0.0048	−0.0015	0.0030	0.0003	0.0267	−0.0234	−0.0176	0.0210	−0.0121	0.0148
58	−0.0037	−0.0115	−0.0053	−0.0098	0.0175	−0.0325	−0.0269	0.0118	−0.0226	0.0079
59	0.0010	−0.0054	−0.0008	−0.0034	0.0229	−0.0271	−0.0214	0.0172	−0.0179	0.0136
60	−0.0107	−0.0204	−0.0124	−0.0185	0.0095	−0.0405	−0.0348	0.0038	−0.0306	0.0006
61	0.0075	0.0049	0.0064	0.0060	0.0312	−0.0188	−0.0133	0.0257	−0.0106	0.0215
62	0.0075	0.0004	0.0054	0.0026	0.0290	−0.0210	−0.0153	0.0233	−0.0107	0.0180
63	−0.0060	−0.0093	−0.0061	−0.0092	0.0186	−0.0340	−0.0281	0.0126	−0.0237	0.0094
64	−0.0173	−0.0264	−0.0194	−0.0242	0.0032	−0.0468	−0.0411	−0.0026	−0.0358	−0.0080
65	0.0109	0.0050	0.0088	0.0072	0.0330	−0.0170	−0.0113	0.0273	−0.0073	0.0241
66	0.0095	0.0054	0.0082	0.0068	0.0325	−0.0175	−0.0120	0.0270	−0.0086	0.0238
67	−0.0027	−0.0112	−0.0055	−0.0083	0.0181	−0.0319	−0.0263	0.0125	−0.0223	0.0081
68	0.0014	−0.0031	−0.0000	−0.0016	0.0241	−0.0258	−0.0202	0.0185	−0.0140	0.0119
69	−0.0152	−0.0310	−0.0204	−0.0257	0.0054	−0.0515	−0.0454	−0.0007	−0.0400	−0.0060
70	0.0042	−0.0002	0.0033	0.0009	0.0271	−0.0229	−0.0173	0.0214	−0.0130	0.0168
71	0.0170	0.0121	0.0157	0.0135	0.0399	−0.0106	−0.0051	0.0344	0.0001	0.0291
72	−0.0048	−0.0123	−0.0070	−0.0101	0.0164	−0.0336	−0.0280	0.0109	−0.0206	0.0054
73	0.0131	0.0078	0.0106	0.0104	0.0357	−0.0148	−0.0090	0.0299	−0.0043	0.0257
74	−0.0310	−0.0398	−0.0334	−0.0374	−0.0102	−0.0607	−0.0549	−0.0160	−0.0494	−0.0226

Table 4 – *continued*

CAN	29 +da	30 −da	31 +db	32 −db	33 +d$\overline{\log R_e}$	34 −d$\overline{\log R_e}$	35 +d$\overline{\langle SB_e\rangle}$	36 −d$\overline{\langle SB_e\rangle}$	37 +d$\overline{\log \sigma}$	38 −d$\overline{\log \sigma}$
75	−0.0017	−0.0068	−0.0034	−0.0051	0.0208	−0.0292	−0.0235	0.0150	−0.0174	0.0093
76	−0.0216	−0.0308	−0.0237	−0.0287	0.0004	−0.0528	−0.0467	−0.0057	−0.0420	−0.0102
77	0.0160	0.0116	0.0138	0.0138	0.0388	−0.0112	−0.0056	0.0333	−0.0034	0.0323
78	−0.0053	−0.0105	−0.0073	−0.0085	0.0171	−0.0329	−0.0272	0.0115	−0.0241	0.0084
79	0.0044	−0.0010	0.0020	0.0014	0.0267	−0.0233	−0.0177	0.0211	−0.0153	0.0191
80	0.0042	0.0001	0.0029	0.0016	0.0272	−0.0228	−0.0172	0.0216	−0.0149	0.0201
82	0.0043	−0.0000	0.0027	0.0017	0.0272	−0.0228	−0.0172	0.0216	−0.0144	0.0190
83	0.0032	−0.0009	0.0019	0.0006	0.0262	−0.0238	−0.0181	0.0205	−0.0148	0.0175
90	0.0087	0.0054	0.0074	0.0069	0.0321	−0.0179	−0.0122	0.0264	−0.0097	0.0237

sign, reminiscent of what we measured in Paper VII. In addition, its mean velocities projected along the Lauer & Postman and SMAC dipole directions (see Fig. 18 for the peculiar velocity field of all clusters) are also similar to what seen in Paper VII. Case 25 has a random field (always the same for the performed 99 simulations) of the same rms amplitude as Case 24 (0.05 dex) plus the bulk flow motions determined by Lauer & Postman (1994, hereafter LP; see Fig. 12 for the peculiar velocity field of all clusters). LP measured the bulk motion of the Abell clusters with $cz < 15\,000\,\mathrm{km\,s^{-1}}$ with respect to the cosmic microwave background to be $764\,\mathrm{km\,s^{-1}}$ in the direction of $l = 341°$, $b = 44°$ (reanalysis by Colless 1995), using the $L - \alpha$ relation for the brightest cluster galaxies. The resulting peculiar velocity field has a prominent asymmetry of the mean bulk motions of the HCB and PPC clusters (see Fig. 12), which gives an apparently larger dipole motion in the LP direction (see Fig. 18). Case 26 adds on top of a random field of 0.05 rms amplitude (always the same for the performed 99 simulations) the bulk motion determined by Hudson et al. (1999, hereafter SMAC). SMAC determined the motions of the Abell clusters with $cz < 12\,000\,\mathrm{km\,s^{-1}}$ using the FP, finding $V_{\rm bulk} = 630\,\mathrm{km\,s^{-1}}$ towards $l = 260°$, $b = -1$. The resulting peculiar velocity field has small mean bulk motions of the HCB and PPC clusters (see Fig. 12 for the peculiar velocity field of all clusters), and an approximately zero dipole motion in the SMAC direction (see Fig. 18). Case 27 has a pure LP bulk motion without a random component. Case 28 has a pure SMAC bulk motion without a random component. In all five cases the FP parameters are recovered without additional biases with respect to Case 1. The statistical errors are slightly larger, especially for the $\overline{\log R_e}$ parameter. The mean number of galaxies varies slightly, as galaxies near the selection cut might get included or not in the sample accordingly to the positive or negative peculiar velocity of the clusters they belong to (see Section 3.1). We conclude that the ML algorithm recovers the FP parameters correctly also when peculiar velocity fields are present.

The last three sets of simulations (Cases 45, 46 and 47) refer to input distributions uniform in the FP parameters, in the errors, or both (see Section 3.1), with zero peculiar velocity fields. Inspection of Tables 1 and 2 and Fig. 9 shows that also in these cases the input parameters are recovered with small biases. The largest effects are seen for σ_2, where the ML Gaussian algorithm overestimates the effects of the uniform error distribution, biasing σ_2 low. The rms values are similar to the ones derived for the previous cases: da, db, dc are marginally larger, dσ_2 marginally smaller.

Summarizing, with only a few exceptions (noted above), the systematic differences in the fits derived for different cases are comparable to the random errors in the determination of the parameters for the standard case. Therefore the uncertainties in our best-fitting FP parameters are dominated by the random errors and not by systematic effects from the fitting method. In addition, the systematic effects explored in the simulations (Tables 1 and 2) reproduce, at least qualitatively, the trends observed in the fits to the actual EFAR data (table 4 of Paper VII).

3.5.3 The likelihood distribution

We now investigate whether the assumption of a Gaussian distribution of galaxies in the FP space is compatible with the EFAR data sample. Fig. 13 (left-hand panels) shows the cumulative distributions of the mean (i.e., normalized to the number of galaxies fitted) likelihoods of the simulations of Cases 1 to 8, 18 to 28, and 45 to 47 (top row, only galaxies of clusters used to determine the FP parameters) and Cases 1 and 20 to 47 (bottom row, all galaxies of the clusters for which peculiar velocities have been computed). Note that Cases 29 to 44, not listed in Tables 1 and 2, are discussed in detail in Section 3.5.4. They are perturbed versions of Case 1.

Except for Cases 20 and 21, all simulations (including the uniform distribution cases 45, 46 and 47) give similar cumulative distributions of the mean likelihoods. Depending on the exact case, a mean likelihood equal to or larger than that of the EFAR sample is observed in up to 30 per cent of the simulations. Case 45 (a uniform distribution of the FP parameters and Gaussian errors) gives only slightly smaller mean likelihoods. Case 20 gives systematically higher mean likelihoods, and Case 21 systematically lower, than that of the EFAR sample. Inspection of the central and left-hand panels plots of Fig. 13 clarifies that the cumulative distribution of the mean unweighted likelihoods are similar for all the simulations with Gaussian error distributions, predicting that values larger than that of the EFAR sample are observed in 70 to 95 per cent of the cases. The Cases 46 and 47, where the error distributions are uniform, produce systematically 20–30 per cent larger values, because the ML Gaussian algorithm is overstressing the role of errors. As noticed before (see Fig. 5), the mean selection weights of all simulations, except Case 20, are smaller than that of the EFAR sample.

Therefore we conclude that the Gaussian modelling is a reasonable description of the distribution of the EFAR galaxies in the ($\log R_e$, $\log \sigma$, $\langle SB_e\rangle$) space and of the error distribution. The EFAR data set does not allow to discriminate between a Gaussian and a uniform distribution of the FP parameters. Error distributions with tails slightly stronger than Gaussians are hinted. Values of $\log D_W^0$ slightly larger (by $\approx$0.04 dex) than that measured in

Table 5. The mean residual selection bias $\langle\delta\rangle$ for Cases 39–47.

CAN	39 $+d\sigma_1$	40 $-d\sigma_1$	41 $+d\sigma_2$	42 $-d\sigma_2$	43 $+d\sigma_3$	44 $-d\sigma_3$	45 UG	46 GU	47 UU
1	0.0021	0.0012	0.0018	0.0015	0.0057	−0.0031	−0.0066	−0.0131	−0.0072
2	−0.0377	−0.0365	−0.0368	−0.0373	−0.0334	−0.0416	−0.0250	−0.0355	−0.0236
3	−0.0172	−0.0160	−0.0165	−0.0167	−0.0137	−0.0203	−0.0077	−0.0115	−0.0185
4	−0.0093	−0.0098	−0.0095	−0.0096	−0.0059	−0.0139	−0.0071	−0.0050	−0.0022
5	−0.0146	−0.0159	−0.0152	−0.0154	−0.0075	−0.0227	0.0077	−0.0026	−0.0002
6	0.0042	0.0030	0.0036	0.0035	0.0047	0.0020	0.0041	−0.0027	0.0063
7	−0.0179	−0.0169	−0.0173	−0.0175	−0.0140	−0.0217	−0.0156	−0.0138	−0.0203
8	0.0040	0.0029	0.0036	0.0032	0.0058	0.0004	−0.0003	−0.0037	−0.0026
9	0.0103	0.0069	0.0084	0.0086	0.0086	0.0083	0.0115	−0.0003	0.0129
10	0.0024	0.0013	0.0019	0.0017	0.0029	0.0003	0.0042	0.0040	0.0068
11	−0.0066	−0.0079	−0.0071	−0.0074	−0.0054	−0.0097	−0.0111	−0.0007	0.0035
12	0.0044	0.0031	0.0037	0.0037	0.0048	0.0022	0.0069	0.0063	0.0080
13	0.0070	0.0053	0.0061	0.0061	0.0087	0.0029	0.0045	0.0099	0.0108
14	−0.0003	−0.0027	−0.0015	−0.0016	−0.0008	−0.0026	0.0086	0.0081	0.0052
15	0.0123	0.0101	0.0113	0.0110	0.0135	0.0083	0.0062	0.0074	0.0042
16	0.0039	0.0021	0.0029	0.0029	0.0042	0.0013	0.0029	0.0031	0.0069
17	−0.0016	−0.0027	−0.0022	−0.0022	0.0005	−0.0055	−0.0017	−0.0065	0.0023
18	−0.0023	−0.0040	−0.0032	−0.0032	−0.0021	−0.0047	0.0038	0.0082	0.0110
19	0.0019	−0.0007	0.0006	0.0004	0.0011	−0.0003	0.0232	0.0050	0.0141
20	0.0081	0.0062	0.0071	0.0071	0.0080	0.0058	0.0037	0.0052	0.0046
21	0.0056	0.0032	0.0043	0.0043	0.0050	0.0033	0.0126	0.0096	0.0070
22	0.0047	0.0025	0.0037	0.0035	0.0042	0.0027	0.0022	0.0066	0.0136
23	0.0025	0.0015	0.0021	0.0018	0.0031	0.0003	0.0017	0.0025	−0.0033
24	0.0021	0.0011	0.0016	0.0015	0.0027	−0.0001	−0.0026	0.0035	0.0009
25	−0.0086	−0.0091	−0.0087	−0.0090	−0.0067	−0.0117	−0.0101	−0.0099	−0.0046
26	−0.0068	−0.0076	−0.0072	−0.0072	−0.0051	−0.0099	0.0012	0.0155	−0.0006
27	0.0149	0.0119	0.0132	0.0134	0.0139	0.0125	0.0192	0.0217	0.0290
29	−0.0080	−0.0085	−0.0080	−0.0086	−0.0050	−0.0121	0.0031	−0.0047	−0.0078
30	−0.0173	−0.0175	−0.0173	−0.0175	−0.0151	−0.0204	−0.0145	−0.0050	0.0020
31	0.0109	0.0084	0.0095	0.0096	0.0101	0.0088	0.0107	0.0030	0.0147
32	0.0023	0.0014	0.0019	0.0017	0.0030	0.0002	−0.0029	0.0001	0.0058
33	−0.0045	−0.0051	−0.0048	−0.0050	−0.0032	−0.0070	−0.0051	0.0007	0.0016
34	−0.0091	−0.0089	−0.0088	−0.0092	−0.0054	−0.0134	−0.0191	−0.0027	−0.0088
35	0.0029	0.0020	0.0025	0.0024	0.0038	0.0006	−0.0011	−0.0023	0.0036
36	−0.0083	−0.0085	−0.0083	−0.0085	−0.0066	−0.0107	−0.0077	−0.0039	−0.0033
37	0.0058	0.0041	0.0049	0.0048	0.0059	0.0036	0.0043	−0.0018	0.0006
38	0.0037	0.0025	0.0032	0.0029	0.0051	0.0004	0.0052	0.0066	−0.0045
39	0.0112	0.0093	0.0103	0.0101	0.0119	0.0081	0.0139	0.0021	0.0042
40	0.0006	−0.0009	−0.0003	−0.0001	0.0013	−0.0022	0.0021	−0.0023	0.0024
42	−0.0044	−0.0055	−0.0049	−0.0050	−0.0031	−0.0073	0.0070	0.0053	−0.0007
43	−0.0212	−0.0202	−0.0205	−0.0210	−0.0157	−0.0266	−0.0248	−0.0258	−0.0338
44	−0.0353	−0.0329	−0.0338	−0.0344	−0.0290	−0.0402	−0.0308	−0.0333	−0.0279
45	0.0114	0.0098	0.0106	0.0105	0.0117	0.0090	0.0022	0.0018	0.0116
46	−0.0007	−0.0020	−0.0013	−0.0014	0.0012	−0.0045	−0.0037	0.0031	−0.0038
48	0.0012	−0.0006	0.0003	0.0002	0.0029	−0.0030	−0.0013	−0.0017	−0.0052
49	−0.0051	−0.0051	−0.0049	−0.0053	−0.0025	−0.0084	−0.0077	−0.0076	−0.0032
50	0.0079	0.0063	0.0071	0.0070	0.0087	0.0049	0.0078	0.0026	0.0032
51	0.0083	0.0070	0.0077	0.0076	0.0094	0.0053	0.0087	0.0089	0.0002
52	0.0175	0.0153	0.0163	0.0163	0.0181	0.0140	−0.0004	0.0160	0.0217
53	−0.0240	−0.0223	−0.0230	−0.0232	−0.0187	−0.0284	−0.0216	−0.0233	−0.0286
55	0.0025	0.0004	0.0014	0.0013	0.0020	0.0005	0.0045	0.0070	0.0057
56	−0.0332	−0.0325	−0.0328	−0.0329	−0.0279	−0.0387	−0.0435	−0.0214	−0.0294
57	0.0025	0.0009	0.0017	0.0016	0.0042	−0.0015	0.0029	0.0029	0.0087
58	−0.0075	−0.0076	−0.0074	−0.0078	−0.0050	−0.0108	−0.0091	−0.0129	−0.0035
59	−0.0017	−0.0025	−0.0021	−0.0022	−0.0002	−0.0046	0.0012	−0.0034	−0.0018
60	−0.0158	−0.0153	−0.0153	−0.0158	−0.0124	−0.0194	−0.0189	−0.0160	−0.0153
61	0.0074	0.0051	0.0062	0.0062	0.0068	0.0054	0.0186	0.0001	0.0102
62	0.0046	0.0035	0.0041	0.0039	0.0066	0.0008	−0.0008	0.0053	0.0061
63	−0.0064	−0.0089	−0.0076	−0.0078	−0.0071	−0.0085	−0.0132	0.0112	−0.0030
64	−0.0218	−0.0219	−0.0216	−0.0221	−0.0185	−0.0260	−0.0264	−0.0251	−0.0169
65	0.0087	0.0074	0.0080	0.0079	0.0097	0.0058	0.0082	0.0020	0.0035
66	0.0084	0.0067	0.0076	0.0074	0.0086	0.0060	0.0045	0.0064	0.0052
67	−0.0067	−0.0070	−0.0068	−0.0070	−0.0042	−0.0103	−0.0216	−0.0057	−0.0036
68	0.0000	−0.0016	−0.0008	−0.0009	0.0008	−0.0030	0.0025	0.0037	0.0033
69	−0.0239	−0.0223	−0.0229	−0.0231	−0.0182	−0.0291	0.0003	−0.0312	−0.0166
70	0.0029	0.0013	0.0021	0.0020	0.0037	−0.0000	−0.0012	0.0113	0.0023
71	0.0156	0.0137	0.0147	0.0145	0.0161	0.0126	0.0194	0.0039	0.0136
72	−0.0080	−0.0091	−0.0085	−0.0086	−0.0052	−0.0126	−0.0001	−0.0072	−0.0075
73	0.0116	0.0095	0.0104	0.0105	0.0120	0.0085	0.0099	0.0021	0.0008
74	−0.0356	−0.0352	−0.0353	−0.0356	−0.0321	−0.0395	−0.0398	−0.0257	−0.0391

Table 5 – *continued*

CAN	39 $+d\sigma_1$	40 $-d\sigma_1$	41 $+d\sigma_2$	42 $-d\sigma_2$	43 $+d\sigma_3$	44 $-d\sigma_3$	45 UG	46 GU	47 UU
75	−0.0035	−0.0049	−0.0042	−0.0042	−0.0022	−0.0067	0.0035	0.0057	0.0031
76	−0.0259	−0.0265	−0.0260	−0.0264	−0.0238	−0.0293	−0.0233	−0.0155	−0.0208
77	0.0148	0.0129	0.0138	0.0138	0.0147	0.0126	0.0136	0.0057	0.0128
78	−0.0073	−0.0084	−0.0078	−0.0079	−0.0065	−0.0097	−0.0041	0.0037	0.0077
79	0.0023	0.0012	0.0017	0.0017	0.0029	0.0001	0.0079	0.0045	0.0029
80	0.0030	0.0015	0.0022	0.0022	0.0031	0.0010	0.0054	0.0052	0.0055
82	0.0030	0.0015	0.0022	0.0022	0.0033	0.0006	0.0080	0.0039	0.0030
83	0.0021	0.0003	0.0012	0.0012	0.0024	−0.0005	0.0031	0.0082	0.0045
90	0.0083	0.0060	0.0071	0.0071	0.0079	0.0059	0.0069	0.0031	0.0088

Paper I are needed to match the mean selection weight of the EFAR sample.

3.5.4 *Peculiar velocities and bias corrections*

Once the parameters of the best-fitting Gaussian distribution are determined using a subset of clusters (hereafter the FP clusters), the ML algorithm is used with these parameters fixed, to compute the peculiar velocities of the remaining clusters. Tables 3, 4 and 5 give the average residuals (over 99 simulations) from the input peculiar velocities $\langle \Delta\delta \rangle = \langle \delta - \delta_{\rm input} \rangle$ for a number of cases. Table 3 considers Cases 1 and 20 to 28 of Table 1, listing also the values of $\langle \Delta\delta \rangle$ given in table 7 of Paper VII, based on 1000 simulations of Case 1, and the statistical precision reached for Case 1 and 99 simulations. Tables 4 and 5 give the results for 19 additional Cases, from 29 to 47. The 16 Cases from 29 to 44 are obtained by perturbing one of the FP parameters by $\pm 1\sigma$, keeping the others fixed to the best solution value. Cases 29 and 30 perturb the *a*

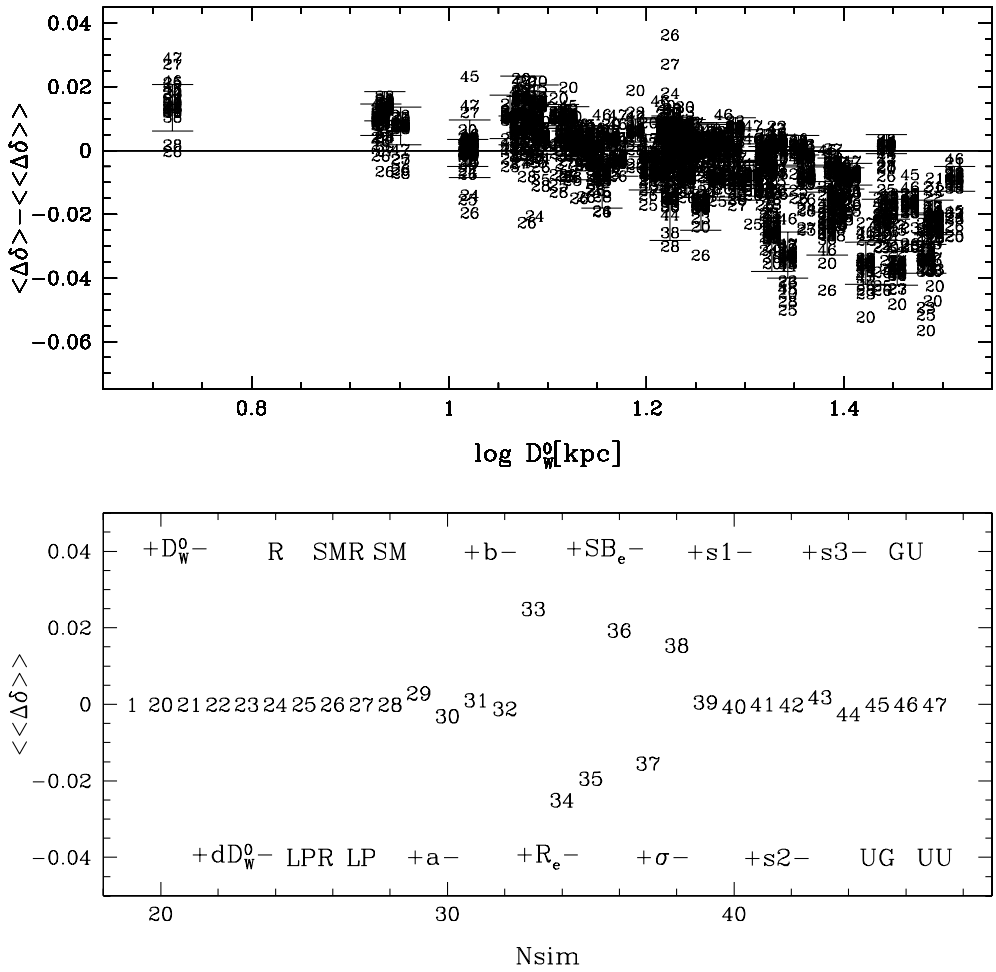

Figure 14. The residuals selection bias determined from 99 simulations and Cases 1 and 20 to 28 of Tables 1 and 3, and Cases 29 to 44 of Tables 4 and 5. The top panel shows the residuals $\langle \Delta\delta \rangle = \langle \delta - \delta_{\rm input} \rangle$ from the input peculiar velocity field $\delta_{\rm input}$ ($\delta_{\rm input} = 0$ for Cases 1, 20 to 23, and 29 to 44; see text, Table 1 and Figs 11 and 12 for Cases 23 to 28), with the average residual over the FP clusters subtracted off, as a function of $\log D_W^0$. Each Case is identified by its number (see Tables 1, 4 and 5). The error bars show the statistical precision reached for Case 1 with 99 simulations. The bottom panel shows the average residual measured for the FP clusters as a function of the Case number. The labels provide an additional mnemonic identifier.

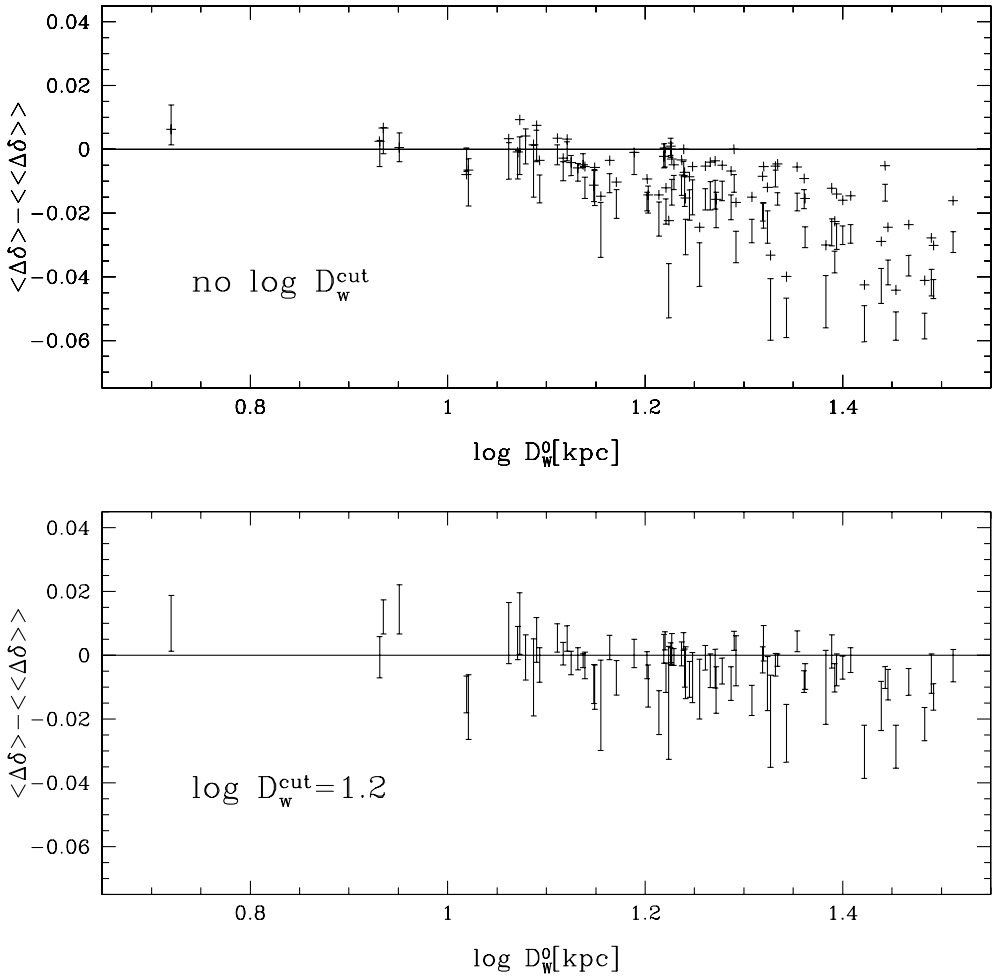

Figure 15. The residual selection bias $\langle\Delta\delta\rangle - \langle\!\langle\Delta\delta\rangle\!\rangle$ determined for Case 9 (no $\log D_{W\rm cut}$ applied, top) and Case 12 ($\log D_{W\rm cut} = 1.2$, bottom), as a function of $\log D_W^0$. The error bars show the statistical precision reached with 99 simulations. The crosses show the mean values for Case 1.

coefficient, 31 and 32 b, 33 and 34 $\overline{\log R_{\rm e}}$, 35 and 36 $\overline{\log\sigma}$, 37 and 38 $\overline{\langle SB_{\rm e}\rangle}$, 39 and 40 σ_1, 41 and 42 σ_2, 43 and 44 σ_3, respectively. Cases 45, 46 and 47 refer to the simulations with uniform distributions in the FP parameters, the errors, or both.

Fig. 14 shows $\langle\Delta\delta\rangle - \langle\!\langle\Delta\delta\rangle\!\rangle$ as a function of $\log D_W^0$. Here $\langle\!\langle\Delta\delta\rangle\!\rangle$ is the average residual over the FP clusters. It is zero by construction for Cases 1, 20 to 28, and 45 to 47. The general trend of increasingly negative residuals at large values of $\log D_W^0$ is easily explained. The clusters at higher redshifts (large $\log D_W^0$) lack small galaxies and therefore have mean values of $\log R_{\rm e}$ larger than $\overline{\log R_{\rm e}}$, or $\delta = \overline{\log R_{\rm e}} - \log R_{\rm e}$ progressively more negative.

Once the zero-point offset (given by the residual $\langle\Delta\delta\rangle$ averaged over the FP clusters) is subtracted off, the simulations 29 to 44 give residuals compatible with Case 1 within the statistical errors. Therefore the residual bias corrections are robust against small errors in the FP solution. The largest variations of the zero-point are observed when the values of $\overline{\log R_{\rm e}}$, $\overline{\log\sigma}$ and $\overline{\langle SB_{\rm e}\rangle}$ are perturbed. As expected, one finds $\langle\!\langle\Delta\delta\rangle\!\rangle \approx \pm 0.025 = \pm {\rm d}\overline{\log R_{\rm e}}$, when $\overline{\log R_{\rm e}}$ is perturbed, $\langle\!\langle\Delta\delta\rangle\!\rangle \approx \pm 0.02 = \mp a\,{\rm d}\overline{\log\sigma}$, when $\overline{\log\sigma}$ is perturbed, and $\langle\!\langle\Delta\delta\rangle\!\rangle \approx \pm 0.02 = \mp b\,{\rm d}\overline{\langle SB_{\rm e}\rangle}$ when $\overline{\langle SB_{\rm e}\rangle}$ is perturbed. Errors in $\log D_W^0$ affect the selection weighting scheme, and therefore the determination of $\langle\Delta\delta\rangle$ for the clusters (at higher redshifts) that have the largest $\log D_W^0$. In some cases the errors in $\langle\Delta\delta\rangle$ are larger than the statistical precision of Case 1. Positive errors ($+D_W^0$, Case 20) produce too negative $\langle\Delta\delta\rangle$, since more small galaxies than with the correct values of $\log D_W^0$ are excluded from the fits. The contrary happens for negative errors ($-D_W^0$, Case 21). Errors in δ_W affect also $\langle\Delta\delta\rangle$, especially at higher redshifts. In this case negative errors ($-{\rm d}D_W^0$, Case 23) produce too negative $\langle\Delta\delta\rangle$, because a sharper (i.e., a smaller δ_W) selection function eliminates more small galaxies. Positive errors (${\rm d}D_W^0$, Case 22) produce the reverse.

The presence of a peculiar velocity field (Cases 24 to 28) can also affect $\langle\Delta\delta\rangle$, because redshift distances are used to convert the measured selection cuts from arcsec to kpc. In particular, clusters sampled by a small number of galaxies are prone to small-number statistics fluctuations, as galaxies near the selection cut-off might not be always included in the simulation catalogues.

Uniform distributions of the FP parameters, of the errors, or both do not affect $\langle\Delta\delta\rangle$ systematically, within the statistical errors.

Finally, Fig. 15 illustrates the effect of the $\log D_{W\rm cut}$ value on the required peculiar velocities. When no $\log D_{W\rm cut}$ is applied (Case 9), the residual biases at high $\log D_W^0$ are larger than when $\log D_{W\rm cut}$ is equal to 1.1 (Case 1). The biases are reduced if a larger $\log D_{W\rm cut}$ (1.2, Case 12) is chosen, but the statistical errors increase. In addition, as discussed in Section 3.5.2, this choice gives larger systematic and statistical errors for the FP parameters.

We conclude that the peculiar velocity biases are much

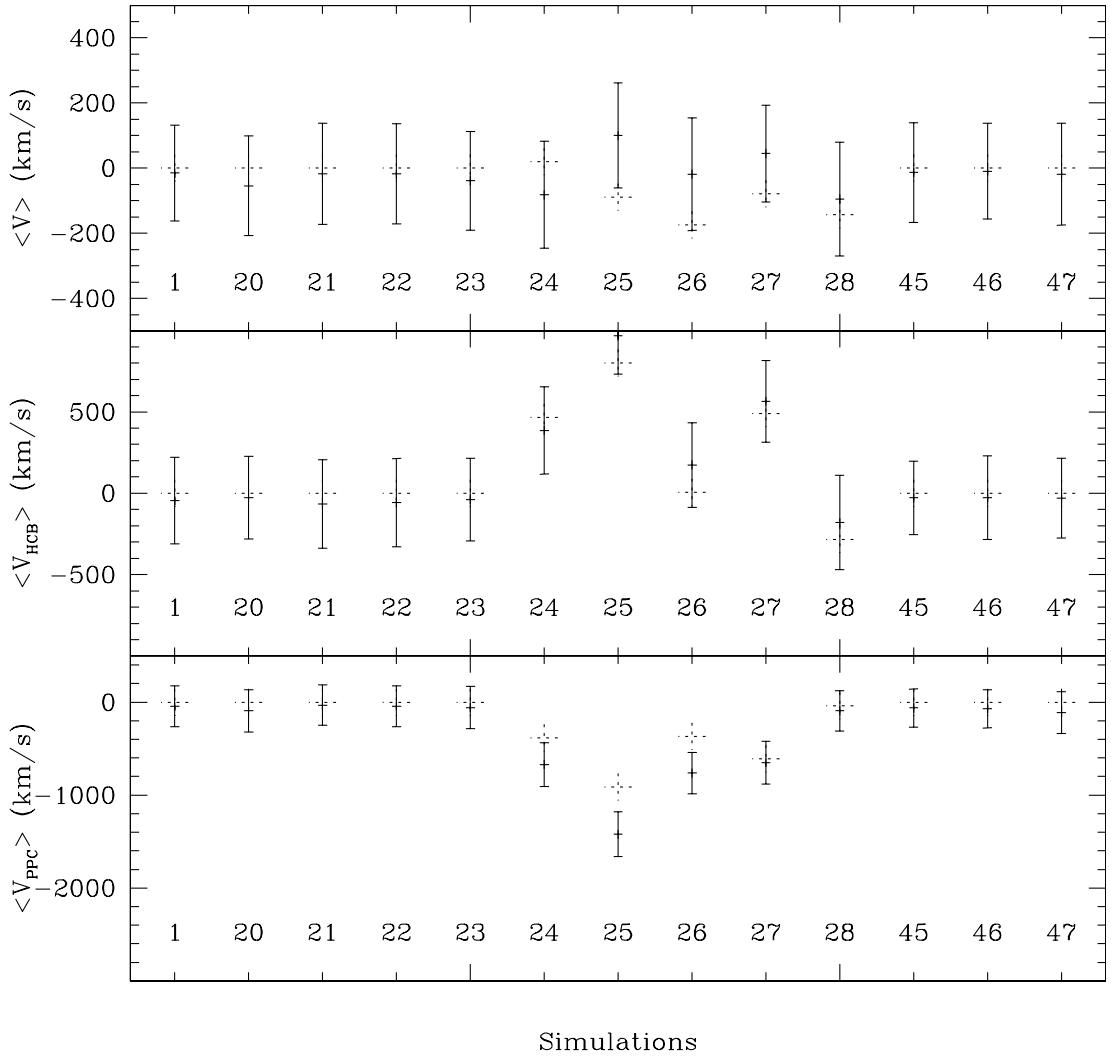

Figure 16. The simulations of the mean peculiar velocities $\langle V \rangle$ (mean velocity of the sample of 50 clusters defined in Paper VII, top panel), $\langle V_{\rm HCB} \rangle$ (mean velocity of the clusters with positive Galactic longitude, the HCB sample, middle panel) and $\langle V_{\rm PPC} \rangle$ (mean velocity of the clusters with negative Galactic longitude, the PPC sample, bottom panel). The points show the mean values (over 99 simulations) and their rms for Cases 1, 20 to 28, and 45 to 47 of Table 1. The dotted bars show the input values.

smaller than the random errors in the peculiar velocities. The uncertainties in the peculiar velocity bias corrections as computed from the 1000 simulations of Case 1 used in Paper VII do not increase the random errors in the peculiar velocities. However, residual systematic effects at the level of 0.01 dex might still be present, especially for the clusters at higher redshifts, due to the uncertainties in the determination of the selection function.

3.5.5 The estimation of the mean motions

Given the large mean distance of the EFAR clusters, and the precision of the FP distance estimator (20 per cent for the single galaxy; see Paper VII), the present data set does not allow the determination of the peculiar motions of single clusters. Nevertheless, the mean motions of the EFAR clusters can be constrained. In the following we investigate this point using the subsample of clusters identified in Paper VII for the study of the bulk motions. To this belong the 50 EFAR clusters with three or more galaxies (hereafter peculiar velocity, PV, clusters), redshifts less than $15\,000\,{\rm km\,s^{-1}}$, and peculiar velocity errors less than $1800\,{\rm km\,s^{-1}}$. We compute the average mean velocities without applying the bias corrections investigated in Section 3.5.4 (although this is done in Paper VII), to stress that our results are not affected much by these residual systematic uncertainties, and that random errors dominate the noise.

We begin by examining the mean peculiar velocities $\langle V \rangle$, $\langle V_{\rm HCB} \rangle$ and $\langle V_{\rm PPC} \rangle$ of the sample. These are the mean over the PV clusters, over the PV clusters with positive Galactic longitude (the HCB sample), and over the ones with negative Galactic longitude (the PPC sample). Fig. 16 shows that these average quantities are recovered with statistical errors of about $200\,{\rm km\,s^{-1}}$. These errors are generally larger than the systematic differences from the input values. In particular, errors on the selection function parameters do not affect the result much (Cases 20 to 23) and uniform distributions of the FP parameters, of the errors, or both do not change this conclusion (Cases 45 to 47). The largest systematic difference is observed for Cases 24 to 26 and $V_{\rm PPC}$, where the input values are ill-defined, since the rms of the cluster peculiar velocities is large (see Figs 11 and 12).

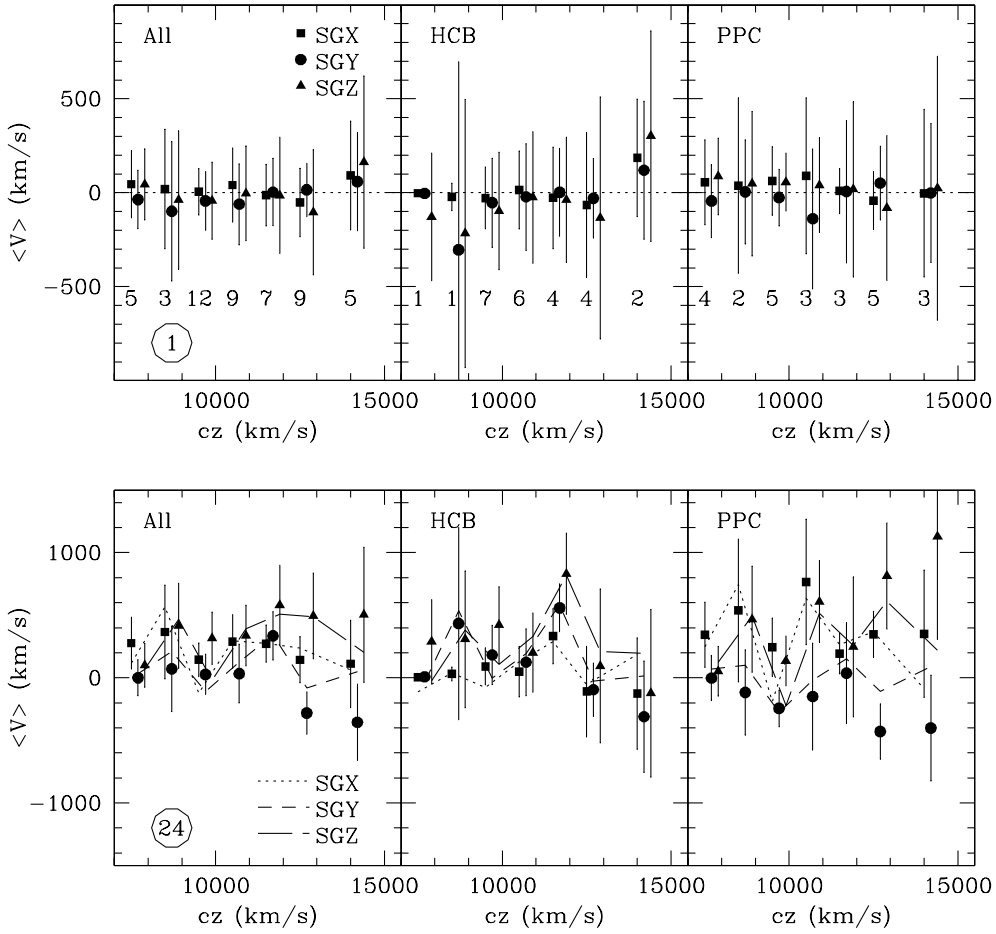

Figure 17. The simulations of the mean peculiar velocities in radial shells. The clusters are grouped in seven redshift ranges: the first is 4000–8000 km s^{-1}, the next five cover 8000 to 13 000 km s^{-1} in 1000 km s^{-1} steps, and the last is 13 000–15 000 km s^{-1}. The left-hand panels show the whole sample of 50 PV clusters, the middle panels show the HCB clusters, and the right-hand panels show the PPC clusters. The points show the mean values (over 99 simulations) of the peculiar velocities and their rms for Cases 1 (top) and 24 (bottom) of Table 1. The Supergalactic X, Y and Z components are shown as filled squares, circles and triangles respectively (with small offsets in redshift for clarity). In the bottom panels the dotted, short-dashed and long-dashed lines show the input values. The number of clusters in each redshift range is indicated at the bottom of each top panel.

As a second test, we consider the Supergalactic X, Y and Z components of the mean peculiar velocities in radial shells. Fig. 17 shows the averages of 99 simulations obtained for Cases 1 and 24 of Table 1. Again, the input values are recovered with systematic differences smaller than the statistical errors.

We determine now how well the EFAR cluster subsample can constrain the bulk flow motions determined by LP and Hudson et al. (1999). We fitted the peculiar velocities of the 50 clusters used in Paper VII with a bulk flow model $V_{\rm bulk}\cos\theta$, where θ is the angle between the dipole and cluster direction, determining $V_{\rm bulk}$ in a least-squares sense. fig. 15 of Paper VII shows these fits to the EFAR data. Fig. 18 shows that when simulations with no peculiar velocities are considered (Cases 1 and 20 to 23 of Table 1), the recovered mean $V_{\rm bulk}$ is compatible with zero, with statistical errors of about 160 km s^{-1}. Errors on the selection function parameters do not affect the result much (Cases 20 to 23), as uniform distributions of the FP parameters, of the errors, or both (Cases 45 to 47). Similarly, when the simulations with pure LP or SMAC dipole motions are considered (Cases 27 and 28 respectively), the recovered mean $V_{\rm bulk}$ is consistent with the input values within the statistical uncertainties. Fig. 16 of Paper VII shows the histograms of the recovered bulk flow amplitudes for 500 simulations. Only one out of these simulations of the LP flow, and none of SMAC, yields a $V_{\rm bulk}$ less than the value measured from the EFAR data in Paper VII. In contrast, the simulations with a random peculiar velocity component (Case 24) give mean $V_{\rm bulk}$ values similar to the observed values, both for the LP and the SMAC directions. Simulations with a random component on top of the LP and SMAC bulk flows (Cases 25 and 26) produce large mean $V_{\rm bulk}$ along the LP direction, and little net motion along the SMAC direction.

Finally, we investigate whether not only the mean motions, but also their global intrinsic fluctuations, could be determined with the EFAR cluster sample. To this purpose, we use the one-dimensional ML algorithm of Section 2.4: we consider the peculiar velocities derived for the 99 simulations of Case 24 of Table 1 and their projections along the Supergalactic X, Y and Z coordinates with their estimated errors, separately for the whole sample of PV clusters, and the northern HCB and southern PPC subsets. For each of these data sets the ML algorithm estimates the intrinsic (Gaussian) dispersion. Fig. 19 shows the results. The derived rms are systematically underestimated, by more than a factor of 2, when the input values are of the order of $\approx$600 km s^{-1}, and by $\approx$25 per cent if larger input values are considered. We

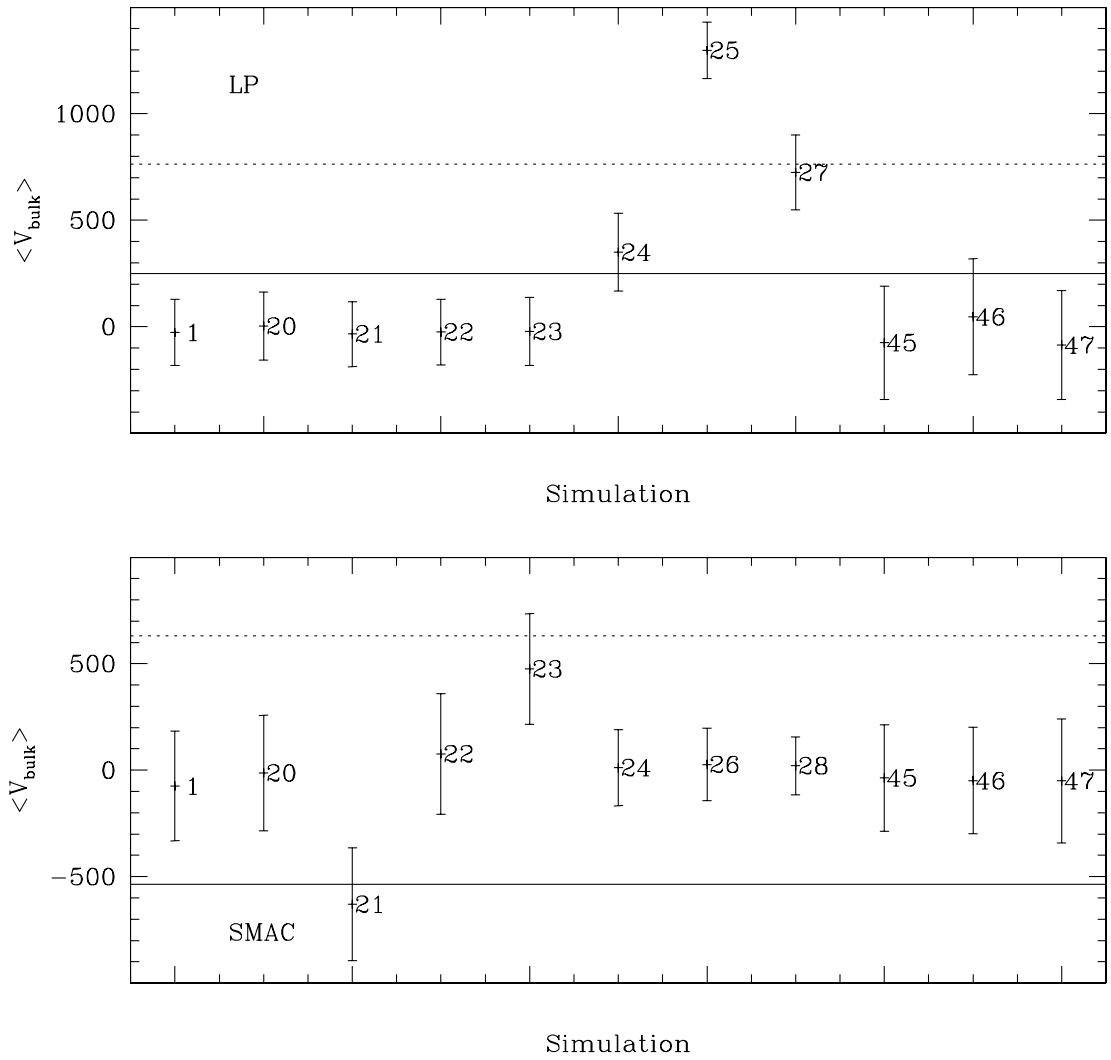

Figure 18. The simulations of the bulk flow motions of Lauer & Postman (1994, top) and Hudson et al. (1998, bottom). The points show the mean values (over 99 simulations) of $V_{\rm bulk}$ derived using the 50 clusters used in Paper VII for the determination of the EFAR mean peculiar velocities, for 11 Cases identified by the numbers in Table 1. The error bars show the rms values. The dotted lines show the values of $V_{\rm bulk}$ as derived by LP and SMAC. The full lines show the values of $V_{\rm bulk}$ as derived in Paper VII.

conclude that cluster sample is too small to allow an accurate determination of these quantities.

To summarize, the EFAR cluster sample allows us to measure the mean motions of the HCB and PPC regions with 200 km s^{-1} precision, and to constrain the bulk flow along the LP dipole direction strongly. It is less suited to constrain the SMAC result, and does not allow the accurate determination of the random peculiar motion component.

4 CONCLUSIONS

We have described the maximum-likelihood Gaussian algorithm we developed to investigate the correlations between the parameters of the EFAR data base (the Mg_2–Mgb' relation of Paper II, the Mgb'–σ and Mg_2–σ relations of Paper V, and the Fundamental Plane of Paper VII), and determine the cluster peculiar velocities of Paper VII.

We performed extensive testing based on mock catalogues of the EFAR sample. We find that 'canonical' methods based on a least-squares approach cannot cope with the challenge of a sample with a spread of a factor of 2 in redshift, with sizable selection effects, non-negligible and non-uniform errors, and explicit cuts. We quantify the size of the systematic biases these methods introduce. In contrast, the maximum-likelihood Gaussian algorithm takes into account errors, selection effects and the presence of explicit cuts, determining nearly unbiased estimates of the slopes of the correlations and their intrinsic and parallel spread. 10–30 per cent of the analysed simulations have mean likelihoods larger than that of the EFAR sample, justifying the use of Gaussian modelling. We derive the analytical solution of the maximum-likelihood Gaussian problem in N dimensions in the presence of small errors. We show that the residual systematic biases are always smaller than the statistical errors. We investigate in detail the effects of cluster sample selection, errors in the selection function parameters, and selection cuts. We explore the cases of uniform distributions of parameters and errors. We conclude that the mean peculiar motions of the EFAR clusters can be determined reliably. In particular, the large amplitude of the dipole motion measured by Lauer & Postman (1994) can be strongly constrained.

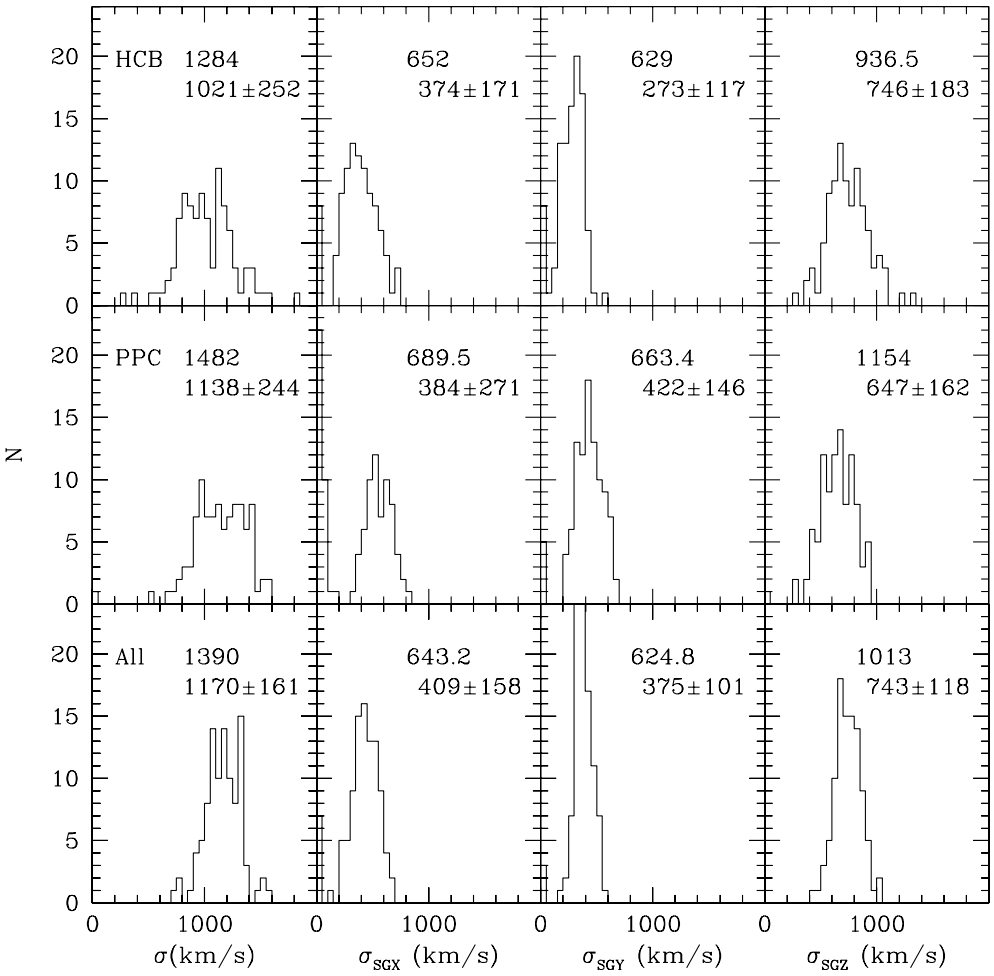

Figure 19. The histograms of the peculiar velocity dispersions derived from the one-dimensional ML analysis of the 99 simulations of Case 24 of Table 1. The dispersions are shown separately for the HCB, PPC and PV cluster samples, for the radial peculiar velocities and their projections along the Supergalactic *X*, *Y* and *Z* projections. The labels give the input dispersions, the results averaged over the 99 simulations and their rms.

ACKNOWLEDGMENTS

RPS acknowledges the support by DFG grant SFB 375. GW is grateful to the SERC and Wadham College for a year's stay in Oxford, and to the Alexander von Humboldt-Stiftung for making possible a visit to the Ruhr-Universität in Bochum. MC acknowledges the support of a Lindemann Fellowship, a DIST Collaborative Research Grant and an Australian Academy of Science/Royal Society Exchange Program Fellowship. This work was partially supported by NSF Grant AST90-16930 to DB, AST90-17048 and AST93-47714 to GW, AST90-20864 to RKM. The entire collaboration benefitted from NATO Collaborative Research Grant 900159 and from the hospitality and monetary support of Dartmouth College, Oxford University, the University of Durham and Arizona State University. Support was also received from PPARC visitors grants to Oxford and Durham Universities, and a PPARC rolling grant: 'Extragalactic Astronomy and Cosmology in Durham 1994–98'.

REFERENCES

Abramowitz M., Stegun A., 1971, Handbook of Mathematical Functions. Dover, New York

Akritas M. G., Bershady M. A., 1996, ApJ, 470, 706

Carvalho R. R., Djorgovski S., 1992, ApJ, 389, L49

Colless M. M., 1995, AJ, 109, 1937

Colless M., Burstein D., Davies R. L., McMahan R., Saglia R. P., Wegner G., 1999, MNRAS, 303, 813 (Paper V)

Colless M., Saglia R. P., Burstein D., Davies R. L., McMahan R., Wegner G., 2001, MNRAS, 321, 277 (Paper VII)

Djorgovski S., Davis M., 1987, ApJ, 313, 59

Dressler A., Lynden-Bell D., Burstein D., Davies R. L., Faber S. M., Terlevich R. J., Wegner G., 1987, ApJ, 313, 42

Eadie W. T., Dryard D., James F. E., Roos M., Sadoulet B., 1971, Statistical Methods in Experimental Physics. North-Holland Publishing Company, Amsterdam

Feigelson E. D., Babu G. J., 1992, ApJ, 397, 55

Hudson M. J., Lucey J. R., Smith R. J., Steel J., 1997, MNRAS, 291, 461

Hudson M. J., Smith R. J., Lucey J. R., Schlegel D. J., Davies R. L., 1999, ApJ, 512, L79 (SMAC)

Isobe T., Feigelson E. D., Akritas M. G., Babu G. J., 1990, ApJ, 364, 104

Jørgensen I., 1997, MNRAS, 288, 161

Jørgensen I., Franx M., Kjærgaard P., 1996, MNRAS, 280, 167

La Barbera F., Busarello G., Capaccioli M., 2000, A&A, 362, 851

Lauer T. R., Postman M., 1994, ApJ, 425, 418 (LP)

Pahre M. A., Djorgovski S. G., De Carvalho R. R., 1997, in Da Costa L. N., Renzini A., eds, Proc. of the ESO Workshop on Galaxy Scaling Relations: Origins, Evolution and Applications. Springer-Verlag, Berlin

Press W. H., Flannery B. P., Teukolsky S. A., Vetterling W. T., 1986, Numerical Recipes. Cambridge Univ. Press, Cambridge
Saglia R. P., Burstein D., Baggley G., Bertschinger E., Colless M. M., Davies R. L., McMahan R., Wegner G., 1997a, MNRAS, 292, 499(Paper III)
Saglia R. P., Bertschinger E., Baggley G., Burstein D., Colless M. M., Davies R. L., McMahan R., Wegner G., 1997b, ApJS, 109, 79(Paper IV)
Scodeggio M., Giovanelli R., Haynes M. P., 1997, AJ, 113, 101
Teerikorpi P., 1997, ARA&A, 35, 101
van Albada T. S., Bertin G., Stiavelli M., 1993, MNRAS, 265, 627
Wegner G., Colless M., Baggley G., Davies R. L., Bertschinger E., Burstein D., McMahan R., Saglia R. P., 1996, ApJS, 106, 1 (Paper I)
Wegner G., Colless M., Burstein D., Saglia R. P., McMahan R., Davies R. L., Baggley G., 1999, MNRAS, 305, 259 (Paper II)
Weinberg S., 1972, Gravitation and Cosmology. Wiley, New York
Willick J. A., 1994, ApJS, 92, 1

APPENDIX A: ONE-DIMENSIONAL MODEL, LIMITING CASE

Neglecting the presence of cuts, the maximization of equation (17) leads to

$$\mu = \frac{\sum_i \dfrac{x_i}{S_i(\sigma_i^2+\sigma^2)}}{\sum_i \dfrac{1}{S_i(\sigma_i^2+\sigma^2)}}, \tag{A1}$$

$$\sum_i \frac{\sigma_i^2+\sigma^2-(x_i-\mu)^2}{S_i(\sigma_i^2+\sigma^2)^2} = 0. \tag{A2}$$

Here we solve equations (A1) and (A2) in the limiting case of small measurement errors ($\sigma_i \sigma$). We get

$$\mu = \bar{x} + (\bar{x} - \bar{x}_{\rm err})\frac{\sigma_{\rm err}^2}{s^2}, \tag{A3}$$

$$\sigma^2 = s^2 - \sigma_{\rm err}^2 + 2\sigma_{\rm err}^2\left(1 - \frac{s_{\rm err}^2}{s^2}\right), \tag{A4}$$

where $\bar{x} = (\Sigma_i x_i/S_i)/(\Sigma 1/S_i)$ is the selection-weighted mean, $\bar{x}_{\rm err} = (\Sigma_i x_i\sigma_i^2/S_i)/(\Sigma_i\sigma_i^2/S_i)$ is the error and selection-weighted mean, $\sigma_{\rm err}^2 = (\Sigma\sigma_i^2/S_i)/(\Sigma 1/S_i)$ is the selection-weighted mean square error, $s^2 = (\Sigma(x-\bar{x})^2/S_i)/(\Sigma_i 1/S_i)$ is the selection-weighted rms, and $s_{\rm err}^2 = (\Sigma\sigma_i^2(x-\bar{x})^2/S_i)/(\Sigma_i\sigma_i^2/S_i)$ is the selection- and error-weighted rms. Therefore the mean and rms are obtained by correcting the usual formulae with a term taking into account the spread in errors.

APPENDIX B: THE TWO-DIMENSIONAL MODEL, LIMITING CASE

Here we present the solution which minimizes equation (16) in the limiting case of small errors (with a diagonal error matrix), no peculiar velocities and no cuts, considering expansions to first order in the errors, for the two-dimensional case. In Appendix C we derive the general result in the N-dimensional case. To simplify the notation in the following, we call the components (x_1, x_2) as (x, y). For the mean values we find:

$$\bar{x} = x^{(0)} + \sigma_{ex}^2[V_{22}^{(0)}(x^{(0)} - x_x^{(1)}) - V_{12}^{(0)}(y^{(0)} - y_x^{(1)})]/\Delta^{(0)}, \tag{B1}$$

$$\bar{y} = y^{(0)} + \sigma_{ey}^2[-V_{12}^{(0)}(x^{(0)} - x_y^{(1)}) + V_{11}^{(0)}(y^{(0)} - y_y^{(1)})]/\Delta^{(0)}, \tag{B2}$$

where $x^{(0)} = (\Sigma_i x_i/S_i)/S$, $y^{(0)} = (\Sigma_i y_i/S_i)/S$, $S = \Sigma_i 1/S_i$, $x_x^{(1)} = (\Sigma_i x_i\sigma_{xi}^2/S_i)/(S\sigma_{ex}^2)$, $x_y^{(1)} = (\Sigma_i x_i\sigma_{yi}^2/S_i)/(S\sigma_{ey}^2)$, $\sigma_{ex}^2 = (\Sigma_i\sigma_{xi}^2/S_i)/S$, $\sigma_{ey}^2 = (\Sigma_i\sigma_{yi}^2/S_i)/S$, $y_x^{(1)} = (\sum_i y_i\sigma_{xi}^2/S_i)/(S\sigma_{ex}^2)$, $y_y^{(1)} = (\Sigma_i y_i\sigma_{yi}^2/S_i)/(S\sigma_{ey}^2)$, $V_{11}^{(0)} = (\Sigma_i(x_i - x^{(0)})^2/S_i)/S$, $V_{22}^{(0)} = (\Sigma_i(y_i - y^{(0)})^2/S_i)/S$, $V_{12}^{(0)} = (\Sigma_i(x_i - x^{(0)})(y_i - y^{(0)})/S_i)/S$, and $\Delta^{(0)} = V_{11}^{(0)}V_{22}^{(0)} - V_{12}^{(0)2}$. The covariance matrix $\boldsymbol{V}$ is:

$$\begin{aligned} V_{11} &= V_{11}^{(0)} + V_{11}^{(1)} \\ &= V_{11}^{(0)} - \sigma_{ex}^2 \\ &\quad + 2\sigma_{ex}^2[1 - (V_{22}^{(0)}\sigma_{xx,ex}^2 - V_{12}^{(0)}\sigma_{xy,ex})/\Delta^{(0)}], \end{aligned} \tag{B3}$$

$$\begin{aligned} V_{22} &= V_{22}^{(0)} + V_{22}^{(1)} \\ &= V_{22}^{(0)} - \sigma_{ey}^2 \\ &\quad + 2\sigma_{ey}^2[1 - (V_{11}^{(0)}\sigma_{yy,ey}^2 - V_{12}^{(0)}\sigma_{xy,ey})/\Delta^{(0)}], \end{aligned} \tag{B4}$$

$$\begin{aligned} V_{12} &= V_{12}^{(0)} + V_{12}^{(1)} \\ &= V_{12}^{(0)} - \sigma_{ex}^2(V_{22}^{(0)}\sigma_{xy,ex} - V_{12}^{(0)}\sigma_{yy,ex}^2)/\Delta^{(0)} \\ &\quad - \sigma_{ey}^2(V_{11}^{(0)}\sigma_{xy,ey} - V_{12}^{(0)}\sigma_{xx,ey}^2)/\Delta^{(0)}, \end{aligned} \tag{B5}$$

where $\sigma_{xx,ex}^2 = [\Sigma_i(x^i - x^{(0)})^2\sigma_{xi}^2/S_i]/(S\sigma_{ex}^2)$, $\sigma_{yy,ey}^2 = [\Sigma_i(y_i - y^{(0)})^2\sigma_{yi}^2/S_i]/(S\sigma_{ey}^2)$, $\sigma_{xy,ex}^2 = [\Sigma_i(x_i - x^{(0)})(y_i - y^{(0)})\sigma_{xi}^2/S_i]/(S\sigma_{ex}^2)$, $\sigma_{xy,ey}^2 = [\Sigma_i(x_i - x^{(0)})(y_i - y^{(0)})\sigma_{yi}^2/S_i]/(S\sigma_{ey}^2)$. As in the one-dimensional case, we recognize the usual (error-corrected) zeroth-order term, plus a term taking into account the spread in the errors. With no spread in the errors we have $V_{12}^{(1)} = 0$, and we recover the Ansatz of Akritas & Bershady (1996). To first order, equation (9) then reads

$$\begin{aligned} a_o \approx a_o^{(0)} + a_o^{(1)} = a_o^{(0)}\Bigg[1 &+ \frac{V_{22}^{(1)} - V_{11}^{(1)}}{\sqrt{(V_{22}^{(0)} - V_{11}^{(0)})^2 + 4V_{12}^{(0)2}}} \\ &- \frac{V_{12}^{(1)}}{V_{12}^{(0)}}\frac{V_{22}^{(0)} - V_{11}^{(0)}}{\sqrt{(V_{22}^{(0)} - V_{11}^{(0)})^2 + 4V_{12}^{(0)2}}}\Bigg], \end{aligned} \tag{B6}$$

where $a_o^{(0)}$ is equation (9) evaluated using $V^{(0)}$. With no spread in the errors,

$$a_+ = a_o^{(0)}\left[1 + (\sigma_{ex}^2 - \sigma_{ey}^2)/\sqrt{(V_{22}^{(0)} - V_{11}^{(0)})^2 + 4V_{12}^{(0)2}}\right]. \tag{B7}$$

Therefore $a_o^{(0)}$ *underestimates* the true slope if the error in the x direction is larger than that in y.

APPENDIX C: DERIVATION OF THE N-DIMENSIONAL CASE

Let $\boldsymbol{V}$ be the intrinsic covariance matrix and $\boldsymbol{\Lambda}$ its inverse, $\boldsymbol{E}_i$ the error matrix of each point, $\boldsymbol{V}_i = \boldsymbol{V} + \boldsymbol{E}_i$ the observed covariance matrix of each point, with $\boldsymbol{E}_i \ll \boldsymbol{V}$. Then we have

$$\begin{aligned} \boldsymbol{\Lambda}_i = (\boldsymbol{V} + \boldsymbol{E}_i)^{-1} &= [\boldsymbol{V}(\boldsymbol{I} + \boldsymbol{V}^{-1}\boldsymbol{E}_i)]^{-1} = (\boldsymbol{I} + \boldsymbol{\Lambda}\boldsymbol{E}_i)^{-1}\boldsymbol{\Lambda} \\ &\sim (\boldsymbol{I} - \boldsymbol{\Lambda}\boldsymbol{E}_i)\boldsymbol{\Lambda} = \boldsymbol{\Lambda} - \boldsymbol{\Lambda}\boldsymbol{E}_i\boldsymbol{\Lambda}, \end{aligned} \tag{C1}$$

where the first-order approximation $(\boldsymbol{I} + \boldsymbol{\epsilon})^{-1} \sim \boldsymbol{I} - \boldsymbol{\epsilon}$ was used.

We get

$$\det \boldsymbol{V}_i = \det \boldsymbol{V} \det(1 + \boldsymbol{\Lambda E}_i) = \det \boldsymbol{V}[1 + \mathrm{tr}(\boldsymbol{\Lambda E}_i)]$$
$$= \det \boldsymbol{V}(1 + \Sigma_{jk} \Lambda_{jk} E_{i,jk}), \tag{C2}$$

where the first-order approximation $\det(\boldsymbol{I} + \boldsymbol{\epsilon}) \sim 1 + \mathrm{tr}(\boldsymbol{\epsilon})$ was used. Therefore to first order we get

$$\det \boldsymbol{\Lambda}_i = \det \boldsymbol{\Lambda}(1 - \Sigma_{jk} \Lambda_{jk} E_{i,jk}). \tag{C3}$$

The equation for the likelihood reads

$$\mathcal{L} = \prod_{i=1}^{m}$$
$$\times \left\{ \frac{\sqrt{\det \boldsymbol{\Lambda}}}{(2\pi)^{n/2}} (1 - 0.5 \Sigma_{jk} \Lambda_{jk} E_{i,jk}) \exp[-\hat{\boldsymbol{x}}_i^T (\boldsymbol{\Lambda} - \boldsymbol{\Lambda E}_i \boldsymbol{\Lambda}) \hat{\boldsymbol{x}}_i / 2] \right\}^{1/S_i}, \tag{C4}$$

where $\hat{\boldsymbol{x}}_i = \boldsymbol{x}_i - \bar{\boldsymbol{x}}$, $\boldsymbol{x}_i$ are the n-dimensional m vectors of data points, and $\bar{\boldsymbol{x}}$ is the vector of the mean values. Taking the logarithm, we get

$$\ln \mathcal{L} = \Sigma_{i=1}^{m} \frac{1}{S_i}$$
$$\times \left[-\frac{n}{2} \ln(2\pi) + \frac{1}{2} \ln \det \boldsymbol{\Lambda} - \frac{1}{2} \Sigma_{jk} \Lambda_{jk} E_{i,jk} - \frac{1}{2} \hat{\boldsymbol{x}}_i^T (\boldsymbol{\Lambda} - \boldsymbol{\Lambda E}_i \boldsymbol{\Lambda}) \hat{\boldsymbol{x}}_i \right]. \tag{C5}$$

The equation for the vector of the mean values reads

$$\frac{\partial \ln \mathcal{L}}{\partial \bar{\boldsymbol{x}}_k} = \Sigma_i (\boldsymbol{\Lambda} - \boldsymbol{\Lambda E}_i \boldsymbol{\Lambda})(\boldsymbol{x}_i - \bar{\boldsymbol{x}})_k / S_i = 0. \tag{C6}$$

Setting $\bar{\boldsymbol{x}} = \boldsymbol{x}^{(0)} + \boldsymbol{x}^{(1)}$, the zeroth-order term is

$$\boldsymbol{x}^{(0)} = (\Sigma_i \boldsymbol{x}_i / S_i) / (\Sigma_i 1 / S_i). \tag{C7}$$

The first-order term is then

$$-\Sigma_i \boldsymbol{\Lambda} \boldsymbol{x}^{(1)} / S_i = \Sigma_i \boldsymbol{\Lambda E}_i \boldsymbol{\Lambda} (\boldsymbol{x}_i - \boldsymbol{x}^{(0)}) / S_i, \tag{C8}$$

and therefore

$$\boldsymbol{x}^{(1)} = (\Sigma_i \boldsymbol{E}_i \boldsymbol{\Lambda} (\boldsymbol{x}^{(0)} - \boldsymbol{x}_i) / S_i) / (\Sigma_i 1 / S_i), \tag{C9}$$

which is equivalent to equations (B1) and (B2) for E_i diagonal and taking the zeroth order for $\boldsymbol{\Lambda}$ (see below).

Let now consider the derivatives with respect to the $\boldsymbol{\Lambda}$ components:

$$\frac{\partial \ln \mathcal{L}}{\partial \Lambda_{lm}} = \Sigma_i \frac{1}{S_i} \left[\frac{1}{2 \det \boldsymbol{\Lambda}} \frac{\partial \det \boldsymbol{\Lambda}}{\partial \Lambda_{lm}} - \frac{1}{2} \Sigma_{jk} E_{i,jk} \frac{\partial \Lambda_{jk}}{\partial \Lambda_{lm}} \right.$$
$$\left. - \frac{1}{2} \hat{\boldsymbol{x}}_i^T \left(\frac{\partial \boldsymbol{\Lambda}}{\partial \Lambda_{lm}} \right) \hat{\boldsymbol{x}}_i + \frac{1}{2} \hat{\boldsymbol{x}}_i^T \left(\frac{\partial \boldsymbol{\Lambda E}_i \boldsymbol{\Lambda}}{\partial \Lambda_{lm}} \right) \hat{\boldsymbol{x}}_i \right] = 0. \tag{C10}$$

Let first note that

$$\frac{1}{\det \boldsymbol{A}} \frac{\partial \det \boldsymbol{A}}{\partial A_{lm}} = \frac{(-1)^{l+m} \det \boldsymbol{A}_{(l,m)}}{\det \boldsymbol{A}} = A_{lm}^{-1}, \tag{C11}$$

where $\boldsymbol{A}_{(l,m)}$ is the matrix obtained by eliminating the row l and the column m. Since $\boldsymbol{\Lambda}$ is symmetric, we get

$$\frac{1}{\det \boldsymbol{\Lambda}} \frac{\partial \det \boldsymbol{\Lambda}}{\partial \Lambda_{lm}} = 2 V_{lm} \tag{C12}$$

if $l \neq m$, and

$$\frac{1}{\det \boldsymbol{\Lambda}} \frac{\partial \det \boldsymbol{\Lambda}}{\partial \Lambda_{ll}} = V_{ll} \tag{C13}$$

otherwise. Similarly, we get $\partial \Lambda_{jk} / \partial \Lambda_{lm} = \delta_{jl} \delta_{km} + \delta_{jm} \delta_{kl}$ if $l \neq m$ and $\partial \Lambda_{jk} / \partial \Lambda_{ll} = \delta_{jl} \delta_{kl}$. Finally, we derive

$$\left(\frac{\partial \boldsymbol{\Lambda E}_i \boldsymbol{\Lambda}}{\partial \Lambda_{lm}} \right)_{jk} = \Sigma_\mu E_{i,l\mu} (\Lambda_{\mu k} \delta_{jm} + \Lambda_{\mu j} \delta_{km})$$
$$+ \Sigma_\nu E_{i,m\nu} (\Lambda_{\nu k} \delta_{jl} + \Lambda_{\nu j} \delta_{kl}) \tag{C14}$$

if $l \neq m$, and

$$\left(\frac{\partial \boldsymbol{\Lambda E}_i \boldsymbol{\Lambda}}{\partial \Lambda_{ll}} \right)_{jk} = \Sigma_\mu \delta_{kl} \Lambda_{j\mu} E_{i,\mu l} + \Sigma_\nu \delta_{jl} E_{i,l\nu} \Lambda_{\nu k} \tag{C15}$$

otherwise. Writing the covariance matrix as $\boldsymbol{V} = \boldsymbol{V}^{(0)} + \boldsymbol{V}^{(1)}$, the zeroth order reads $V_{jk}^{(0)} = [\Sigma_i (\boldsymbol{x}_i - \boldsymbol{x}^{(0)})_j (\boldsymbol{x}_i - \boldsymbol{x}^{(0)})_k / S_i] / (\Sigma_i 1 / S_i)$. The first order comes from the terms of equation (C10) linear in $\boldsymbol{E}_i$:

$$V_{ll}^{(1)} = E_{ll} - 2 \Sigma_{j\mu} \sigma_{jl,\mu l} \Lambda_{j\mu}^{(0)} E_{\mu l}, \tag{C16}$$

$$V_{lm}^{(1)} = E_{lm} - \Sigma_{k\mu} \sigma_{mk,l\mu} \Lambda_{\mu k}^{(0)} E_{\mu l} - \Sigma_{k\nu} \sigma_{lk,m\nu} \Lambda_{\nu k}^{(0)} E_{\nu m}, \tag{C17}$$

where $\boldsymbol{E} = (\Sigma_i \boldsymbol{E}_i / S_i) / (\Sigma_i 1 / S_i)$ and $\sigma_{jl,\mu\nu} = [\Sigma_i (\boldsymbol{x}_i - \boldsymbol{x}^{(0)})_j \times (\boldsymbol{x}_i - \boldsymbol{x}^{(0)})_l E_{i,\mu\nu} / S_i] / (\Sigma_i E_{i,\mu\nu} / S_i)$. Note that $\boldsymbol{V}^{(1)} = -\boldsymbol{E}$ if there is no spread in the errors (i.e., $\boldsymbol{E}_i = \text{constant}$).

APPENDIX D: THE PHOTOMETRIC ERROR MATRIX

The photometric part of the error matrix $\boldsymbol{E}_i$ of equation (26) can be derived as follows. Paper IV shows that the errors in the half-luminosity radii δr_i and average surface brightness δu_i derived from the fits to the photometric profiles are correlated, with $\delta FP_i = \delta r_i - \alpha \delta u_i$ and $\alpha \approx 0.3$, and calibrates the values of δr_i and δFP_i in terms of the quality parameter Q. Therefore we consider the rotated coordinates $(y, z) = \boldsymbol{T}(\log R_{e,i}, \langle SB_{e,i} \rangle)$, where $y = (\log R_{e,i} - \alpha \langle SB_{e,i} \rangle) / \sqrt{1 + \alpha^2}$ and $z = (\alpha \log R_{e,i} + \langle SB_{e,i} \rangle) / \sqrt{1 + \alpha^2}$, and $\boldsymbol{T}$ the corresponding rotation matrix. In these coordinates the error matrix $\boldsymbol{E}_{yz}$ is diagonal, with $E_{yz,11} = \sigma_y^2$ and $E_{yz,22} = \sigma_z^2$. From the definition of y it follows $\sigma_y^2 = \delta FP_i^2 / (1 + \alpha^2)$. From $\log R_{e,i} = (y + \alpha z) / \sqrt{1 + \alpha^2}$ and the fact that the errors on y and z are uncorrelated, we get $\delta r_i^2 = (\sigma_y^2 + \alpha^2 \sigma_z^2) / (1 + \alpha^2)$ and finally $\sigma_z^2 = [(1 + \alpha^2) \delta r_i^2 - \delta FP_i^2 / (1 + \alpha^2)] / \alpha^2$. The matrix $\boldsymbol{T}^T \boldsymbol{E}_{yz} \boldsymbol{T}$ then gives

$$E_{i,11} = \frac{\sigma_y^2 + \alpha^2 \sigma_z^2}{1 + \alpha^2} = \delta r_i^2, \tag{D1}$$

$$E_{i,13} = E_{i,31} = \frac{\alpha}{1 + \alpha^2} (\sigma_z^2 - \sigma_y^2) = \frac{(1 + \alpha^2) \delta r_i^2 - \delta FP_i^2}{\alpha (1 + \alpha^2)}, \tag{D2}$$

$$E_{i,33} = \frac{\alpha^2 \sigma_y^2 + \sigma_z^2}{1 + \alpha^2} = \frac{(\alpha^2 - 1) \delta FP_i^2 + (1 + \alpha^2) \delta r^2}{\alpha^2 (1 + \alpha^2)}. \tag{D3}$$

APPENDIX E: THE NORMALIZATION OF THE 3-DIM DISTRIBUTION FUNCTION

The integral of equation (22) can be performed by defining the set

of rotated coordinates $(w_1, w_2, w_3) = Q(\hat{\boldsymbol{x}})$:

$$w_1 = \frac{\hat{x}_1 - b\hat{x}_3}{\sqrt{1+b^2}},$$

$$w_2 = \hat{x}_2, \tag{E1}$$

$$w_3 = \frac{b\hat{x}_1 + \hat{x}_3}{\sqrt{1+b^2}}. \tag{E2}$$

Writing $\boldsymbol{M} = \boldsymbol{Q}^T \boldsymbol{\Lambda}_i \boldsymbol{Q}$, integration over w_3 leads to the following integral:

$$f_{3i} = \frac{|\boldsymbol{W}|}{2\pi} \int_{w_{1c}}^{\infty} \int_{w_{2c}}^{\infty} \exp(-\boldsymbol{w}^T W \boldsymbol{w}/2)\, \mathrm{d}w_1\, \mathrm{d}w_2, \tag{E3}$$

where the 2×2 matrix $\boldsymbol{W}$ is

$$W_{i,j} = M_{i,j} - \frac{M_{i,3} M_{j,3}}{M_{3,3}}, \tag{E4}$$

and $w_{1c} = (FP_{\rm cut} - \overline{FP})/\sqrt{1+\alpha^2}$, where $FP_{\rm cut} = 0.78 \log D_{Wcut} - 0.61$ (Paper III, $\alpha = 0.3 \approx b$), $\overline{FP} = \overline{\log R_{\rm e}} - \delta_j - \alpha\overline{\langle SB_{\rm e}\rangle}$) and $w_{2c} = \log \sigma_{\rm cut} - \overline{\log \sigma}$. Finally, one gets

$$f_{3i} = L(h, k, \rho), \tag{E5}$$

where $L(h,k,\rho)$ is the bivariate probability integral (Abramovitz & Stegun 1971), $h = w_{1c}\sqrt{W_{2,2}(1-\rho^2)}$, $k = w_{2c}\sqrt{W_{1,1}(1-\rho^2)}$ and $\rho = -W_{1,2}/\sqrt{W_{1,1}W_{2,2}}$.

This paper has been typeset from a TEX/LATEX file prepared by the author.